The Vertex Effect in Polycrystalline Materials

Simulation, a Macroscopic Model, and Structural Application

Dissertation
zur Erlangung des akademischen Grades
Doktoringenieur
(Dr.-Ing.)

von Dipl.-Ing. Michael Schurig
geb. am 16.01.1973 in Berlin
genehmigt durch die Fakultät für Maschinenbau
der Otto-von-Guericke-Universität Magdeburg

Gutachter:
Prof. Albrecht Bertram
Prof. Henryk Petryk
Promotionskolloquium am 17.07.2006

The Vertex Effect in Polycrystalline Materials

Simulation, a Macroscopic Model, and Structural Application

The Vertex Effect in Polycrystalline Materials

Simulation, a Macroscopic Model, and Structural Application

Dissertation
zur Erlangung des akademischen Grades
Doktoringenieur
(Dr.-Ing.)

von Dipl.-Ing. Michael Schurig
geb. am 16.01.1973 in Berlin
genehmigt durch die Fakultät für Maschinenbau
der Otto-von-Guericke-Universität Magdeburg

Gutachter:
Prof. Albrecht Bertram
Prof. Henryk Petryk
Promotionskolloquium am 17.07.2006

September 5, 2006

Acknowledgements

Soli Deo Gloria.

The work presented in this thesis has been done during my time as a research staff member at the Otto-von-Guericke-Universität Magdeburg.

I am indebted to Prof. Albrecht Bertram, who was the advisor and the first referee of this thesis. He was a guide in finding the topic of the work and finally finishing it. His mentorship by teaching the theoretical foundations of continuum mechanics and widening the view by stimulating a variety of contacts was a great experience.

I also wish to thank Prof. Henryk Petryk, Polish Academy of Science, for the supportive discussions on the general topic and several aspects of the work, and for being the second referee.

I enjoyed being a member of a team of great colleagues. In particular, I wish to thank Enrico Brosche for his help with numerical integration.

I would like to mention the support and the interdisciplinary discussions as an associated member in the Graduate School "Micro-Macro-Interactions in Structured Media and Particle Systems", supported by DFG.

Last but not least I wish to express my deepest gratitude to my beloved wife Doris, who cared for our children Lisa and Julius and by this gave me the opportunity to work on this thesis.

CONTENTS

1. ZUSAMMENFASSUNG

Der *Vertex-Effekt* beschreibt den Einfluss mehrerer koexistenter plastischer Fließmechanismen in ihrer Interaktion. Sie bewirken, dass am Schnittpunkt der Fließflächen im Spannungsraum eine Ecke (*Corner*, *Vertex*) im zusammengesetzten Fließort entsteht, was zur Namensgebung geführt hat.

Wenn sehr viele Mechanismen existieren, wie in Polykristallen, ist von größerer Bedeutung der Einfluss auf die sich ergebende Fließregel. Ein Vergleich der Mehrflächenplastizität (Abschnitt 4.3) mit regularisierten Versionen (Abschnitt 4.4) zeigt in Abschnitt 4.5, dass dieses einerseits auf den Rang des inkrementellen linearen Operators und andererseits auf den nichtlinearen Einfluss der Belastungsbedingung für die Gleitsysteme zurückzuführen ist. Berücksichtigt man die stückweise Definition des aktiven Set der Gleitsysteme, so kann dieser Einfluss durch ein einzelnes, aber stückweise definiertes plastisches Potential beschrieben werden.

Dieser Weg wird in Kapitel 6 beschritten. Das vorgeschlagene plastische Potential erweitert die assoziierte Fließregel nach von Mises um Terme, die eine Fließflächenparallele Komponente des plastischen Fließens in Abhängigkeit von der Abweichung vom proportionalen Belastungspfad gestattet. Dieser Einfluss wird durch einen einzelnen skalaren Parameter α beschrieben, der den Richtungskosinus der Rate des elastischen Mandel-Spannungstensors bei eingefrorenen plastischen Variablen im Verhältnis zur proportionalen Prozessrichtung wiedergibt. Diese Wahl wurde getroffen, weil dieser Parameter für die Belastungsbedingung der Mehrflächenplastizität maßgeblich ist.

Es zeigt sich, dass die Null-Fläche des gewählten Potentials mit der der Fließfläche übereinstimmt, da die Normale der von-Mises-Fließfläche mit der radialen Richtung eines proportionalen Prüfprozesses übereinstimmt.

Die zusätzlichen Materialfunktionen werden mit Hilfe einer Simulation mit dem Taylor-Modell, das als numerisches Laboratorium dient, bestimmt. In einem einzelnen Zeitschritt ergibt sich eine deutliche Verbesserung der Fließrichtung und der dissipierten Leistung im Gegensatz zur J_2-Theorie.

Weitere Untersuchungen mit Hilfe des Taylor-Modelles zeigen in Kapitel 5 die Entwicklung einer Ecke in der Polykristallfließfläche, die nach dem Dissipationskriterium bestimmt wurde. Diese Ecke wandert auf proportionalen und nichtproportionalen Pfaden mit dem Spannungspunkt und entsteht durch das intergranulare Eigenspannungsfeld schon nach kleiner Vorverformung.

Die vorgeschlagene Theorie wird in Abschnitt 6.5 durch einen Vergleich mit experimentellen Befunden eines mehrachsigen Zug-Torsions-Versuches (Lensky, 1960) verifiziert. Auch auf einem komplexen Prozesspfad zeigt sich die Verbes-

serung gegenüber der J_2-Theorie.

Als letztes Anwendungsbeispiel wird das Drillknicken einer kreuzförmigen Säule untersucht. Dieses Beispiel sorgte in den 1940er und 1950er Jahren für erhebliche Zweifel an der Richtigkeit der J_2-Fließtheorie, da die entsprechende Deformationstheorie weitaus bessere Ergebnisse für die kritische Knicklast lieferte. Später wurde dies mit der zu großen tangentialen Steifigkeit bei nichtproportionalen Prozessen erklärt, die aus dem fehlenden Vertex-Effekt herrührt. Im Gegensatz dazu ist der Modul der Deformationstheorie völlig pfadunabhängig. Dieser Fehler zeigt sich bei diesem speziellen Problem als günstig.

Mit dem vorgeschlagenen Vertex-Modell lässt sich auf analytischem Weg zeigen, dass die richtige Steifigkeit aus der geeigneten Mittelung der Steifigkeiten über die Plattendicke resultiert. Die experimentell ermittelten Knicklasten lassen sich korrekt wiedergeben, im Gegensatz zur J_2-Theorie, die infolge der postulierten Entlastung ein Verfestigungsunabhängiges Ergebnis liefert.

2. INTRODUCTION

2.1 The Vertex Effect

The term *vertex effect* means the experimentally and theoretically well founded fact that plastic materials in a stress state where the yield surfaces of several distinct plastic glide mechanisms intersect in a vertex in the stress space, behave differently from materials with a smooth yield surface.

At first, the normality rule is not directly applicable, because a well defined normal is lacking.

Secondly, the interaction of different mechanisms allows for a more complicated constitutive behaviour in the flow rule. In particular, a nonlinear dependence of the direction of plastic flow on the loading direction can be stated.

As a third topic, the shape of the yield surface is not smooth, indicating the presence of strong distortional hardening dependent on the loading history.

The vertex effect is important as it explains a couple of problems encountered in application of smooth plasticity (as the contrasting theory without a vertex effect). In particular, such material models behave excessively stiff upon strain path changes as can be seen in nonproportional experiments, like e.g. multiaxial strain or torsional buckling.

2.2 Literature review

2.2.1 Isotropic criteria

Non-smooth yield surfaces are not a modern invention. As early as in the work of (Tresca, 1864), corners in the yield surface were assumed. The criterion

$$\max \tau_{ij} - k = 0 \tag{2.1}$$

leads to a number of three distinct criteria. At some points the according hyperplanes in stress space intersect, leading to a non-smooth boundary of the elastic domain. As the material described by the Tresca criterion is isotropic, the nonsmoothness was taken as a disadvantage. In contrast, the smooth Huber-v.Mises-criterion has been widely accepted.

2.2.2 Early models of polycrystal plasticity

With the investigation of crystals, the research interest focussed on the existence of several physically distinct mechanisms. The early work of Taylor (1938) and

Sachs (1928) were not embedded in a continuum theory of plasticity. Hence, a gap opened between the smooth isotropic continuum theory of plasticity and the non-smooth anisotropic discrete crystal plasticity.

In the second half of the twentieth century, this gap was filled. For the first time, Batdorf and Budiansky (1949) decomposed the plastic strain into contributions of infinitely many slip systems. Heuristic hardening laws for each mechanism were fitted to experiments.

Koiter (1953) introduced multiple yield surfaces into classical flow theory, the interSection of which may form corners and vertices.

Lin (1954, 1958) presented a slip model with experimental an uniaxial stress-strain-curve and was able to calculate the effective elastic-plastic response of a polycrystalline material and to compare with experiments. As a consequence, he claimed the existence of corners in the macroscopic yield surface.

A similar presentation was given by Sanders Jr. (1954). Extrapolating the results by Koiter (1953) to an infinite number of mechanisms, he showed the existence of a rounded initial yield surface and the composition of subsequent yield surfaces by part of the initial surface and a developing vertex that could be approximated by a cone the tip of which is the preloading point. In addition he made the transition from focussing on the irregular shape of the yield surface to the implications on the flow rule. In contradiction to a plasticity theory with a smooth yield surface, a direction of the plastic flow that is fixed in a process-independent way cannot be expected.

2.2.3 Experimental research

A number of investigations attempted to provide experimental evidence for yield vertices. Clearly, multiaxial tests are necessary for such experiments. Phillips (1960) proposed stress controlled combined tension-torsion experiments on thin-walled aluminum tubes. A stress path oscillating in a zig-zag manner around a mean direction indicated strongly process-dependend strain rates as expected if *"the path of loading carries a pointed or sharply rounded vertex with it"* due to the changes in the yield surface normal.

Bertsch and Findley (1962) presented a theoretical analysis, according to which typical *intrinsic* corners move along the stress path instead of being traced by the stress point while moving along the yield surface. Their experimental results left questions open that were augmented by a detailed discussion of the definition of yield and its influence on the results. Indeed, it will be shown in Chapter 5 that the shape of the yield surface and the existence of a pointed vertex depends on the definition of the critical quantity that indicates plastification. In particular the choice of the threshold is of importance.

Cruciform planar specimens were used by Shiratori and Ikegami (1968). Subsequent yield surfaces clearly exhibit corners. Their experiments with zig-zag loading were less clear. Here, the yield point is defined by a small offset strain of $\epsilon_p = 0.0001$.

Hecker (1971, 1972) pointed out the influence of the definition of the yield point. He used a combined tension-internal-pressure machine and a copper spec-

imen. Large offset strains ($\epsilon_p = 0.002$) tend to wipe out the finer contributions of the plastic anisotropy leaving only gross effects like isotropic and kinematic hardening. At small proof strains ($\epsilon_p = 5 \cdot 10^{-6}$) the curvature of the yield surface increases by the negative cross effect. However, no corners have been found. The importance of including the physical background into the mathematical models of plasticity is stressed in the summary. In particular the yield stress drop in reloading (Phillips and Sierakowski, 1965) is explicitly named as a factor able to erase corners that have developed.

By usage of a computer controlled testing machine Gupta and Lauert (1983) obtained subsequent yield surfaces for different proof strains by radial probing. They showed that very sensitive testing ($\epsilon_p = 0.0001$) exhibits a vertex, while for only slightly larger proof strain this is not the case. In addition a degression opposite to the vertex is found.

Reviews on experimental results that include the question of existence of corners are given by Hecker (1976) (who gives a huge classified overview on experimental papers) and Ikegami (1982).

Besides the question of the special shape of yield surfaces due to the corners, the implications for the plastic flow gained increasing interest in later publications. Starting with Lensky (1960) whose experimental results for non-proportional stress trajectories resulted in the delay phenomenon: After deviation from a proportional path a continuation of the process in a constant direction of plastic flow with some additional plastic strain is needed to obtain a stress process that runs straightly in the new normality direction. Such effects are crucial for macroscopic vertex theories of plasticity that concentrate on an improved formulation of the flow rule being able to predict such effects.

2.2.4 Computational approaches

Computational methods improved the knowledge from their first usage on. First investigations were possible with the polycrystal model by Lin and Ito (1966), which used simplified assumptions (isotropy, single slip in a grain) to obtain an analytical solution. He found a vertex in the subsequent yield surfaces if the occurence of the first active slip system was taken as a criterion. A comparison with experimental yield surfaces for larger plastic proof strains show a replacement of the vertex with a rounded area of high curvature.

The non-smoothness of the yield surface in an improved theoretical setting was shown by Hutchinson (1970). Using a self-consistent method, initial and subsequent yield surfaces for f.c.c. crystals were computed, assuming that the yielded grain is completely surrounded by an elastic matrix. The results show a clear corner. The yield surface is defined by the first occurrence of slip in any grain.

A self-consistent model was used by Kiryk and Petryk (1998) to calculate isolines of the viscous flow potential. Subsequent yield surfaces carry a vertex. A comparison with experiments is given.

Kraska (1998) computed the yield-surface of polycrystals using a finite-element discretization. Distortional hardening and vertex-like structures can

be found in his Fig. 7.26 for small thresholds of dissipated power, although not mentioned by the author. His approach will be used in Chapter 5 for determination of important vertex parameters.

Zattarin et al. (2004) used a nonlinear self-consistent polycrystal model to predict the evolution of yield surfaces. They compared their results with experiments by Boucher et al. (1992). The distortional hardening demonstrates primary and secondary rounded vertices and is mainly attributed to second order internal stresses, but this result is only based on the relative smallness of plastic strain. However, our findings in Chapter 5 suggest a more prominent influence of the crystallographic texture.

2.2.5 Construction of material models

A general discussion of materials with a micro-macro scale transition led Hill (1967) to the conclusion that in a strict sense, corners *must* exist in yield surfaces (even in the isotropic case with smooth yield surfaces for the microscopic entities).

Sewell (1974) proposed a plastic flow theory using a 3-surface vertex as in a multisurface model. It takes up the structure of the crystal plasticity proposed by Mandel (1965).

For the analysis of localization of deformation in brittle rock materials, the development of vertex-like structures on the yield surface were investigated by Rudnicki and Rice (1975). These are shown to destabilize the material behaviour. Deformation theory of plasticity is interpreted as vertex development for full loading.

Localization of biaxially stretched metal sheets at earlier strain levels than expected can be explained by the vertex formation (Stören and Rice, 1975). Initial imperfections (Marciniak and Kuczynski, 1967) need too strong intensities for giving realistic results when the yield surface is assumed to be smooth. Again, the deformation theory of plasticity has been used to model the vertex effect. In contrast to the flow theory, it does not exhibit a excessive lateral incremental modulus, a fact which has been interpreted as a direction-dependent plastic modulus as connected with the vertex effect.

Christoffersen and Hutchinson (1979) continued in this direction. By a short review of results on the stability of plastic structures it is demonstrated that flow theories with a smooth yield surface do not agree with experiments in that point. An incremental J_2 vertex theory is presented making use of a convex stress rate potential that contains the usual quadratic ansatz multiplied by a scalar function of the angle between the axis of the conical vertex and the stress rate, separating total loading or fully active range (identified with J_2 deformation theory), unloading, and partial loading in between.

These results were further refined in Hutchinson and Tvergaard (1981). By a comparison of different theories (nonlinear elasticity, i.e. J_2 deformation theory), kinematic hardening plasticity and plasticity with yield surface corner development), the influence of the corner angle and the size of the total loading range on the bifurcation and imperfection sensitivity have been studied showing

that blunt corners decrease the imperfection sensitivity as well as a smaller total loading range.

In a series of articles Gotoh (1985a,c) introduced a general incremental plastic law based on isotropic representation theorems that depends explicitly on the angle between stress tensor and stress increment. This dependence has been chosen as to reduce to J_2 deformation theory for the case of proportional loading and to purely elastic behavior for large angles. Hence a vertex is incorporated. Gotoh (1985b) is supplemented with a calculation of the stress response in non-proportional strain paths. It is shown to exhibit the delay effect (Lensky, 1960).

Goya and Ito (1991) presented a corner theory based on the incremental moduli. Stress- and strain-rate-dependend functions were used to weaken the moduli. In addition, the process direction itself has been shown to be of interest and included in an extended version (Ito et al., 1992). An FE polycrystal model was used to identify parameters of a macroscopic model. 64 grains were used, and the model includes two extra parameters for the influence of non-normality effects (Goya and Ito, 1997).

A framework for the enhancement of classical (smooth) plasticity theories with the corner effect was proposed by Petryk and Thermann (1997) A two surface model is modified in order to introduce the corner effect by the inner yield surface while the outer loading surface is defined by a smooth analytical formula. The plastic compliances are assumed to depend on the angle of the stress rate and the corner tip. Micromechanical considerations lead to the derived transition function for partial unloading. The reference strain rate for proportional loading depends on the distance from loading surface. In the proposed most simple version, only one additional parameter is needed, the maximum cone angle at the yield surface vertex. Isotropy is assumed for the elastic behavior. The loading surface behaves like in the J_2 flow theory with kinematic and isotropic hardening, but could be replaced by any other suitable smooth law.

Hu et al. (1998) proposed a theory based on an evolution law for Young's modulus and Poisson's ratio, called J_2 Quasi-Flow Corner Theory. It seems to improve the smooth transition from plastic loading to elastic unloading at the localization point. It was used with a Barlat-Lian type of anisotropic yield function (Hu et al., 2001).

A series of papers (Kuroda and Tvergaard, 1999, Kuwabara et al., 2000, Kuroda and Tvergaard, 2001a,b) proposed to describe the yield surface in the vicinity of the prestress point by an abrupt modification of strain rate. It is shown analytically that this corresponds to a resulting stress trajectory that is very close to the yield surface (Kuroda and Tvergaard, 1999). For a 160 grain Taylor-type polycrystal model, the method has been used for the determination of subsequent yield surfaces that exhibit a clear corner. The comparison with offset strain-based yield surfaces shows that the strain path change gives a better approximation. It is argued, that the strain path change exhibits corners that are erased by a yield surface probing experiment through unloading (Hecker, 1976). In an experimental study using cruciform specimens (Kuwabara et al., 2000), the predictions have been confirmed while offset strain yield curves show no or only blunted corners.

Kuroda and Tvergaard (2001a) proposed a phenomenological elastically isotropic plasticity model based on a viscoplastic overstress law and a smooth while anisotropic dynamic yield surface. Its shape is given by an approach of Barlat and Lian (1989), employing an exponential parameter to adapt the yield surface radii. In contradiction to classical approaches, normality is not preassumed, but an explicit dependence of the plastic strain rate on the tangential part of total strain rate is assumed. By this approach a vertex-like behavior is modelled also for a smooth yield surface. The reason is that yield surfaces widely used in application are based on a small but finite offset strain. Thus the existence of a vertex is not obvious. Comparison with a Taylor model of 800 grains is used in terms of a 2D forming limit diagram (FLD) to adapt the parameters.

Tsutsumi and Hashiguchi (2005) proposed a non-normality flow rule that has originally been intended for granular media. In addition to a normal contribution, "loading to the side" generates an additional component of the plastic strain rate that is parallel to the yield surfaces.

Yet there is no widely accepted model for plastic materials exhibiting the vertex effect, even in the case of small strain.

2.2.6 Application

Early contributions mentioned the occasional failure of J_2 flow theory to describe buckling phaenomena properly (Gerard and Becker, 1957). Often, imperfections are needed that can exceed realistic levels (Stören and Rice, 1975, Hutchinson and Budiansky, 1976, Hutchinson and Tvergaard, 1981). An important issue is the prediction of forming limits that is improved by the inclusion of the vertex effect into the considerations (Stören and Rice (1975), Petryk and Thermann, 1996, Kuroda and Tvergaard (2001a), Hu et al. (2001), Stoughton and Zhu (2004)).

2.3 Overview and main results

In Part I, the theoretical background of this work is given. Chapter 3 contains the fundamental equations of continuum mechanics, while in Chapter 4 the theory of plastic materials is considered.

In Section 4.3, plastic materials with multiple mechanisms are investigated. The well-known resulting formulae are compared with regularized approaches to such materials (presented in Section 4.4).

They differ due to the intersection of multiple yield surfaces at one point, called a *vertex*. The resulting difference of the flow rules is called *vertex effect* and discussed in Section 4.5. It is shown (Section 4.5.2), that it is mainly due to two facts:

1. The rank of certain linear operators is 1 for a single mechanism (regularized) and larger for multiple mechanisms. Thus the flow rules depend on the strain rate direction in different linear ways. The nondefective

eigenspace of the regularized operator is contained in the nondefective eigenspace of the multi-mode operator.

2. Successive unloading leads to different active sets in different process directions. Each of these disjoint cones in the strain rate space deserves a separate treatment. Thus a nonlinear dependence of the flow rule on the strain rate is the case.

If the information about the active set of mechanisms is included in the dependencies of a single plastic potential, the vertex effect can be predicted. In particular, plastic flow components parallel to the regularized yield surface as found in the multi mode plasticity theory, can be obtained by this approach.

In accordance with problems in the experimental investigation, the existence of corners in yield surfaces is shown by a micro-macro simulation based on the Taylor-Lin model in Chapter 5. Two different indicators are compared and the development of the vertex – in particular the corner angle – as a function of accumulated strain, on one- and two-staged process paths is obtained from the data.

It is concluded that at strains of an order of magnitude as technical proof strains, vertices in the yield surface are well developed and follow the stress point immediately (traveling vertex). Thus in a macroscopic theory, the vertex effect may be included without a separate theory for the vertex evolution, considerably simplifying the matter.

Chapter 6 deals with a macroscopic vertex model of plasticity based on these findings. A single plastic potential including two transition functions to model the successive unloading of mechanisms and their influence on the dissipation as well as on the direction of plastic flow is introduced. The transition functions incorporate the influence of the process continuation on the plastic flow. They are chosen to approximate simulations with the Taylor-Lin model (Section 6.4). The results of the J_2 flow theory are considerably improved both in terms of the dissipation and the direction of plastic flow. Both are connected with the incremental moduli of the material model that are corrected for non-proportional processes.

The ability of the proposed theory to predict the behaviour of a plastic material in the sequel of a kinked process path is shown by a comparison with experiments in Section 6.5. The delay effect investigated by Lensky (1960) can be reproduced better than by the J_2 flow theory. It is worth mentioning, that this is not paid for by largely increased numerical costs.

As a structural example, the torsional buckling of a cruciform column is the subject of Section 7. The J_2 flow theory and its excessive lateral stiffness tends to overestimate the buckling load. By the proposed theory this problem can be overcome. Its formulation enables the usage of an incremental directionally quadratic rate potential. It is used to interpret the critical buckling load at which the nature of the quadratic form changes from elliptic to hyperbolic, leading to an instable incremental deformation in the sense of the energy criterion (Petryk, 1991).

It is shown that the proposed theory is able to reproduce the experimental data reported by Gerard and Becker (1957) without relying on strong geometric imperfections like Hutchinson and Budiansky (1976) or finite timesteps as Papadopoulos and Lu (1998).

Both analytical and numerical results are presented.

2.4 Notation

Vectors and second order tensors are denoted by bold lower and upper case letters, $\mathbf{a} = a_i \mathbf{e}_i$, $\mathbf{A} = a_{ij} \mathbf{e}_i \otimes \mathbf{e}_j$, while their components are denoted by lower case italic letters having the according number of indices. The summation convention is used for double latin indices unless explicitly excluded. The application and composition has no extra symbol, $\mathbf{Av}$, $\mathbf{AB}$. Fourth order tensors are denoted such as $\mathbb{C} = c_{ijkl} \mathbf{e}_i \otimes \mathbf{e}_j \otimes \mathbf{e}_k \otimes \mathbf{e}_l$ and their application by brackets, $\mathbf{A} = \mathbb{C}[\mathbf{B}]$. A dot symbolizes the inner product of the according vectors or tensors, $\mathbf{A} \cdot \mathbf{B} = a_{ij} b_{ij}$.

For push-forward operations, the Rayleigh product is frequently used in the following form $(\mathbf{A} \otimes \mathbf{B} \otimes \mathbf{C} \otimes \mathbf{D}) \star \mathbb{C} = c_{ijkl} (\mathbf{A}\mathbf{e}_i) \otimes (\mathbf{B}\mathbf{e}_j) \otimes (\mathbf{C}\mathbf{e}_k) \otimes (\mathbf{D}\mathbf{e}_l)$, for short, $(\mathbf{A} \otimes \mathbf{B}) \star \mathbb{C} = (\mathbf{A} \otimes \mathbf{B} \otimes \mathbf{A} \otimes \mathbf{B}) \star \mathbb{C}$ and $\mathbf{A} \star \mathbb{C} = (\mathbf{A} \otimes \mathbf{A} \otimes \mathbf{A} \otimes \mathbf{A}) \star \mathbb{C}$.

Part I

THEORETICAL FOUNDATIONS

3. GENERAL ASPECTS OF CONTINUUM MECHANICS

3.1 Kinematics of continua

Section Overview
In this Section the basic terms of the description of the motion of continuous media are introduced, including the strain measures, and different placements. See Leigh (1968), Marsden and Hughes (1994), Bertram (2005) or others for details.

3.1.1 Placement and motion

The basic assumption of continuum mechanics is the continuous distribution of matter. This means that the existence of atoms –quanta of matter– is neglected. Instead, each body is thought about as a differentiable manifold, parametrized by a number of three parameters, X_i, $i = 1 \dots 3$. Each triple (X_1, X_2, X_3) intrinsically adresses a point P.

At each time t, the body occupies a closed region of the physical Euclidean space $\mathcal{E}$. For each point (X_1, X_2, X_3), its *placement* in $\mathcal{B}_t \subseteq \mathcal{E}$, $\boldsymbol{\kappa}_t$ is defined by

$$\begin{array}{rrl} \boldsymbol{\kappa}_t : & \mathbb{R}^3 & \to \mathcal{E}, \\ & (X_1, X_2, X_3) & \mapsto \mathbf{x}_t. \end{array} \tag{3.1}$$

This placement is referred to as the *actual placement*, and $\mathbf{x}_t$ the *spatial* position vector of P. Placements can also be defined if they are never actually attained by the body. Thus one can arbitrarily introduce a *reference placement* $\boldsymbol{\kappa}_0$ leading to the *material* position vector, $\mathbf{x}_0 = \boldsymbol{\kappa}_0(X_1, X_2, X_3)$. To describe the *motion* of a body, the reference placement is often utilized to eliminate the intrinsic coordinates with the material position vector.

$$\begin{array}{rrl} \boldsymbol{\chi} : & \mathcal{B}_0 \times \mathbb{R} & \to \mathcal{E}, \\ & (\mathbf{x}_0, t) & \mapsto \boldsymbol{\kappa}_t \circ \boldsymbol{\kappa}_0^{-1}(\mathbf{x}_0). \end{array} \tag{3.2}$$

Here, $\mathcal{B}_0 \subseteq \mathcal{E}$ and $\mathcal{B}_t \subseteq \mathcal{E}$ are the volumes occupied by the body in the two placements, respectively.

The deformation of a body can also be described without relying on the arbitrary introduction of a reference placement. In that case, instead of position vectors the parametrization of the manifold (X_1, X_2, X_3) is used. Accordingly, a clear distinction between the elements of the tangential space and the dual space makes the transformation rules for different objects clear: Vectors have

to be transformed as in (3.4), while covectors (one-forms) transform according to (3.5) (Krawietz, 1986, Bertram, 1989, Marsden and Hughes, 1994).

3.1.2 Deformation and strain measures

In the description of material behaviour, the *deformation gradient*

$$\mathbf{F} = \mathrm{Grad}\boldsymbol{\chi}(\mathbf{x}_0, t) = \boldsymbol{\chi}(\mathbf{x}_0, t) \otimes \nabla_0. \tag{3.3}$$

is the fundamental measure of how a body transforms locally. In rigid body translation it is the identity. $\mathbf{F} \in L^+$ is a second order two point tensor. It maps line elements (vectors) associated with the reference placement to such associated with the actual placement. Thus, in a thorrow notation, it is a map from the local tangent space of the undeformed body to the local tangent space of the deformed body.

$$\mathbf{d}_t = \mathbf{F}\mathbf{d}_0 \tag{3.4}$$

Nanson's formula (also called Piola transform by Marsden and Hughes (1994)) does the same for elements of surface (covectors), using the *cofactor*,

$$\mathbf{n}_t \mathrm{d}A_t = J\mathbf{F}^{-T}\mathbf{n}_0 \mathrm{d}A_0. \tag{3.5}$$

While $\mathbf{F}$ has no special symmetry properties, the impermeability of matter requires its *Jacobian* $J = \frac{\mathrm{d}V_t}{\mathrm{d}V_0}$ that transforms volume element from the reference to actual placement to be positive,

$$J = \det \mathbf{F} > 0. \tag{3.6}$$

The *polar decomposition* theorem allows for the split between rotation and stretch,

$$\mathbf{F} = \mathbf{R}\mathbf{U} = \mathbf{V}\mathbf{R}, \tag{3.7}$$

introducing the *rotation tensor* $\mathbf{R}$ and the *right and left stretch tensors*, $\mathbf{U}$ and $\mathbf{V}$, respectively. The latter are constant in rigid body rotations. Both decompositions are of equal importance. Here, $\mathbf{U} = \sqrt{\mathbf{C}}$. This tensor function is computed via the singular values of $\mathbf{F}$, the eigenvalues of

$$\mathbf{C} = \mathbf{F}^\top \mathbf{F}. \tag{3.8}$$

$\mathbf{C}$ is called *right Cauchy-Green tensor*. Then (3.7) can be solved for $\mathbf{R}$ and $\mathbf{V}$. For practical applications, an iterative algorithm proposed by Higham (1986) is superior to the classical approach based on singular value decomposition.

Suitable functions $\mathbf{E}_{(n)}$ of $\mathbf{U}$ and $\mathbf{V}$ can be used as *measures of strain*. An overview is given in the textbooks by Lubarda (2002), or Bertram (2005). Some measures of deformation used in this work are summarized in Table 3.1 on page 30.

Another description, how a material point $\mathbf{x}_0 = \boldsymbol{\kappa}_0(P)$ moves, is the *displacement* vector $\mathbf{u}(\mathbf{x}_0, t) = \boldsymbol{\chi}(\mathbf{x}_0, t) - \mathbf{x}_0$. Its gradient

$$\mathbf{H} = \mathbf{F} - \mathbf{1} \tag{3.9}$$

is used to judge the magnitude of deformation. *Small deformations* are characterized by $\|\mathbf{H}\| \ll 1$. Here, the *Frobenius norm* $\|\mathbf{A}\| = \sqrt{\mathbf{A} \cdot \mathbf{A}}$ is used.

In the case of small deformations, the strain tensors converge, by linearization,

$$\mathbf{E}_{(n)} \approx \boldsymbol{\epsilon} = \frac{1}{2}\left(\mathbf{H} + \mathbf{H}^{\top}\right). \tag{3.10}$$

In problems varying with time, the rate of deformation is needed. Taking the time derivative of $\mathbf{F}$, the material velocity gradient is obtained. In a spatial description, the chain rule yields the *spatial velocity gradient*.

$$\mathbf{L} = \mathbf{v}(\mathbf{x}_t, t) \otimes \nabla = \dot{\mathbf{F}}\mathbf{F}^{-1}. \tag{3.11}$$

Introducing the stretching and the spin tensor,

$$\begin{aligned} \mathbf{D} &= \frac{1}{2}(\mathbf{L} + \mathbf{L}^{\top}) \\ \mathbf{W} &= \frac{1}{2}(\mathbf{L} - \mathbf{L}^{\top}), \end{aligned} \tag{3.12}$$

the rates of the different strain tensors can be written as linear functions of $\mathbf{D}$, like for Green's strain

$$\begin{aligned} \mathbf{E} &= \mathbf{E}_{(1)} = \frac{1}{2}(\mathbf{C} - \mathbf{1}) \\ \dot{\mathbf{E}} &= \mathbf{F}^{\top}\mathbf{D}\mathbf{F}, \end{aligned} \tag{3.13}$$

showing that the stretching tensor $\mathbf{D}$ can be considered the fundamental measure of strain rate.

3.1.3 Change of reference placement

If instead of $\boldsymbol{\kappa}_0$ another reference placement $\boldsymbol{\kappa}_1$ has been chosen, also the motion is affected.

$$\boldsymbol{\chi}_1 = \boldsymbol{\kappa}_t \circ \boldsymbol{\kappa}_1^{-1} = \boldsymbol{\kappa}_t \circ \boldsymbol{\kappa}_0^{-1} \circ \boldsymbol{\kappa}_0 \circ \boldsymbol{\kappa}_1^{-1} = \boldsymbol{\chi} \circ \boldsymbol{\chi}_{01}, \tag{3.14}$$

i.e. the motion $\boldsymbol{\chi}$ is preceded by the relative motion from the new to the original reference placement. Accordingly, the deformation gradient is

$$\mathbf{F}_1 = \boldsymbol{\chi} \otimes \nabla_1 = \mathbf{F}\mathbf{F}_{01} \tag{3.15}$$

where $\mathbf{F}_{01} = \boldsymbol{\chi}_{01} \otimes \nabla_1$.

Thus if we combine the motions between different placements, the according deformation gradients as tangent maps combine multiplicatively. The displacement is additive,

$$\mathbf{u}_1 = \boldsymbol{\chi} - \mathbf{x}_1 = \mathbf{u} + \mathbf{u}_{01} \tag{3.16}$$

while the displacement gradient is not.

$$\mathbf{H}_1 = \mathbf{F}_1 - \mathbf{1} = \mathbf{u} \otimes \nabla_1 + \mathbf{u}_{01} \otimes \nabla_1 = \mathbf{H}\mathbf{F}_{01} + \mathbf{H}_{01}. \tag{3.17}$$

Only if the change of reference placement includes small deformations, $\mathbf{F}_{01} \approx \mathbf{1}$ and the displacement gradients can be added in good approximation.

The same applies to the strain tensors that result from the two motions. In small deformations they are additive. In general, that property does not hold.

3.2 Dynamics of continua

Section Overview
In this Section, the dynamics of continua are introduced, including balance equations, fluxes and productions. Textbooks including details are Müller (1985), Bertram (2005), amongst others. Different stress measures are introduced.

3.2.1 Spatial balance equations

According to the assumptions of continuum mechanics, for extensive quantities balance equations can be applied to each subset of the body $\mathcal{B}_t^i \subseteq \mathcal{B}_t$. The equations for the mass density ρ_t, the mass-specific linear momentum $\dot{\mathbf{u}}$, the mass-specific angular momentum $\mathbf{x} \times \dot{\mathbf{u}}$, and the mass-specific internal energy ϵ can be brought to the following local form:

$$\frac{\rho_0}{\rho_t} = J \tag{3.18}$$

$$\rho_t \ddot{\mathbf{u}} + = \mathrm{div}\mathbf{T} + \rho_t \mathbf{b} \tag{3.19}$$

$$\mathbf{T} = \mathbf{T}^\top \tag{3.20}$$

$$\rho_t \dot{\epsilon} = -\mathrm{div}\mathbf{q} + \mathbf{T} \cdot \mathbf{D} + \rho_t r \tag{3.21}$$

In these spatial formulations, the substantial time derivative $\dot{a}_t = \frac{\partial a}{\partial t} + \mathrm{grad}a \cdot \mathbf{v}$ is used. The nonconvective spatial flux of momentum in (3.19), $\mathbf{T}$, is called Cauchy stress. According to (3.20), for classical (non-Cosserat) continua, it is a symmetric second order tensor. The according source term $\mathbf{b}$ is called body force. In (3.21), the heat flux $\mathbf{q}$, the internal stress power $\mathbf{T} \cdot \mathbf{D}$ per unit volume and the radiation term r can be found.

In the derivation, the regularity of the field quantities is necessary. In places, where the Gauss theorem cannot be used, *jump equations* apply. See Krawietz (1986), Petryk (1998) for a discussion of this point.

3.2.2 Material balance equations

By application of the transformation rules for elements of surface (3.5) and volume (3.6), material balance equations for linear and angular momentum, and internal energy can be formulated.

$$\rho_0 \ddot{\mathbf{u}} = \mathrm{DIV}\mathbf{T}_0 + \rho_0 \mathbf{b} \tag{3.22}$$

$$\mathbf{T}_0 \mathbf{F}^\top = \mathbf{F}\mathbf{T}_0^\top \tag{3.23}$$

$$\rho_0 \dot{\epsilon} = -\mathrm{DIV}\mathbf{q}_0 + \mathbf{T}_0 \cdot \dot{\mathbf{F}} + \rho_0 r \tag{3.24}$$

The time rate simplifies to the material time derivative, $\dot{a} = \frac{\partial a}{\partial t}$. Here, the nonconvective material flux of momentum $\mathbf{T}_0 = J\mathbf{T}\mathbf{F}^{-\top}$ is the First Piola-Kirchhoff stress tensor. Instead of the symmetry, (3.23) applies. $\mathbf{q}_0 = J\mathbf{q}\mathbf{F}^{-\top}$ is the material heat flux.

Either version of the field equations leaves the closure problem open: The 5 field equations contain 14 variables, $(\rho_t, \epsilon, \mathbf{u}, \mathbf{q}, \mathbf{T})$ in the actual placement or 13 variables $(\epsilon, \mathbf{u}, \mathbf{q}_0, \mathbf{T}_0)$ in 4 equations in the reference placement. In addition, the temperature Θ is a constitutive variable.

Restricting ourselves to the isothermal case $\Theta = \text{const}$, we shall proceed with the derivation of a set of constitutive equations that close that problem and describe materials with elastic-plastic properties including the vertex effect.

3.2.3 Work conjugate stress and strain measures

The balance of internal energy (3.21) or (3.24) is the key for the introduction of stress measures. A strain tensor $\mathbf{E}^x$ and a stress tensor $\mathbf{S}^x$ are *work conjugate*, if their inner product equals the stress power per unit reference volume, using thus the Kirchhoff stress $\boldsymbol{\tau} = J\mathbf{T}$,

$$\mathbf{S}^x \cdot \dot{\mathbf{E}}^x = \boldsymbol{\tau} \cdot \mathbf{D} = \mathbf{T}_0 \cdot \dot{\mathbf{F}}. \tag{3.25}$$

In particular, for invertible tensors $\mathbf{A}$ and $\mathbf{B}$,

$$\dot{\mathbf{E}}^x = \mathbf{A}^\top \mathbf{D}\mathbf{B}, \tag{3.26}$$

which includes the rates $\dot{\mathbf{E}}_{(n)}$, the work conjugate stress tensor is

$$\mathbf{S}^x = \mathbf{A}^{-1}\boldsymbol{\tau}\mathbf{B}^{-\top}. \tag{3.27}$$

For $\mathbf{A} = \mathbf{B} = \mathbf{F}$ the stress tensor is pulled back to the reference placement, accounting for the mixedvariant nature of the according slots. We obtain

$$\boldsymbol{\tau} \cdot \mathbf{D} = \mathbf{S} \cdot \dot{\mathbf{E}}, \tag{3.28}$$

introducing the second Piola-Kirchhoff stress $\mathbf{S} = \mathbf{F}^{-1}\boldsymbol{\tau}\mathbf{F}^{-\top}$ as work conjugate to Green's strain. $\mathbf{S}$ maps the reference surface element covectors to reference stress vectors. Accordingly, $\mathbf{F}^\top\mathbf{D}\mathbf{F}$ maps reference vectors to reference velocity covectors.

On the other hand, for $\mathbf{A} = \mathbf{F}^{-\top}$ and $\mathbf{B} = \mathbf{F}$, the pull-back transformation is applied to the covariant stretching tensor.

$$\boldsymbol{\tau} \cdot \mathbf{D} = \mathbf{F}^\top\boldsymbol{\tau}\mathbf{F}^{-\top} \cdot \mathbf{F}^{-1}\mathbf{D}\mathbf{F} = \mathbf{C}\mathbf{S} \cdot \mathbf{F}^{-1}\mathbf{D}\mathbf{F}. \tag{3.29}$$

(3.29) introduces the Mandel stress $\mathbf{CS}$, but does not define a strain tensor.

$$\mathbf{F}^{-1}\mathbf{D}\mathbf{F} = \text{sym}\mathbf{F}^{-1}\dot{\mathbf{F}}, \tag{3.30}$$

The result is the material gradient of the pulled-back velocity, mapping reference vectors into reference vectors. The pull-back of the deformed metric, $\mathbf{C}$, is thus used to lower one index in $\mathbf{CS}$ being a map of reference covectors.

Some other useful notations are summarized in Table 3.1.

Deformation Gradient	$\mathbf{F}$	$\mathbf{T}_0 = J\mathbf{T}\mathbf{F}^{-\top}$	First Piola-Kirchhoff stress
linear strain	$\boldsymbol{\epsilon}$	$\mathbf{T}$	Cauchy stress
Green strain	$\mathbf{E} = \frac{1}{2}(\mathbf{F}^\top\mathbf{F} - \mathbf{1})$	$\mathbf{S} = J\mathbf{F}^{-1}\mathbf{T}\mathbf{F}^{-\top}$	Second Piola-Kirchhoff stress
Almansi strain	$\mathbf{E}^A = \frac{1}{2}(\mathbf{1} - \mathbf{F}^{-1}\mathbf{F}^{-\top})$	$\boldsymbol{\tau}$	Kirchhoff stress
Hencky strain	$\mathbf{E}^H = \ln\sqrt{\mathbf{F}^\top\mathbf{F}}$	$\approx \mathbf{R}^\top\boldsymbol{\tau}\mathbf{R}$	rotated Kirchhoff stress

Tab. 3.1: Stress and strain measures

3.3 The second law of thermodynamics

The second law of thermodynamics is a restriction to processes possible in nature. Constitutive eqations must be carefully examined not to admit unphysical processes.

Amongst different formulations that are present in the standard literature, the Clausius-Planck equation for the *Helmholtz free energy* $\psi = \epsilon - \Theta\eta$,

$$\frac{1}{\rho}\mathbf{T}\cdot\mathbf{D} \geq \dot{\psi}. \tag{3.31}$$

ascertains in purely mechanical processes, that the dissipation is non-negative (Bertram, 2005, p. 152).

A more general approach can be found in Müller (1985) and has been taken up in a part of the newer literature (Müller and Ruggeri, 1993, Šilhavý, 1997, Wilmański, 1998). However, (3.31) is broad enough for the class of materials focussed on in this work.

4. RATE INDEPENDEND PLASTIC MATERIALS

4.1 Elastic properties

Section Overview
In this Section the elastic laws that shall be applied later are introduced. After a short introduction, we restrict ourselves to small elastic deformations. This restriction is justified for metals.

4.1.1 Hyperelastic laws

The behavior of elastic materials is instantaneous and reversible. Thus no influence of the past and no friction stresses are present. The Helmholtz free energy (suppressing the temperature-dependence in the isothermal case), is

$$\psi = \hat{\psi}_{\mathbf{F}}(\mathbf{F}). \tag{4.1}$$

It serves as a potential for the first Piola-Kirchhoff stress,

$$\mathbf{T}_0 = \rho_0 \frac{\partial \psi_{\mathbf{F}}}{\partial \mathbf{F}}. \tag{4.2}$$

For the function $\hat{\psi}_{\mathbf{F}}(\mathbf{F})$, the principles of material theory apply (Truesdell and Noll (1965), also Krawietz (1986), Bertram (2005)).

4.1.2 Principle of material objectivity

Application of the principle of material objectivity yields *reduced forms* for material equations, based on the assumption of Euclidean invariance of constitutive equations. For the free energy, we get as one possibility amongst others

$$\psi = \hat{\psi}_{\mathbf{C}}(\mathbf{C}) = \hat{\psi}_{\mathbf{F}}(\mathbf{F}). \tag{4.3}$$

4.1.3 Change of strain measure and reference placement

For other stress and strain measures, formulations equivalent to (4.2) can be found by application of the chain rule:

$$\begin{aligned}\mathbf{S}^x \cdot \dot{\mathbf{E}}^x &= \mathbf{T}_0 \cdot \dot{\mathbf{F}} \\ &= \rho_0 \frac{\partial \psi}{\partial \mathbf{F}} \cdot \left(\frac{\partial \mathbf{E}^x}{\partial \mathbf{F}}\right)^{-1} \circ \left(\frac{\partial \mathbf{E}^x}{\partial \mathbf{F}}\right)[\dot{\mathbf{F}}] \\ &= \rho_0 \left(\frac{\partial \mathbf{E}^x}{\partial \mathbf{F}}\right)^{-\top} [\frac{\partial \psi}{\partial \mathbf{F}}] \cdot \left(\frac{\partial \mathbf{E}^x}{\partial \mathbf{F}}\right)[\dot{\mathbf{F}}] \\ &= \rho_0 \frac{\partial \psi}{\partial \mathbf{E}^x} \cdot \dot{\mathbf{E}}^x\end{aligned} \tag{4.4}$$

The strain tensors change by a transition to another reference placement (see Section 3.1.3 on page 27). Accordingly, the free energy function, like all constitutive functions, depends on that choice.

$$\hat{\psi}_{\mathbf{F}\,1}(\mathbf{F}_1) = \hat{\psi}_{\mathbf{F}\,1}(\mathbf{F}\mathbf{F}_{01}) = \hat{\psi}_{\mathbf{F}\,0}(\mathbf{F}) \tag{4.5}$$

Releasing this dependence on the arbitrary unphysical reference placement is the advantage of an intrinsic formulation based on manifolds as presented in a couple of advanced textbooks (e.g. Krawietz, 1986, Bertram, 1989, Marsden and Hughes, 1994).

4.1.4 The general hyperelastic law

To obtain a hyperelastic law, we use the reduced form of the free energy (4.3),

$$\mathbf{S} = 2\rho_0 \partial_{\mathbf{C}} \psi \tag{4.6}$$

Thus the constitutive function for the stress can be deduced from the free energy,

$$\begin{aligned}\mathbf{S} &= k(\mathbf{C}), \\ k(\mathbf{C}) &= 2\rho_0 \partial_{\mathbf{C}} \hat{\psi}_{\mathbf{C}}(\mathbf{C}).\end{aligned} \tag{4.7}$$

We use k as symbol for the reduced form as we shall use it as the fundamental constituive law from which we derive equivalent formulations for other work conjugate measures, e.g.

$$\begin{aligned}\mathbf{S}^x &= \hat{\mathbf{S}}^x(\mathbf{E}^x) \\ \hat{\mathbf{S}}^x(\mathbf{E}^x) &= \rho_0 \partial_{\mathbf{E}^x} \hat{\psi}_{\mathbf{E}^x}(\mathbf{E}^x).\end{aligned} \tag{4.8}$$

4.1.5 Linear elastic laws

In the case of small deformations, linear elastic behavior means a linear law between the Cauchy stress and the linear strain tensor, using the fourth order *tensor of elastic moduli* $\tilde{\mathbb{C}}$ and the stress-free strain $\boldsymbol{\epsilon}_U$,

$$\hat{\mathbf{T}}(\boldsymbol{\epsilon}) = \tilde{\mathbb{C}}[\boldsymbol{\epsilon} - \boldsymbol{\epsilon}_U]. \tag{4.9}$$

The free energy that results in (4.9) via $\mathbf{T} = \partial_{\boldsymbol{\epsilon}}\psi$ is quadratic,

$$\hat{\psi}_{\boldsymbol{\epsilon}}(\boldsymbol{\epsilon}) = \frac{1}{2}(\boldsymbol{\epsilon} - \boldsymbol{\epsilon}_U) \cdot \tilde{\mathbb{C}}[\boldsymbol{\epsilon} - \boldsymbol{\epsilon}_U]. \tag{4.10}$$

The generalization for large deformations is nontrivial, as we could use any strain tensor to obtain a quadratic energy and a linear stress function. For other strain measures, additional dependencies on the deformation gradient may be obtained inducing a nonlinearity. Thus linear elasticity has no physical meaning in large strain problems without including the choice of stress and strain measure in the constitutive assumptions. However, if the elastic deformations are small, all strain tensors are equal to the linear strain tensor up to higher order terms, and a linear elastic law for any pair of conjugate stress and strain measures is justified.

In the sequel we shall use $\mathbf{S}$ and $\mathbf{E}$ as preferred measures and thus

$$\begin{aligned}
\hat{\psi}_{\mathbf{E}}(\mathbf{E}) &= \frac{1}{2}(\mathbf{E} - \mathbf{E}_U) \cdot \tilde{\mathbb{C}}[\mathbf{E} - \mathbf{E}_U], && (4.11)\\
\hat{\mathbf{S}}(\mathbf{E}) &= \tilde{\mathbb{C}}[\mathbf{E} - \mathbf{E}_U], && (4.12)\\
k(\mathbf{C}) &= \tilde{\mathbb{C}}[\frac{1}{2}(\mathbf{C} - \mathbf{1}) - \mathbf{E}_U]. && (4.13)
\end{aligned}$$

(4.13) shall prove to be of particular interest for the introduction of plastic behavior. In that case, the free energy has to be enhanced by additional terms.

Accordingly, for other stress measures we obtain by a simple transformation

$$\begin{aligned}
\mathbf{T}_0 &= \mathbf{F}\mathbb{C}[\mathbf{E} - \mathbf{E}_U]\\
&= (\mathbf{F} \otimes \mathbf{1}) \star \mathbb{C}[\frac{1}{2}(\mathbf{F} - \mathbf{F}^{-\top}) - \mathbf{F}^{-\top}\mathbf{E}_U]\\
\boldsymbol{\tau} &= \mathbf{F} \star \mathbb{C}[\mathbf{E}^A - \mathbf{F}^{-\top}\mathbf{E}_U\mathbf{F}^{-1}]\\
\mathbf{S}^x &= \mathbf{A}^{-1}\mathbf{F}\mathbb{C}[\mathbf{F}^\top\mathbf{A}^{-\top}\mathbf{E}^A\mathbf{B}^{-1}\mathbf{F} - \mathbf{E}_U]\mathbf{F}^\top\mathbf{B}^{-\top}\\
&= (\mathbf{A}^{-1}\mathbf{F} \otimes \mathbf{B}^{-1}\mathbf{F}) \star \mathbb{C}[\mathbf{A}^\top\mathbf{E}^A\mathbf{B} - \mathbf{A}^\top\mathbf{F}^{-\top}\mathbf{E}_U\mathbf{F}^{-1}\mathbf{B}].
\end{aligned} \tag{4.14}$$

and thus formally identical elastic laws, however, are not given in the respective work conjugate strain tensor (see Section 2.4 on page 22 for the usage of the Rayleigh product $\star$).

$(4.14)_{1-3}$ have in common that the elastic moduli, which are constant in (4.12), are functions of the deformation now.

4.1.6 Rate forms of the elastic law

Taking the time derivative of (4.12) or (4.14) and suitable transformations, we obtain rate forms of the elastic laws,

$$\begin{aligned}
\dot{\mathbf{S}} &= \hat{\mathbf{S}}(\dot{\mathbf{E}}) \\
\dot{\mathbf{T}}_0 - \mathbf{L}\mathbf{T}_0 &= (\mathbf{F}\otimes\mathbf{1}) \star \mathbb{C}[\dot{\mathbf{F}}] \\
\dot{\boldsymbol{\tau}} - \mathbf{L}\boldsymbol{\tau} - \boldsymbol{\tau}\mathbf{L}^\top &= \mathbf{F} \star \mathbb{C}[\mathbf{D}] \\
\dot{\mathbf{S}}^x - (\mathbf{A}^{-1}\mathbf{F})^\bullet(\mathbf{A}^{-1}\mathbf{F})^{-1}\mathbf{S}^x - \mathbf{S}^x\big((\mathbf{B}^{-1}\mathbf{F})^\bullet(\mathbf{B}^{-1}\mathbf{F})^{-1}\big)^\top & \\
= (\mathbf{A}^{-1}\mathbf{F}\otimes\mathbf{B}^{-1}\mathbf{F}) \star \mathbb{C}[\dot{\mathbf{E}}^x]. &
\end{aligned} \tag{4.15}$$

An alternative formulation for the stress rate in $(4.15)_3$ is

$$\ldots = \Phi \circ \frac{\mathrm{d}}{\mathrm{d}t}\Phi^{-1}[\mathbf{S}^x] \tag{4.16}$$

with the push-forward transformation

$$\Phi[\mathbf{C}] = \mathbf{A}^{-1}\mathbf{F}\mathbf{C}\mathbf{B}^{-1}\mathbf{F}, \tag{4.17}$$

which can be interpreted as a convective Lie rate (e.g. Marsden and Hughes, 1994) in the case $\mathbf{A} = \mathbf{B}$. Our formulation is also applicable for two point tensors. In particular for $(4.15)_3$ the upper Oldroyd rate of the Kirchhoff stress $\overset{\triangle}{\boldsymbol{\tau}}$ is obtained.

Starting from other elastic laws in a pair of work conjugate invariant stress and strain tensors, the ojective rate obtained for the Kirchhoff stress would be another one. Thus, we understand the choice of an objective rate for an incremental elastic law as a constitutive assumption like the choice of stress and strain tensors in a given form of elastic law. If the rate law is derived from a finite elastic law, all the alternatives are equally applicable. In such a manner, difficulties arising from hypoelastic formulations can be avoided. Nevertheless there is still an academic discussion on which objective rate is preferrable.

Obviously, the instantaneous elastic moduli tensors used in the rate laws (4.15) are the same as in the finite elastic laws $(4.14)_3$ derived by a mere push-forward operation. They can all be obtained as second derivatives of the free energy,

$$\mathbb{C}^x = (\mathbf{A}^{-1}\mathbf{F}\otimes\mathbf{B}^{-1}\mathbf{F}) \star \mathbb{C} = \partial^2_{\mathbf{E}^x}\hat{\psi}(\mathbf{E}^x). \tag{4.18}$$

From the reciprocal symmetry of the instantaneous moduli, a potential for the rate equations (4.15) is available. In that case,

$$\begin{aligned}
\dot{\mathbf{S}} &= \partial_{\dot{\mathbf{E}}}\mathcal{U} \\
\mathcal{U} &= \frac{1}{2}\dot{\mathbf{E}}\cdot\mathbb{C}[\dot{\mathbf{E}}].
\end{aligned} \tag{4.19}$$

The existence of such rate potentials is independend of the choice of the stress and strain measure. However, in contrast to the "physical" potential ψ, the rate

potential $\mathcal{U}$ changes with different choices (Lubarda, 2002, pp. 151ff).

$$\begin{aligned}
\dot{\mathbf{T}}_0 - \mathbf{L}\mathbf{T}_0 &= \partial_{\dot{\mathbf{F}}} \frac{1}{2}\dot{\mathbf{F}} \cdot (\mathbf{F} \otimes \mathbf{1}) \star \mathbb{C}[\dot{\mathbf{F}}] \\
\dot{\boldsymbol{\tau}} - \mathbf{L}\boldsymbol{\tau} - \boldsymbol{\tau}\mathbf{L}^\top &= \partial_{\mathbf{D}} \frac{1}{2}\mathbf{D} \cdot \mathbf{F} \star \mathbb{C}[\mathbf{D}] \\
\dot{\mathbf{S}}^x - (\mathbf{A}^{-1}\mathbf{F})^\bullet(\mathbf{A}^{-1}\mathbf{F})^{-1}\mathbf{S}^x - \mathbf{S}^x\big((\mathbf{B}^{-1}\mathbf{F})^\bullet(\mathbf{B}^{-1}\mathbf{F})^{-1}\big)^\top & \\
= \partial_{\dot{\mathbf{E}}^x} \frac{1}{2}\dot{\mathbf{E}}^x \cdot (\mathbf{A}^{-1}\mathbf{F} \otimes \mathbf{B}^{-1}\mathbf{F}) \star \mathbb{C}[\dot{\mathbf{E}}^x]. &
\end{aligned} \tag{4.20}$$

Although not being of much benefit for elastic problems, in the elastic-plastic regime certain useful applications exist.

4.1.7 Elastic isomorphy

Two elastic material points X and Y are called *elastically isomorphic* (Bertram, 2005, Sect. 6.4), if there exists an elastic isomorphism $\mathbf{K} \in L^+$ such that for the reference densities, and for the elastic laws for the second Piola-Kirchhoff stress $\mathbf{S}$, the following relation are valid:

$$\rho_{0X} = \rho_{0Y} \det \mathbf{K}, \tag{4.21}$$

$$k_Y(\mathbf{C}) = det\mathbf{K}\,\mathbf{K}k_X(\mathbf{K}^\top\mathbf{C}\mathbf{K})\mathbf{K}^\top, \qquad \forall \mathbf{F} \in L^+, \tag{4.22}$$

i.e. the elastic isomorphism behaves like the deformation gradient of a change of reference placement. However, it is not the gradient of any motion. For the material behavior in X and Y, arbitrary reference placements are allowed. $\mathbf{K}$ depends on the choice of the reference placements.

For linear elastic behaviour, we obtain from $(4.22)_2$

$$\mathbb{C}_Y[\frac{1}{2}(\mathbf{C}-\mathbf{1}) - \mathbf{E}_{UY}] = \det\mathbf{K}\,\mathbf{K}\mathbb{C}_X[\frac{1}{2}(\mathbf{K}^\top\mathbf{C}\mathbf{K}-\mathbf{1}) - \mathbf{E}_{UX}]\mathbf{K}^\top \qquad \forall \mathbf{C}, \tag{4.23}$$

which by comparison results in a transformation rule of the elastic moduli

$$\begin{aligned}
\mathbb{C}_Y &= \det\mathbf{K}\,\mathbf{K} \star \mathbb{C} \\
\mathbf{E}_{UY} &= \mathbf{K}^{-\top}\left\{\mathbf{E}_{UX} + \frac{1}{2}(\mathbf{K}^\top\mathbf{K} - \mathbf{1})\right\}\mathbf{K}^{-1}.
\end{aligned} \tag{4.24}$$

$(4.24)_2$ can be obtained from $(4.14)_3$ by setting $\mathbf{A} = \mathbf{F}\mathbf{K}$ and $\mathbf{B} = \det\mathbf{K}\,\mathbf{F}\mathbf{K}$. Thus, a second interpretation of the elastic isomorphism is a change of the constitutive variables while the elastic law is formally left identical.

Both interpretations underline the physical content of elastic isomorphisms: The two points have the same elastic behavior. This statement is in large deformation problems only possible after a transformation to appropriate reference placements and identical measures of strain.

4.1.8 Elastic symmetry

One important application of elastic isomorphism is in analyzing elastic symmetry. If a material point is elastically isomorphic to itself (automorphism), the elastic isomorphism is called a *symmetry transformation*. For $\mathbf{K} = \mathbf{Q} \in SO(3)$, we have $\det \mathbf{K} = 1$. Overviews can be found in many textbooks (e.g Hosford, 1993, Lubarda, 2002, Bertram, 2005).

4.2 Theory of plasticity based on isomorphisms

Section Overview
The main features of a plasticity theory based on isomorphisms are recalled (Bertram, 1992, 1999, 2005).

4.2.1 Isomorphisms between elastic laws

The fact that traveling dislocations leave the crystallographic lattice and, thus, elastic properties unchanged, is reflected by the introduction of isomorphic elastic laws before and after plastic deformation (yielding). In dependence on the plastic state to be introduced, the elastic law is

$$\mathbf{S} = k_P(\mathbf{C}). \tag{4.25}$$

For a (ficticious) plastic reference state denoted by a tilde, an *elastic reference law*

$$\mathbf{S} = \tilde{k}(\mathbf{C}) \tag{4.26}$$

is assumed. (4.25) and (4.26) are related by an elastic isomorphism according to (4.22).

$$k_P(\mathbf{C}) = \det \mathbf{P}\mathbf{P}\tilde{k}(\mathbf{P}^\top \mathbf{C}\mathbf{P})\mathbf{P}^\top. \tag{4.27}$$

The isomorphism operator $\mathbf{P} \in L^+$ is called *plastic transformation*.

Thus using the alternate interpretation of elastic isomorphism in Section 4.1.7, the constant elastic reference law can easily be formulated using $(4.14)_3$ and

$$\mathbf{A} = \mathbf{F}\mathbf{P} =: \tilde{\mathbf{F}}, \tag{4.28}$$

and

$$\mathbf{B} = \det \mathbf{P}\, \mathbf{F}\mathbf{P} = \det \mathbf{P}\tilde{\mathbf{F}}. \tag{4.29}$$

Equivalently,

$$\begin{aligned} \tilde{\mathbf{S}} &= \det \mathbf{P}\tilde{\mathbf{F}}^{-1}\boldsymbol{\tau}\tilde{\mathbf{F}}^{-\top} \\ \tilde{\mathbf{C}} &= \tilde{\mathbf{F}}^\top \tilde{\mathbf{F}} \\ \tilde{\mathbf{E}} &= \frac{1}{2}(\tilde{\mathbf{C}} - \mathbf{1}) \end{aligned} \tag{4.30}$$

introduces the quantities $\tilde{\mathbf{F}}$, $\tilde{\mathbf{S}}$, $\tilde{\mathbf{C}}$, $\tilde{\mathbf{E}}$. They are called the *elastic transformation*, the *elastic second Piola-Kirchhoff stress*, the *elastic right Cauchy-Green tensor*, and the *elastic Green's strain*.

$$\hat{\tilde{\mathbf{S}}}(\tilde{\mathbf{E}}) = \tilde{\mathbb{C}}[\tilde{\mathbf{E}}] \tag{4.31}$$

thus choosing the undistorted state $\tilde{\mathbf{E}}_U = \mathbf{0}$ as the reference state. (4.14) yields equivalent formulations for the elastic law,

$$\begin{aligned}
\hat{\mathbf{S}}(\mathbf{E}) &= \mathbf{P} \star \tilde{\mathbb{C}}[\mathbf{E} - \frac{1}{2}(\mathbf{P}^{-\top}\mathbf{P} - \mathbf{1})] \\
\hat{\mathbf{T}}_0(\mathbf{F}) &= (\tilde{\mathbf{F}} \otimes \mathbf{P}) \star \tilde{\mathbb{C}}[\frac{1}{2}(\mathbf{F} - \mathbf{F}^{-\top}) - \frac{1}{2}(\tilde{\mathbf{F}}^{-\top}\mathbf{P} - \mathbf{F}^{-\top})] \\
\hat{\boldsymbol{\tau}}(\mathbf{E}^A) &= \tilde{\mathbf{F}} \star \tilde{\mathbb{C}}[\mathbf{E}^A - \frac{1}{2}(\tilde{\mathbf{F}}^{-\top}\tilde{\mathbf{F}} - \mathbf{F}^{-\top}\mathbf{F}^{-1})] \\
\hat{\mathbf{S}}^x(\mathbf{A}^\top\mathbf{E}^A\mathbf{B}) &= (\mathbf{A}^{-1}\tilde{\mathbf{F}} \otimes \mathbf{B}^{-1}\tilde{\mathbf{F}}) \star \tilde{\mathbb{C}}[\mathbf{A}^\top\mathbf{E}^A\mathbf{B} - \frac{1}{2}(\mathbf{A}\tilde{\mathbf{F}}^{-\top}\tilde{\mathbf{F}}\mathbf{B} - \mathbf{A}\mathbf{F}^{-\top}\mathbf{F}^{-1}\mathbf{B})]
\end{aligned} \tag{4.32}$$

4.2.2 Derivation of the multiplicative split

The definition of the elastic transformation

$$\tilde{\mathbf{F}} = \mathbf{F}\mathbf{P} \quad \Rightarrow \quad \mathbf{F} = \tilde{\mathbf{F}}\mathbf{P}^{-1} \tag{4.33}$$

used above as a short-hand notation is the starting point for the vast majority of approaches to finite plasticity. In spite of a lack of clearness of the concept in early publications, the multiplicative split is well understood today (Lubliner, 1990, Bertram, 1999, Neff, 2000, Böhlke, 2001, Mielke, 2003, Bertram, 2005). The interpretation of an elastic isomorphism as a local change of reference placement according to the needs of simplification of elastic laws acknowledges the substantial parallelism between these two concepts.

For most practical applications both approaches can be stated as identical. Often the multiplicative split is apparently introduced based on kinematic arguments only. The isomorphy condition is however tacitly assumed by many authors.

The interpretation as a local (incompatible) placement is particular useful for a geometric interpretation of $\mathbf{P}$ and $\tilde{\mathbf{F}}$. Application of (3.4) and (3.5) shows that $\mathbf{P}$ transforms lattice vectors to the reference placement, $\mathbf{d}_0 = \mathbf{P}\tilde{\mathbf{d}}$, as well as covectors $\mathbf{n}_0 = \det\mathbf{P}\,\mathbf{P}^{-\top}\tilde{\mathbf{n}}$. Similarly, $\tilde{\mathbf{F}}$ acts in the actual placement, $\mathbf{d}_t = \tilde{\mathbf{F}}\tilde{\mathbf{d}}$, $\mathbf{n}_t = J\det\mathbf{P}\,\tilde{\mathbf{F}}^{-\top}\tilde{\mathbf{n}}$.

4.2.3 A kinematic split of the velocity gradient

By taking the time derivative,

$$\underbrace{\dot{\tilde{\mathbf{F}}}\tilde{\mathbf{F}}^{-1}}_{\tilde{\mathbf{L}}} = \underbrace{\dot{\mathbf{F}}\mathbf{F}^{-1}}_{\mathbf{L}} + \tilde{\mathbf{F}}\mathbf{P}^{-1}\dot{\mathbf{P}}\tilde{\mathbf{F}}^{-1}, \tag{4.34}$$

an apparently kinematically defined split of the spatial velocity gradient $\mathbf{L}$ can be found:

$$\mathbf{L} = \tilde{\mathbf{L}} - \tilde{\mathbf{F}}\mathbf{P}^{-1}\dot{\mathbf{P}}\tilde{\mathbf{F}}^{-1} \tag{4.35}$$

During elastic processes, the elastic law is unchanged, which leaves $\mathbf{P}$ constant. Accordingly, the second part in (4.35) is present in inelastic processes only, while in elastic ones $\tilde{\mathbf{L}} = \mathbf{L}$.

Plastic imcompressibility is achieved, if all volume changes are completely elastic in nature. As a consequence, $\mathrm{tr}\mathbf{P}^{-1}\dot{\mathbf{P}} = 0$ and thus $\det \mathbf{P} = 1$. Henceforth we shall assume this.

Inserting (4.35) into (3.25), the stress power can be split into an elastic (storage) and an inelastic (dissipational) part

$$\begin{aligned}\boldsymbol{\tau}\cdot\mathbf{L} &= \boldsymbol{\tau}\cdot\tilde{\mathbf{L}} - \boldsymbol{\tau}\cdot\tilde{\mathbf{F}}\mathbf{P}^{-1}\dot{\mathbf{P}}\tilde{\mathbf{F}}^{-1} \\ &= \tilde{\mathbf{F}}^{\top}\tilde{\mathbf{F}}\tilde{\mathbf{F}}^{-1}\boldsymbol{\tau}\tilde{\mathbf{F}}^{-\top}\cdot\left(\tilde{\mathbf{F}}^{-1}\dot{\tilde{\mathbf{F}}} - \mathbf{P}^{-1}\dot{\mathbf{P}}\right) \\ &= \tilde{\mathbf{C}}\tilde{\mathbf{S}}\cdot\tilde{\mathbf{F}}^{-1}\dot{\tilde{\mathbf{F}}} - \tilde{\mathbf{C}}\tilde{\mathbf{S}}\cdot\mathbf{P}^{-1}\dot{\mathbf{P}}.\end{aligned} \tag{4.36}$$

Here, the Mandel stress $\tilde{\mathbf{C}}\tilde{\mathbf{S}}$ has been shown to be power conjugate to $\tilde{\mathbf{F}}^{-1}\dot{\tilde{\mathbf{F}}} - \mathbf{P}^{-1}\dot{\mathbf{P}}$, the second of which is only present in inelastic processes.

Besides the plastic transformation $\mathbf{P}$, additional plastic hardening variables z (denoting symbolically a tuple of variables in the according spaces) shall be introduced. Also dual variables $g = \hat{g}(z)$ of the same rank and number as z are assumed that contribute energetically as $g \cdot \dot{z}$. We shall use z and g as generic vectorial representations of the respective variables, regardless of their tensorial rank and the operations $\cdot$ or $\otimes$ on these variables have to be read in an appropriate manner.

The evolution of the internal variables $\mathbf{P}$ and g is governed by the flow rule and the hardening rule. A general treatise of the description of inelasticity in the state space can be found in Bertram (2005, p. 244ff). An ansatz for the rules of evolution that is broad enough to describe the process-dependence of plasticity also in the presence of the vertex effect, but obeys the restrictions of the principles of material theory is

$$\begin{aligned}\mathbf{P}^{-1}\dot{\mathbf{P}}(t) &= \hat{\mathbf{\Pi}}(\mathbf{C}, \mathbf{P}, z, \dot{\mathbf{C}}) \\ \dot{z}(t) &= \hat{z}(\mathbf{C}, \mathbf{P}, z, \dot{\mathbf{C}}).\end{aligned} \tag{4.37}$$

Purely elastic behaviour with $(\mathbf{P}, z) = \text{const}$ is found on processes that are completely inside the elastic domain, i.e. a subset of the Mandel stress space which depends on g,

$$\mathcal{E} = \left\{\tilde{\mathbf{C}}\tilde{\mathbf{S}} |\ \phi(\tilde{\mathbf{C}}\tilde{\mathbf{S}}, g) \leq 0\right\} \tag{4.38}$$

The boundary $\partial\mathcal{E}$ is called *yield limit*, and the function $\phi(\tilde{\mathbf{C}}\tilde{\mathbf{S}}, g)$ *yield criterion*.

In contrast, processes that would penetrate the current yield limit are inelastic.

Here, we restrict ourselves to the case of convex elastic domains. This restriction allows for the use of certain results of convex optimization and has sufficient generality for most practical applications. However, the convexity can be released as stated, e.g. in Bertram (2005, p. 252).

The plastic flow changes the elastic law (4.32) by alteration of $\mathbf{P}$, and the elastic domain (4.38) indirectly through g. No inelastic process can leave the elastic domain configured by the actual plastic state. Accordingly some processes require a change of the plastic state variables and, thus, of the elastic law.

Contrary, rate-dependend models require that in the thermodynamic equilibrium no inelastic processes take place. Thus a finite overstress is needed. Other models use creep laws, like the widely used model for single crystals described in Kocks (1998a), which was originally introduced by Hutchinson (1976). Here, the yield limit is incorporated as the point where the mechanisms' activity increases massively, while the elastic domain in a strict sense shrinks to a single stress point. Rate-dependend models typically have a rate-independend limit.

4.2.4 Small elastic deformations

Small elastic deformations are characterized by $\|\tilde{\mathbf{F}} - \mathbf{1}\| \ll 1$.

All simplifications that apply for small total deformations are also available here. In particular, the elastic Green's strain can be linearized, and the elastic second Piola-Kirchhoff stress is approximately equal to the Cauchy stress tensor. Moreover, $\tilde{\mathbf{C}}\tilde{\mathbf{S}} \approx \tilde{\mathbf{S}}$ and, thus, the Mandel stress is approximately symmetric.

4.3 Constitutive theory of multi-mode plasticity

Section Overview
The theory of plasticity for materials with multiple coexisting mechanisms is worked out. This includes as a special case the classical (single mode) plasticity. Results of this Section are necessary for description of the vertex effect. In addition, the basic formula for further derivations are provided.

4.3.1 Multiple mechanisms of plasticity

The general constitutive equation for the flow and hardening rules (4.37) is

$$\begin{aligned} \mathbf{P}^{-1}\dot{\mathbf{P}} &= \hat{\mathbf{\Pi}}, \\ \dot{z} &= \hat{z}. \end{aligned} \tag{4.39}$$

If a set of N independent mechanisms potentially contribute to plastic flow, an additive relation is usually assumed for the rates (Koiter, 1953),

$$\begin{aligned} \hat{\mathbf{\Pi}} &= \sum_{\alpha=1}^{N} \hat{\mathbf{\Pi}}_\alpha, \\ \hat{z} &= \sum_{\alpha=1}^{N} \hat{z}_\alpha \end{aligned} \tag{4.40}$$

For each mechanism, a convex yield criterion

$$\phi_\alpha(\tilde{\mathbf{C}}\tilde{\mathbf{S}}, g) \leq 0 \tag{4.41}$$

is used. (4.41) are weak inequality constraints for (4.40). The elastic domain is defined by the intersection,

$$\mathcal{E} := \left\{ \tilde{\mathbf{C}}\tilde{\mathbf{S}} | \phi_\alpha(\tilde{\mathbf{C}}\tilde{\mathbf{S}}, g) \leq 0, \alpha = 1 \dots N \right\}. \tag{4.42}$$

The intersection of convex domains is alsoconvex (see Boyd and Vandenberghe (2004)).

The flow and hardening rules can be introduced according to the maximum dissipation principle (Bishop and Hill, 1951a,b), which is widely used in the literature (Chin and Mammel (1969), Lubliner (1990, Section 3.2.2), Neff (2000), Nguyen (2000), Miehe et al. (2002)). It is an equivalent variational formulation of the consistency condition and the normality rule. Thus it is a geometric and not a thermodynamic principle as the name seems to indicate.

$$\max_{\tilde{\mathbf{C}}\tilde{\mathbf{S}}, g} \left(-\tilde{\mathbf{C}}\tilde{\mathbf{S}} \cdot \mathbf{P}^{-1}\dot{\mathbf{P}} + g \cdot \dot{z} \right). \tag{4.43}$$

The elastic domain imposes constraints on the above maximization,

$$\phi_\alpha \leq 0 \qquad \alpha = 1 \dots N. \tag{4.44}$$

Introducing the plastic Lagrange multipliers $\lambda_\alpha \geq 0$, we obtain the unconstrained maximum principle

$$\max_{\tilde{\mathbf{C}}\tilde{\mathbf{S}}, g, \lambda_\alpha} \left(-\tilde{\mathbf{C}}\tilde{\mathbf{S}} \cdot \mathbf{P}^{-1}\dot{\mathbf{P}} + g \cdot \dot{z} + \sum_\alpha \lambda_\alpha \phi_\alpha \right). \tag{4.45}$$

By the methods of convex optimization (see Boyd and Vandenberghe, 2004) the solutions

$$\begin{aligned} \mathbf{P}^{-1}\dot{\mathbf{P}} &= -\sum_{\alpha=1}^{N} \lambda_\alpha \partial_{\tilde{\mathbf{C}}\tilde{\mathbf{S}}} \phi_\alpha, \\ \dot{z} &= -\sum_{\alpha=1}^{N} \lambda_\alpha \partial_g \phi_\alpha, \\ \lambda_\alpha \, \phi_\alpha &= 0 \quad \text{if } \alpha = 1 \dots N, \\ \lambda_\alpha &\geq 0 \quad \text{if } \alpha = 1 \dots N, \\ \phi_\alpha &\leq 0 \quad \text{if } \alpha = 1 \dots N \end{aligned} \tag{4.46}$$

are restricted by the Kuhn-Tucker conditions. (4.46) is a differential-algebraic system of equations (DAE) for the flow and hardening rule. (4.46) is equally valid for elastic and elastic-plastic processes, by $(4.46)_3$ selecting zero slip on a particular slip system α, if the according yield criterion $(4.46)_4$ is not fulfilled.

The normality rule $(4.46)_1$ is widely acknowledged as a physically well founded assumption in newer textbooks (Nguyen, 2000, Lubarda, 2002) Note that the minus sign in the flow rule (4.46) results from the definition of $\mathbf{P} = \mathbf{F}_p^{-1}$.

The set of active constraints, here interpreted as the set of inelastic mechanisms, is called the *active set*

$$\mathcal{A} = \{\alpha |\, \phi_\alpha = 0,\, \lambda_\alpha > 0\}\,. \tag{4.47}$$

In numerical solution procedures, the determination of $\mathcal{A}$ imposes some difficulties as the DAE problem can be ill posed due to a nonuniquess of the solution of the algebraic part (see Section 4.3.3). The positivity condition for the plastic multiplicators λ_α was introduced as a consequence of the one-sidedness of the constraints $(4.46)_5$. It is further analyzed in Section 4.3.4.

4.3.2 Solution of the DAE

More information about the plastic behaviour can be achieved by resolving the algebraic constraint equations in $(4.46)_3$ by differentiation, as it must be valid at any time. Thus the algebraic constraint equations can be replaced by a differential equation. Initial conditions must be consistent with the constraint.

Starting at a certain time, it is known which mechanisms are critical, i.e. $\alpha \in \mathcal{A} \;\Rightarrow\; \phi_\alpha = 0$. The remaining mechanisms have $\lambda_\alpha = 0$. Accordingly, forward differentiation is possible. Now, the differentiated constraint is

$$\lambda_\alpha\, \dot{\phi}_\alpha + \dot{\lambda}_\alpha \phi_\alpha = 0. \tag{4.48}$$

For active mechanisms, the first term applies, and for subcritical ones the second term. Accordingly, $\lambda_\alpha = 0$ for subcritical mechanisms. When a previously inactive mechanism gets critical, new consistent initial conditions $\phi = 0$ have to be formulated.

Thus from the differentiated constraint (4.48)

$$\max_{\tilde{\mathbf{C}}\tilde{\mathbf{S}},g,\lambda_\alpha} \left(-\tilde{\mathbf{C}}\tilde{\mathbf{S}} \cdot \mathbf{P}^{-1}\dot{\mathbf{P}} + g \cdot \dot{z} + \sum_{\alpha,\phi_\alpha=0} \lambda_\alpha \dot{\phi}_\alpha \right). \tag{4.49}$$

a similar set of equations arises

$$\begin{aligned}
\mathbf{P}^{-1}\dot{\mathbf{P}} &= -\sum_{\alpha=1}^{N} \lambda_\alpha \partial_{\tilde{\mathbf{C}}\tilde{\mathbf{S}}}\phi_\alpha, \\
\dot{z} &= -\sum_{\alpha=1}^{N} \lambda_\alpha \partial_g \phi_\alpha, \\
\lambda_\alpha\, \dot{\phi}_\alpha &= 0 \quad \text{if } \phi_\alpha = 0, \\
\lambda_\alpha &\geq 0 \quad \text{if } \phi_\alpha = 0, \\
\dot{\phi}_\alpha &\leq 0 \quad \text{if } \phi_\alpha = 0, \\
\lambda_\alpha &= 0 \quad \text{if } \phi_\alpha < 0
\end{aligned} \tag{4.50}$$

We will now explicitly determine the plastic multipliers λ_α, $\alpha \in \mathcal{A}$ by the consistency condition,

$$\dot{\phi}_\alpha = \partial_{\tilde{\mathbf{C}}\tilde{\mathbf{S}}}\phi_\alpha \cdot \frac{\mathrm{d}}{\mathrm{d}t}\tilde{\mathbf{C}}\tilde{\mathbf{S}} + \partial_g \phi_\alpha \cdot \dot{g}. \tag{4.51}$$

For further evaluation, we insert

$$\begin{aligned}
\frac{\mathrm{d}}{\mathrm{d}t}\tilde{\mathbf{C}}\tilde{\mathbf{S}} &= \dot{\tilde{\mathbf{C}}}\tilde{\mathbf{S}} + \tilde{\mathbf{C}}\dot{\tilde{\mathbf{S}}} \\
&= \left[\mathbf{P}^\top \dot{\mathbf{C}}\mathbf{P} + 2\mathrm{sym}\tilde{\mathbf{C}}\mathbf{P}^{-1}\dot{\mathbf{P}}\right]\tilde{\mathbf{S}} + \frac{1}{2}\tilde{\mathbf{C}}\tilde{\mathbb{C}}[\mathbf{P}^\top \dot{\mathbf{C}}\mathbf{P} + 2\mathrm{sym}\tilde{\mathbf{C}}\mathbf{P}^{-1}\dot{\mathbf{P}}] \\
\dot{g} &= \frac{\partial \hat{g}}{\partial z}\dot{z}
\end{aligned} \tag{4.52}$$

and rearrange to get an explicit expression in the rates $\mathbf{P}^{-1}\dot{\mathbf{P}}$, $\dot{\mathbf{C}}$, and $\dot{z}$,

$$\dot{\phi}_\alpha = \tilde{\mathbf{A}}_\alpha \cdot \left(\mathrm{sym}\tilde{\mathbf{C}}\mathbf{P}^{-1}\dot{\mathbf{P}} + \mathbf{P}^\top \frac{1}{2}\dot{\mathbf{C}}\mathbf{P}\right) + a_\alpha \cdot \dot{z}. \tag{4.53}$$

Here, the factors

$$\begin{aligned}
\tilde{\mathbf{A}}_\alpha &= 2\mathrm{sym}(\partial_{\tilde{\mathbf{C}}\tilde{\mathbf{S}}}\phi_\alpha \tilde{\mathbf{S}}) + \tilde{\mathbb{C}}[\tilde{\mathbf{C}}\partial_{\tilde{\mathbf{C}}\tilde{\mathbf{S}}}\phi_\alpha] \\
a_\alpha &= \partial_g \phi_\alpha \frac{\partial g}{\partial z}
\end{aligned} \tag{4.54}$$

have been introduced. After insertion of the flow and hardening rule $(4.50)_{1,2}$, the consistency matrix

$$g_{\alpha\beta} = \frac{\partial \dot{\phi}_\alpha}{\partial \lambda_\beta} = \tilde{\mathbf{A}}_\alpha \cdot \tilde{\mathbf{C}}\, \partial_{\tilde{\mathbf{C}}\tilde{\mathbf{S}}}\phi_\beta + a_\alpha \partial_g \phi_\beta \tag{4.55}$$

simplifies the resulting equation,

$$\dot{\phi}_\alpha = -\sum_{\beta \in \mathcal{A}} g_{\alpha\beta}\lambda_\beta + \mathbf{P} \star \tilde{\mathbf{A}}_\alpha \cdot \dot{\mathbf{E}} = 0, \quad \alpha \in \mathcal{A} \tag{4.56}$$

Symbol	Lubarda (2002)	Nguyen (2000)	Petryk (2000b)
$\mathbf{P} \star \tilde{\mathbf{A}}_\alpha$	$\mathbf{C}_0^\alpha$	$\mathcal{B}_i$	$\boldsymbol{\lambda}_K$,$\boldsymbol{\lambda}_K^p$
$\operatorname{sym} \tilde{\mathbf{C}} \partial_{\tilde{\mathbf{C}}\tilde{\mathbf{S}}} \phi_\alpha$	$\mathbf{P}_0^\alpha$	$f^i{}_{,A}$	$\div$
$g_{\alpha\beta}$	$g_{\alpha\beta}$	$-\mathcal{C}_{ij}$	g_{KL}
$a_\alpha \partial_g \phi_\beta$	$h_{\alpha\beta}$	$\mathcal{H}_{ij}$	$\div$
$\mathbf{P} \star \tilde{\mathbb{C}}$	$\boldsymbol{\Lambda}_{(1)}$	$\mathcal{W}_{,\nabla u \, \nabla u}$	L^e

Tab. 4.1: Notation of multi-mode plasticity found in the literature

which can be finally solved for the plastic multipliers.

A derivation for a number of stress and strain measures can be found in Lubarda (2002), Section 12, while a formulation for dissipative standard materials is briefly outlined in Nguyen (2000), Section 15.5.2. A generalized approach is used by Petryk (2000b), where the rate equations are assumed as the fundamental constitutive equations, and the above formula can be derived by the introduction of an elastic range and the normality rule. For comparison, notations found in the cited literature are summarized in Table 4.1. Note that different stress and strain measures are used. The interaction matrix $g_{\alpha\beta}$, however, is invariant with respect to the choice of stress and strain measure (Petryk, 2000b, Lubarda, 2002).

The plastic multipliers can be obtained by solving (4.56),

$$\lambda_\beta = \begin{cases} \sum_{\alpha \in \mathcal{A}} (g^{-1})_{\beta\alpha} \mathbf{P} \star \tilde{\mathbf{A}}_\alpha \cdot \dot{\mathbf{E}} & \beta \in \mathcal{A} \\ 0 & \beta \notin \mathcal{A} \end{cases} . \tag{4.57}$$

Insertion in the flow rule $(4.50)_1$ yields

$$\begin{aligned} \mathbf{P}^{-1}\dot{\mathbf{P}} &= - \sum_{\alpha,\beta \in \mathcal{A}} (g^{-1})_{\beta\alpha} \left(\partial_{\tilde{\mathbf{C}}\tilde{\mathbf{S}}} \phi_\beta\right) \otimes \mathbf{P} \star \tilde{\mathbf{A}}_\alpha[\dot{\mathbf{E}}] \\ &= - \sum_{\alpha,\beta \in \mathcal{A}} (g^{-1})_{\beta\alpha} \left(\partial_{\tilde{\mathbf{C}}\tilde{\mathbf{S}}} \phi_\beta\right) \otimes \tilde{\mathbf{F}} \star \tilde{\mathbf{A}}_\alpha[\mathbf{D}], \end{aligned} \tag{4.58}$$

whereas the hardening rule $(4.50)_2$ results in

$$\begin{aligned} \dot{z} &= - \sum_{\alpha,\beta \in \mathcal{A}} (g^{-1})_{\beta\alpha} \left(\partial_g \phi_\beta\right) \otimes \mathbf{P} \star \tilde{\mathbf{A}}_\alpha[\dot{\mathbf{E}}] \\ &= - \sum_{\alpha,\beta \in \mathcal{A}} (g^{-1})_{\beta\alpha} \left(\partial_g \phi_\beta\right) \otimes \tilde{\mathbf{F}} \star \tilde{\mathbf{A}}_\alpha[\mathbf{D}]. \end{aligned} \tag{4.59}$$

Note the special convention for the variables z and g of unspecified rank.

In both equations, the strain rate is mapped by a state-dependent linear operator on the according rates. Thus, the theory is *rate-independent* (see Section 4.3.6).

The exploitation of $(4.50)_3$ showed that there are still algebraic equations contained after single differentiation, since $(4.50)_3$ contained the unknown plastic multipliers λ as hidden constraints (Scherf, 2000). One finds that (4.46) is

a DAE of index 2 by another differentiation of (4.56) that results finally in an (implicit) ODE for λ.

4.3.3 Properties of the multiple condition of consistency

The Taylor problem

(4.56) can be interpreted as a mapping from the plastic multipliers to the strain rate $\dot{\mathbf{E}}$. Moreover, the volume preserving nature of plasticity imposes an additional constraint, thus it is a mapping $\mathbb{R}^{\dim(\mathcal{A})} \to \mathbb{R}^5$, which cannot be inverted for $\dim(\mathcal{A}) \geq 5$. This number imposes the *Taylor problem* of the selection of the active set.

In the case of crystal plasticity, a number of proposals have been made to overcome it by selection of five slip systems. A largely applied approach is the center of gravity method: For $d = \dim \mathcal{A} > 5$ any combinatoric choice of 5 of d mechanisms is investigated. A superposition is computed afterwards. Other methods, including a random choice have been proposed. They have been summarized by van Houtte (1988) and Kocks (1998a).

A physical aproach has been proposed by exploitation of the energy criterion of plastic stability (Petryk, 1999).

Standard mathematical approaches like the Moore-Penrose generalized inverse have been investigaded and used (Anand and Kothari, 1996, Miehe et al., 1999, Knockaert et al., 2000) that use minimization of the defect to select one of the multiple solutions. This approach has been interpreted in Knockaert et al. (2000) as physically adequate by application of Taylor's minimum slip principle (Taylor, 1938). Other techniques in the style of a Tykhonov regularization or a problem-adapted "Ansatz in reduced space" have been introduced by Miehe et al. (1999) (see also Miehe and Schröder, 2001). Another problem oriented solution is a special iterative procedure based on a combination of a Lagrange formalism and a penalty method proposed by Schmidt-Baldassari (2003) which has been shown to converge towards $\lambda_\alpha = 0$ for $\alpha \notin \mathcal{A}$.

For a single yield surface the Taylor problem is inexistent. This can be exploited by a regularization of the yield limit of crystal plasticity. It has been proposed independently by Arminjon (1991) and Gambin (1991) and further investigated by Schurig and Bertram (2003), see Section 4.4.

Symmetry and condition of the consistency matrix

In the resolved DAE, the consistency matrix $g_{\alpha\beta}$ is of central importance. A matrix with similar properties arises equally in the numerical solution of (4.46) (Knockaert et al., 2000, Miehe et al., 1999). In general, it is nonsymmetric. However, symmetry is achieved in a number of cases of different significance.

For small elastic deformations ($\tilde{\mathbf{C}} \approx \mathbf{1}$) and symmetry of the interaction matrix $\partial_g \phi_\alpha \frac{\partial g}{\partial z} \partial_g \phi_\beta$, $\tilde{\mathbf{C}}\tilde{\mathbf{S}} \approx \tilde{\mathbf{S}}$, $\tilde{\mathbf{A}}_\alpha = \tilde{\mathbb{C}}[\partial_{\tilde{\mathbf{C}}\tilde{\mathbf{S}}} \phi_\alpha]$, and $g_{\alpha\beta} = \tilde{\mathbb{C}}[\partial_{\tilde{\mathbf{C}}\tilde{\mathbf{S}}} \phi_\alpha] \cdot \partial_{\tilde{\mathbf{C}}\tilde{\mathbf{S}}} \phi_\beta + \frac{\partial g}{\partial z} \partial_g \phi_\alpha \partial_g \phi_\beta$ (Steinmann, 1996, Knockaert et al., 2000). Also, special choices for the interaction matrix can be made to symmetrize $g_{\alpha\beta}$, as proposed by

Havner and Shalaby (1978). If a potential exists for the hardening variables, by an integrability condition the symmetry of the interaction matrix follows (Nguyen, 2000, p.265f). Sometimes this it at least an approximation (Miehe et al., 2002). Convexity of the potential ensures positive definiteness and, thus, invertibility.

$g_{\alpha\beta}$ can have a bad condition number or even be irregular. The reason is strongly connected with the Taylor problem. In the five-dimensional $\tilde{\mathbf{C}}\tilde{\mathbf{S}}$-space only five of the normal directions $\partial_{\tilde{\mathbf{C}}\tilde{\mathbf{S}}}\phi_\beta$ can be linearly independent. Thus, the maximum rank of $\tilde{\mathbf{A}}_\alpha \cdot \tilde{\mathbf{C}}\,\partial_{\tilde{\mathbf{C}}\tilde{\mathbf{S}}}\phi_\beta$ is 5. Irregularity follows for more than five active mechanisms in the case of perfect plasticity. Hardening sometimes improves the situation by the shift of singular values through the interaction matrix. However, if hardening moduli are small, ill-conditioned problems can still arise. This case needs the same way of treatment as above.

4.3.4 The loading condition

Besides the condition $\phi_\alpha = 0$, also $\lambda_\alpha \geq 0$ was required for active mechanisms. This second criterion was a mere mathematical requirement from the maximization principle (4.45).

Any negative or vanishing plastic multiplier λ_α means that the according rate of the constraint ϕ_α is also negative or zero. Thus, the positivity condition excludes unloading mechanisms. A positive value of λ_α is required for loading mechanisms only.

The loading condition used by Bertram (2005) for single mode plasticity

$$\dot{\phi}|_{\mathbf{P},z=const} > 0 \tag{4.60}$$

is still valid. However, it cannot be simply transferred equally to each single mechanism's constraint. The reason is that for nondiagonal $g_{\alpha\beta}$ the mechanisms interact plastically by latent hardening (Hill, 1967). The generalization is

$$\exists\alpha : \dot{\phi}_\alpha|_{\mathbf{P},z=const} > 0. \tag{4.61}$$

Thus, it is possible to determine in advance whether there are active mechanisms at all, but not the active set a priori without solving the incremental equations.

Inserting

$$\dot{\phi}_\alpha|_{\mathbf{P},z=const} = \mathbf{P} \star \tilde{\mathbf{A}}_\alpha \cdot \dot{\mathbf{E}} \tag{4.62}$$

in the positivity condition for the plastic multipliers as obtained in (4.57),

$$\sum_{\alpha\in\mathcal{A}} (g^{-1})_{\beta\alpha}\dot{\phi}_\alpha|_{\mathbf{P},z=\text{const}} = \tilde{\mathbf{N}}_\beta \cdot \frac{\mathrm{d}}{\mathrm{d}t}\tilde{\mathbf{C}}\tilde{\mathbf{S}}\Big|_{\mathbf{P},z=\text{const}} > 0 \qquad \beta \in \mathcal{A}, \tag{4.63}$$

which can be interpreted as a coupled loading condition. The generalized normal

$$\tilde{\mathbf{N}}_\beta = \sum_{\alpha\in\mathcal{A}} (g^{-1})_{\beta\alpha}\partial_{\tilde{\mathbf{C}}\tilde{\mathbf{S}}}\phi_\alpha \tag{4.64}$$

replaces the normal direction in uncoupled mechanisms. Accordingly, for a diagonal $g_{\alpha\beta}$, $\tilde{\mathbf{N}}_\beta = \partial_{\tilde{\mathbf{C}}\tilde{\mathbf{S}}}\phi_\beta$ (Lubarda, 2002, Section 12.13).

An exploitation is possible, whenever the active set $\mathcal{A}$ is known. Usually this is not the case. Using a hypothesis on the active set, the plastic multipliers can be determined and the validity of the hypotheses be checked by the positivity constraint. Thus, an iterative solution process is necessary.

4.3.5 Derivation of rate equations

The forward material time rate of (4.31) yields $\dot{\tilde{\mathbf{S}}} = \tilde{\mathbb{C}}[\dot{\tilde{\mathbf{E}}}]$, with $\dot{\tilde{\mathbf{E}}} = \frac{1}{2}\dot{\tilde{\mathbf{C}}}$ the rate of the elastic Green's strain tensor. Insertion of the respective elastic tensors yields

$$\begin{aligned}\dot{\mathbf{S}} = \mathbf{P} \star \tilde{\mathbb{C}}[\dot{\mathbf{E}}] \\ + \mathbf{P}\left(2\mathrm{sym}\mathbf{P}^{-1}\dot{\mathbf{P}}\tilde{\mathbf{S}} + \tilde{\mathbb{C}}[\tilde{\mathbf{C}}\mathbf{P}^{-1}\dot{\mathbf{P}}]\right)\mathbf{P}^\top\end{aligned} \tag{4.65}$$

resulting in a split of the second Piola-Kirchhoff stress rate into elastic and plastic parts $(4.65)_1$ and $(4.65)_2$. Upon insertion of (4.58), the rate of stress turns into an incremental law, (see Lubarda, 2002, Sections 9.5f, Bertram, 2005, p. 270),

$$\dot{\mathbf{S}} = \mathbf{P} \star \tilde{\mathbb{K}}[\dot{\mathbf{E}}]. \tag{4.66}$$

The incremental moduli tensor is given by

$$\tilde{\mathbb{K}} = \tilde{\mathbb{C}} - \sum_{\alpha,\beta\in\mathcal{A}} (g)^{-1}_{\alpha\beta}\tilde{\mathbf{A}}_\alpha \otimes \tilde{\mathbf{A}}_\beta. \tag{4.67}$$

A rate potential $\mathcal{U}$ exists, if $\mathbb{K} = \mathbf{P} \star \tilde{\mathbb{K}}$ has the major symmetry. This is the case, if $\tilde{\mathbb{C}}$ has this property (in the case of hyperelasticity $\tilde{c}_{ijkl} = \tilde{c}_{klij}$), and moreover $g_{\alpha\beta} = g_{\beta\alpha}$ (see Section 4.3.3).

Then, the rate law and its potential are connected by

$$\begin{aligned}\mathcal{U} &= \frac{1}{2}\dot{\mathbf{E}} \cdot \mathbb{K}[\dot{\mathbf{E}}], \\ \dot{\mathbf{S}} &= \partial_{\dot{\mathbf{E}}}\mathcal{U}, \\ \mathbb{K} &= \frac{\partial^2\mathcal{U}}{\partial\dot{\mathbf{E}}\,\partial\dot{\mathbf{E}}}.\end{aligned} \tag{4.68}$$

For other measures, we obtain according to (4.20)

$$\begin{aligned}\dot{\mathbf{T}}_0 - \mathbf{L}\mathbf{T}_0 &= \partial_{\dot{\mathbf{F}}}\,\frac{1}{2}\dot{\mathbf{F}} \cdot (\mathbf{F} \otimes \mathbf{1}) \star \mathbb{K}[\dot{\mathbf{F}}] \\ \dot{\boldsymbol{\tau}} - \mathbf{L}\boldsymbol{\tau} - \boldsymbol{\tau}\mathbf{L}^\top &= \partial_{\mathbf{D}}\,\frac{1}{2}\mathbf{D} \cdot \mathbf{F} \star \mathbb{K}[\mathbf{D}] \\ \dot{\mathbf{S}}^x - (\mathbf{A}^{-1}\mathbf{F})^\bullet(\mathbf{A}^{-1}\mathbf{F})^{-1}\mathbf{S}^x - \mathbf{S}^x\left((\mathbf{B}^{-1}\mathbf{F})^\bullet(\mathbf{B}^{-1}\mathbf{F})^{-1}\right)^\top & \\ = \partial_{\dot{\mathbf{E}}^x}\,\frac{1}{2}\dot{\mathbf{E}}^x \cdot (\mathbf{A}^{-1}\mathbf{F} \otimes \mathbf{B}^{-1}\mathbf{F}) \star \mathbb{K}[\dot{\mathbf{E}}^x].\end{aligned} \tag{4.69}$$

Inspection shows that in any case $\mathcal{U}$ is a homogeneous function of degree two of the associated rate of deformation. Its domain is divided into a number of disjoint cones, each defined by the active set $\mathcal{A}$ that can be determined from (4.50). By (4.68) the incremental moduli tensor $\mathbb{K}$ is the Hessian of $\mathcal{U}$ which is in turn piecewise defined.

Another split of strain rate is possible by reformulation of (4.66),

$$\begin{aligned}\dot{\mathbf{S}} &= \mathbf{P} \star \tilde{\mathbb{C}}[\dot{\mathbf{E}} - \dot{\mathbf{E}}_p] \\ \dot{\mathbf{E}}_p &= \left(\mathbf{P} \star \tilde{\mathbb{C}}\right)^{-1} \circ \left(\mathbf{P} \star \sum_{\alpha,\beta\in\mathcal{A}} (g)^{-1}_{\alpha\beta} \tilde{\mathbf{A}}_\alpha \otimes \tilde{\mathbf{A}}_\beta\right)[\dot{\mathbf{E}}] \\ &= \sum_{\alpha,\beta\in\mathcal{A}} (g)^{-1}_{\alpha\beta} \tilde{\mathbb{C}}^{-1}[\tilde{\mathbf{A}}_\alpha] \otimes \tilde{\mathbf{A}}_\beta[\mathbf{P}^\top \dot{\mathbf{E}} \mathbf{P}],\end{aligned} \tag{4.70}$$

introducing a formal analogy to small strain formulations (Lubarda and Benson, 2001).

4.3.6 Rate-independence

Replacing a strain process defined by $\mathbf{C}(t)$ by a slower or faster one $\mathbf{C}^*(t) = \mathbf{C}(a(t))$ (Bertram, 1989), one finds that $\dot{\mathbf{C}}^*(t) = \dot{\mathbf{C}}(a(t))\dot{a}(t)$. All the material functionals used so far prove to be positive homogeneous in the strain rate. Clearly, upon integration, (4.66) as well as (4.58) and (4.59) yield the same results after the strain process $\mathbf{C}^*(t)$ at time $a(t)$ compared with $\mathbf{C}(t)$ at t. Thus the presented theory is *rate-independent*.

In a general way, rate-independent plasticity models can be introduced with an extension of the set of variables included in the flow and hardening rule (Halphen and Nguyen, 1975, Bertram, 1999, 2005)

$$\hat{\mathbf{\Pi}} : \ (\tilde{\mathbf{C}}\tilde{\mathbf{S}}, g; \dot{\mathbf{C}}) \mapsto \mathbf{P}^{-1}\dot{\mathbf{P}}, \qquad \hat{z} : \ (\tilde{\mathbf{C}}\tilde{\mathbf{S}}, g; \dot{\mathbf{C}}) \mapsto \dot{z}. \tag{4.71}$$

and the additional assumption that the functions are positive homogeneous in $\dot{\mathbf{C}}$. As a consequence, a split in magnitude and direction is possible,

$$\begin{aligned}\hat{\mathbf{\Pi}} &= \sum_\alpha \lambda_\alpha(\tilde{\mathbf{C}}\tilde{\mathbf{S}}, g, \|\dot{\mathbf{C}}\|, \frac{\dot{\mathbf{C}}}{\|\dot{\mathbf{C}}\|})\, \tilde{\mathbf{\Pi}}_\alpha(\tilde{\mathbf{C}}\tilde{\mathbf{S}}, g, \frac{\dot{\mathbf{C}}}{\|\dot{\mathbf{C}}\|}) \\ \hat{z} &= \sum_\alpha \lambda_\alpha(\tilde{\mathbf{C}}\tilde{\mathbf{S}}, g, \|\dot{\mathbf{C}}\|, \frac{\dot{\mathbf{C}}}{\|\dot{\mathbf{C}}\|})\, \tilde{z}_\alpha(\tilde{\mathbf{C}}\tilde{\mathbf{S}}, g, \frac{\dot{\mathbf{C}}}{\|\dot{\mathbf{C}}\|})\end{aligned} \tag{4.72}$$

where $\lambda(\tilde{\mathbf{C}}\tilde{\mathbf{S}}, g, \bullet, \frac{\dot{\mathbf{C}}}{\|\dot{\mathbf{C}}\|})$ is a positive homogeneous function.

(4.58) and (4.59) fit into this format. The difference is that in Section 4.3.1 (p. 39) λ_α are mathematical objects that are used to implement consistency. Instead of a direct constitutive assumption, they are obtained from the algebraic constraint equations.

Here, the plastic multipliers λ_α are considered as constitutive functions of their own right, allowing for a broader class of materials. The list of variables

shows that the rate $\dot{\mathbf{C}}$ is not considered as one of the normal constitutive variables. In fact it differs by the condition of rate independence. To obtain the same result as in 4.3.2, the differentiated condition of consistency is utilized, together with the loading condition of (4.63)

$$\begin{aligned}
\mathbf{P}^{-1}\dot{\mathbf{P}} &= -\sum_{\alpha=1}^{N} \lambda_\alpha \partial_{\tilde{\mathbf{C}}\tilde{\mathbf{S}}}\phi_\alpha, \\
\dot{z} &= \sum_{\alpha=1}^{N} \lambda_\alpha \partial_g \phi_\alpha, \\
\lambda_\alpha\, \dot{\phi}_\alpha &= 0 \quad \text{if } \phi_\alpha = 0, \\
\dot{\phi}_\alpha|_{\mathbf{P},z=\text{const}} &\geq 0 \quad \text{if } \phi_\alpha = 0, \\
\dot{\phi}_\alpha &\leq 0 \quad \text{if } \phi_\alpha = 0, \\
\lambda_\alpha &= 0 \quad \text{if } \phi_\alpha < 0
\end{aligned} \tag{4.73}$$

As shown in Chapter 5, an extension of this scheme can be used to introduce additional effects that are seen in multi-surface plasticity into theories with a single (but process-dependend) plastic potential.

Even more general are constitutive assumptions that are based on rate equations of the type (4.66). As indicated in Petryk (2000a), a number of physically distinct phenomena can be covered by such equations. Additional attractivity comes out of the formal similarity to elastic laws that allows for some methods of solution from the theory of elasticity to be transferred.

4.4 Regular yield criteria

Section Overview
Two approaches to define a single smooth yield function that approximates the non-smooth elastic domain of multi-mode plasticity are presented. For both cases, the associated flow rules are computed. In contradiction to the multi-mode theory, the vertex effect is not present in these models.

4.4.1 The model of interacting slip systems

To overcome the Taylor problem in single crystal plasticity, the model of interacting slip systems was proposed independently by Gambin (1991) and Arminjon (1991).

They introduced a single yield surface based on an L_p-regularization of the compound crystallite yield locus and an associated flow rule. The approach is similar to the rate-dependent theory (Kocks, 1998b) and includes an exponent similar to the reciprocal strain rate sensitivity as a parameter.

Gambin and Barlat (1997) connected this exponent with the stacking fault energy of the material. Kowalczyk (2001), Kowalczyk and Gambin (2004) used this approach for the determination of an evolving macroscopic yield surface

of a polycrystal, based on the grain interaction model by Sachs (1928) and rigid-plastic grains.

Schurig and Bertram (2003) discussed an ansatz on the slip system level that does not integrate to a normality rule for the crystallite. The ratios of the slip rates are the same as in the rate-dependend theory. For Taylor hardening (all critical stresses are equal, $g_\alpha = g$), the approaches are identical.

A general discussion of the L_p-regularization of compound yield surfaces (for sheet metals) can be found in Mollica and Srinivasa (2002).

Starting from the Schmid law for the slip systems of a single crystal,

$$\begin{aligned} \phi_\alpha(\tilde{\mathbf{C}}\tilde{\mathbf{S}}, g_\alpha) &= \tau_\alpha - \tau_\alpha^c = 0 \\ \tau_\alpha &= \tilde{\mathbf{C}}\tilde{\mathbf{S}} \cdot \mathbf{M}_\alpha \\ \tau_\alpha^c &= g_\alpha, \end{aligned} \tag{4.74}$$

introducing the constant structural Schmid tensors $\tilde{\mathbf{M}}_\alpha = \mathbf{d}_\alpha \otimes \mathbf{n}^\alpha$, where $\mathbf{d}_\alpha$ is the tangential vector of a slip system's slip direction and the $\mathbf{n}^\alpha$ the covector of the according slip plane, an equivalent formulation is found,

$$\phi_\alpha^G(\tilde{\mathbf{C}}\tilde{\mathbf{S}}, g_\alpha) = \frac{\phi_\alpha(\tilde{\mathbf{C}}\tilde{\mathbf{S}}, g_\alpha)}{g_\alpha} = \left(\frac{\tau_\alpha}{g_\alpha}\right) - 1. \tag{4.75}$$

To obtain a useful expression without absolute values, the set of available slip systems has to be chosen in such a manner that positive and negative slip direction are recognized as two distinct slip systems. Thus the number of slip systems in a mathematical sense is twice the number of physically distinct slip systems.

Let $\mathcal{B} \supseteq \mathcal{A}$ be an arbitrary set of slip mechanisms. An L_p-regularization of the individual mechanisms $\alpha \in \mathcal{B}$ is obtained by

$$\Phi(\tilde{\mathbf{C}}\tilde{\mathbf{S}}, g_\alpha) = \frac{1}{n+1} \sum_{\alpha \in \mathcal{B}} \left(\phi_\alpha^G + 1\right)^{n+1} - 1. \tag{4.76}$$

For growing exponents n, this function approaches the multi-mode yield limit (Fig. 4.1) and represents a rounded crystallite yield locus. Application of (4.46) for this single yield surface results in

$$\begin{aligned} \mathbf{P}^{-1}\dot{\mathbf{P}} &= -\lambda \sum_{\alpha \in \mathcal{B}} \frac{1}{g_\alpha} \left(\phi_\alpha^G + 1\right)^n \partial_{\tilde{\mathbf{C}}\tilde{\mathbf{S}}} \phi_\alpha, \\ \dot{z}_\beta &= -\lambda \sum_{\alpha \in \mathcal{B}} \frac{1}{g_\alpha} \left(\phi_\alpha^G + 1\right)^n \left(\partial_{g_\beta} \phi_\alpha - \phi_\alpha^G\right), \\ \lambda\Phi &= 0, \\ \lambda &\geq 0, \\ \phi &\leq 0 \end{aligned} \tag{4.77}$$

By comparison with the original approach, an interpretation as a modified multi-mode approach with interacting slip systems (Kowalczyk, 2001)

$$\lambda_\alpha = \lambda \frac{1}{g_\alpha} \left(\phi_\alpha^G + 1\right)^n = \lambda \theta_\alpha^G \tag{4.78}$$

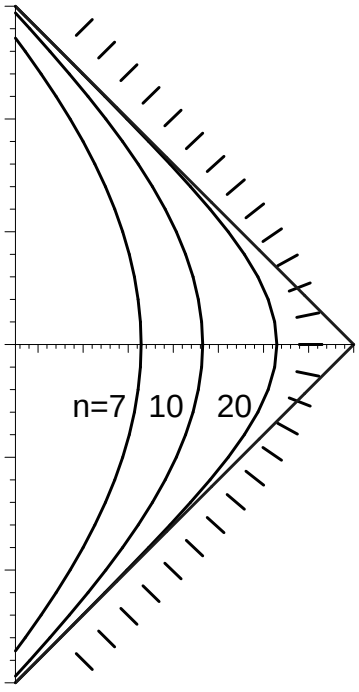

Fig. 4.1: Sketch of the rounded crystallite yield locus (Bertram, 2005)

can be found. $\theta_\alpha = \left(\frac{\tau_\alpha}{g_\alpha}\right)^n$ regularizes the Schmid criterion, and $\theta^G_\alpha = \frac{1}{g_\alpha}\theta_\alpha$.

If $\alpha \in \mathcal{A} \Rightarrow \phi^G_\alpha = \phi_\alpha = 0 \Rightarrow \theta_\alpha = 1$. In the limit,

$$\lim_{n\to\infty} \theta_\alpha = \begin{cases} 1 & \alpha \in \mathcal{A} \\ 0 & \alpha \notin \mathcal{A} \end{cases} \tag{4.79}$$

Thus, the approach can be interpreted as a regularization of the Heaviside function which implements a sudden activation. Accordingly, (4.78) is still approximately fulfilled if subcritical slip systems are included.

The plastic multiplier λ can be obtained again by differentiation of the algebraic constraint, inserting (4.56) and (4.78),

$$\begin{aligned}
\dot\Phi &= \sum_{\alpha\in\mathcal{B}} \frac{1}{g_\alpha} \left(\phi^G_\alpha + 1\right)^n \left(\dot\phi_\alpha - \phi^G_\alpha \dot g_\alpha\right) \\
&= \sum_{\alpha\in\mathcal{B}} \theta^G_\alpha \left(\mathbf{P} \star \tilde{\mathbf{A}}_\alpha \cdot \dot{\mathbf{E}} - \sum_{\beta\in\mathcal{B}} g_{\alpha\beta}\lambda_\beta + \phi^G_\alpha \frac{\partial\, g_\alpha}{\partial\, z_\beta} \partial_{g_\beta}\phi_\beta\, \lambda_\beta \right) \\
&= \sum_{\alpha\in\mathcal{B}} \theta^G_\alpha \mathbf{P} \star \tilde{\mathbf{A}}_\alpha \cdot \dot{\mathbf{E}} \\
&\quad + \lambda \sum_{\alpha,\beta\in\mathcal{B}} \theta^G_\alpha \theta^G_\beta g^G_{\alpha\beta} \\
g^G_{\alpha\beta} &= \frac{\partial \dot\phi^G_\alpha}{\partial \lambda_\beta} \\
&= g_{\alpha\beta} - \phi^G_\alpha \frac{\partial\, g_\alpha}{\partial\, z_\beta} \partial_{g_\beta}\phi_\beta \\
&= g_{\alpha\beta} \qquad \text{if } \mathcal{B} \subseteq \mathcal{A}
\end{aligned} \tag{4.80}$$

resulting in

$$\lambda = \sum_{\alpha\in\mathcal{B}} \frac{\theta^G_\alpha}{\sum_{\gamma\,\delta\in\mathcal{B}} \theta^G_\gamma \theta^G_\delta g^G_{\gamma\delta}} \mathbf{P} \star \tilde{\mathbf{A}}_\alpha \cdot \dot{\mathbf{E}} \tag{4.81}$$

and

$$\begin{aligned}
\lambda_\beta &= \sum_{\alpha\in\mathcal{B}} \frac{\theta^G_\beta\, \theta^G_\alpha}{\sum_{\gamma,\delta\in\mathcal{B}} \theta^G_\gamma \theta^G_\delta g^G_{\gamma\delta}} \mathbf{P} \star \tilde{\mathbf{A}}_\alpha \cdot \dot{\mathbf{E}}, \\
&= \sum_{\alpha\in\mathcal{B}} g^{G\dagger}_{\beta\alpha} \mathbf{P} \star \tilde{\mathbf{A}}_\alpha \cdot \dot{\mathbf{E}}.
\end{aligned} \tag{4.82}$$

Our solution results in an "inverse" matrix

$$g^{G\dagger}_{\alpha\beta} = \frac{\theta^G_\alpha \theta^G_\beta}{\sum_{\gamma,\delta\in\mathcal{B}} \theta^G_\gamma\; g^G_{\gamma\delta} \theta^G_\delta} \tag{4.83}$$

Although it is not the inverse of g^G, it takes place in solving for the λ_α of the interacting slip system model. Clearly, $g^{G\dagger}_{\alpha\beta} = g^{G\dagger}_{\beta\alpha}$.

To investigate, wether $g^{G\dagger}$ is a pseudoinverse of g^G, we use the neccessary and sufficient condition $g^G\, g^{G\dagger}\, g^G = g^G$. Insertion of (4.83) this results in.

$$\frac{\sum_{\alpha,\beta\in\mathcal{B}} g^G_{\mu\alpha}\, \theta^G_\alpha \theta^G_\beta\, g^G_{\beta\nu}}{\sum_{\gamma,\delta\in\mathcal{B}} \theta^G_\gamma g^G_{\gamma\delta} \theta^G_\delta} = g^G_{\mu\nu} \qquad \mu,\nu\in\mathcal{B}. \tag{4.84}$$

For (4.84) to hold, g^G must be symmetric. Introducing the weighted row sum $r_\alpha = \sum_{\beta\in\mathcal{B}} g^G_{\alpha\beta}\theta^G_\beta$, (4.84) can be reformulated as

$$g^G_{\mu\nu} = \frac{r_\mu\, r_\nu}{\sum_{\gamma\in\mathcal{B}} \theta^G_\gamma\, r_\gamma} \qquad \mu,\nu\in\mathcal{B}. \tag{4.85}$$

The implications of (4.85) will be discussed in Section 4.4.3.

4.4.2 The viscoplastic flow potential

Rice (1970) introduced the following viscous flow potential,

$$\omega(\tilde{\mathbf{C}}\tilde{\mathbf{S}}, g) = \frac{1}{n+1}\dot\gamma_0 \sum_\alpha g_\alpha \left|\frac{\tau_\alpha}{g_\alpha}\right|^{n+1}. \tag{4.86}$$

Its derivatives

$$\frac{\partial\omega}{\partial\tau_\alpha} = \dot\gamma_0 \left|\frac{\tau_\alpha}{g_\alpha}\right|^n \mathrm{sign}\tau_\alpha. \tag{4.87}$$

are the slip rates according to the rate-dependent theory (Kocks, 1998a),

Hutchinson and Budiansky (1976) and Kiryk and Petryk (1998) used isosurfaces of ω as a surrogate for the yield surface. One finds ω and Φ quite similar by keeping in mind that the positive and negative direction of a slip system is regarded as two distinct mechanisms in the previous Section, while they are combined here.

Thus, for a rate-independent approach we introduce a second regularized yield surface by

$$\Psi(\tilde{\mathbf{C}}\tilde{\mathbf{S}}, g) = \omega(\tilde{\mathbf{C}}\tilde{\mathbf{S}}, g) - \omega_c. \tag{4.88}$$

In the introduced notation, it is (again using double mechanisms to avoid absolute values)

$$\Psi(\tilde{\mathbf{C}}\tilde{\mathbf{S}}, g) = \frac{1}{n+1}\dot\gamma_0 \sum_{\alpha\in\mathcal{B}} g_\alpha \left(\phi^G_\alpha + 1\right)^{n+1} - \omega_c, \tag{4.89}$$

which is not directly connected with a regularization of the individual mechanisms' yield limit, but weighted with the respective critical resolved shear stresses. Thus in the vertices, a suitable rounding is achieved, while for single slip conditions the yield limit of the selected mechanism is in general not reproduced:

$$\phi^G_\alpha = \left(\frac{(n+1)\omega_c}{\dot\gamma_0\, g_\alpha}\right)^{\frac{1}{n+1}} - 1. \tag{4.90}$$

For different hardening states g_α of the mechanisms this cannot be obtained for more than one mechanism.

Accordingly, (4.46) yields

$$\begin{aligned}
\mathbf{P}^{-1}\dot{\mathbf{P}} &= -\lambda\dot{\gamma}_0 \sum_{\alpha\in\mathcal{B}} (\phi_\alpha^G + 1)^n \, \partial_{\tilde{\mathbf{C}}\tilde{\mathbf{S}}}\phi_\alpha, \\
\dot{z}_\beta &= -\lambda\dot{\gamma}_0 \sum_{\alpha\in\mathcal{B}} (\phi_\alpha^G + 1)^n \, \left(\partial_{g_\beta}\phi_\alpha - \phi_\alpha^G\right), \\
\lambda\Psi &= 0, \\
\lambda &\geq 0, \\
\Psi &\leq 0
\end{aligned} \tag{4.91}$$

resulting in

$$\lambda_\beta = \lambda\dot{\gamma}_0\theta_\beta. \tag{4.92}$$

The resulting λ_β are independent of the actual values of the hardening variable and dimensionless.

The same procedure as in the previous Section results in

$$\begin{aligned}
\lambda_\beta &= \sum_{\alpha\in\mathcal{B}} \frac{\theta_\beta\,\theta_\alpha}{\sum_{\gamma,\delta\in\mathcal{B}} \theta_\gamma\theta_\delta g_{\gamma\delta}^G} \mathbf{P}\star\tilde{\mathbf{A}}_\alpha\cdot\dot{\mathbf{E}}, \\
&= \sum_{\alpha\in\mathcal{B}} g_{\beta\alpha}^{G\ddagger}\mathbf{P}\star\tilde{\mathbf{A}}_\alpha\cdot\dot{\mathbf{E}}.
\end{aligned} \tag{4.93}$$

Note that the only difference to (4.82) is the exchange of θ_α^G with θ_α. Accordingly, using the slightly different definition $r_\alpha = \sum_{\beta\in\mathcal{B}} g_{\alpha\beta}^G\theta_\beta$, the property (4.85) is now

$$g_{\mu\nu}^G = \frac{r_\mu\, r_\nu}{\sum_{\gamma\in\mathcal{B}} \theta_\gamma\, r_\gamma} \qquad \mu,\nu\in\mathcal{B}. \tag{4.94}$$

4.4.3 Regular yield surfaces as replacement for multiple mechanisms

The use of the two regularized criteria is of particular interest in cases where the resulting equations of evolution coincide at least approximately with the multi-mode approach which can be regarded as the physical model. Any deviations are contributions of the vertex effect which is absent in the regularized models. We shall discuss this problem in the sequel.

An inclusion of only active systems $\mathcal{B}\subseteq\mathcal{A}$ can be neglected if one accepts the activation function as a suitable regularization. In this case the fact that each of the (doubled) mechanisms has a half space of the Mandel stress space as its elastic domain needs to be taken into account, e.g. by augmenting the activation function with Maccauley brackets $\langle x\rangle = \frac{1}{2}(|x|+x)$,

$$\theta_\alpha = \left\langle \phi_\alpha^G - 1\right\rangle^n \tag{4.95}$$

We shall now discuss, whether the application of a regularized yield criterion can be interpreted as the application of a pseudoinverse of the consistency matrix, at least under certain circumstances.

The definition of a pseudoinverse has been used in (4.85) and (4.94). Both can only be fulfilled if the matrix g^G is symmetric. Thus the conditions discussed in Section 4.3.3 have to be met, which is the case for small elastic deformations.

The pseudoinverse property for $g^{G\dagger}_{\alpha\beta}$ and $g^{G\ddagger}_{\alpha\beta}$ is fulfilled, if by $\frac{r_\alpha}{\sum_{\delta\in\mathcal{B}} g_\delta \theta_\delta} =: \frac{1}{N_\mathcal{B}}$ each entry of g^G can be reformulated as

$$g^G_{\alpha\beta} = \frac{r_\alpha}{N_\mathcal{A}} \quad \forall \alpha, \beta \in \mathcal{B} \subseteq \mathcal{A}, \tag{4.96}$$

which requires that all components $g^G_{\alpha\beta}$ are equal.

In cannot be expected that this property holds true in general but only in very special situations.

Accordingly, the regularized approach is not a generalized solution of the multi-mode approach, it is a distinct theory. Cases, where both coincide or differ are suitable to discuss the vertex effect. It will be shown that this is not a matter of special choice of material parameters but a matter of how a plastic process is continued.

4.5 The vertex effect

Section Overview
From a given state, different process continuations result in different material responses due to the loading condition and the distinct active set in a material with multiple plastic mechanisms. The nature of this vertex effect is explored by comparison of the multi-mode and the regularized approach of Sections 4.3 and 4.4.

4.5.1 Straight and kinked loading

Starting from a given state the active set $\mathcal{A}$ on a continuation process determines the way a material with multiple plastic mechanisms evolves.

The consistency matrix is a function of the state variables, thus the sign of the plastic multipliers can be obtained from the coupled loading condition (4.63). It is homogeneous of first order.

Accordingly, the active set can be obtained from the dual state variables and the direction of the elastic rate of Mandel's stress, the *loading direction*

$$\tilde{\mathbf{M}} = \frac{\frac{\mathrm{d}}{\mathrm{d}t}\,\tilde{\mathbf{C}}\tilde{\mathbf{S}}\Big|_{\mathbf{P},z=\mathrm{const}}}{\left\|\frac{\mathrm{d}}{\mathrm{d}t}\,\tilde{\mathbf{C}}\tilde{\mathbf{S}}\Big|_{\mathbf{P},z=\mathrm{const}}\right\|}. \tag{4.97}$$

$$\mathcal{A}(\tilde{\mathbf{C}}\tilde{\mathbf{S}}, g, \tilde{\mathbf{M}}) = \Big\{\beta |\, \phi_\beta(\tilde{\mathbf{C}}\tilde{\mathbf{S}}, g) = 0, \tilde{\mathbf{N}}_\beta \cdot \tilde{\mathbf{M}} > 0\Big\}. \tag{4.98}$$

The coupled loading condition (4.63) results in an implicit definition, which raises the need for an iterative approach.

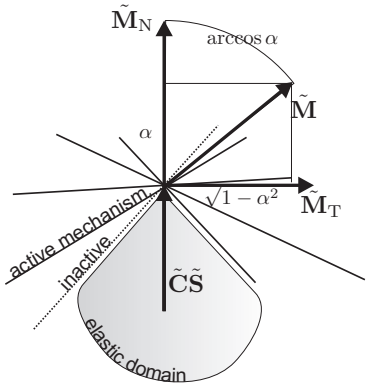

Fig. 4.2: Description of deviation from straight loading from a critical state by a single parameter

It shall prove useful to parametrize the continuation of a process relative to a *natural direction*, $\tilde{\mathbf{M}}_{\mathrm{N}}$. The regularized and the multi-mode approach coincide in this direction. Accordingly,

$$\tilde{\mathbf{M}} = \alpha\tilde{\mathbf{M}}_{\mathrm{N}} + \sqrt{1-\alpha^2}\tilde{\mathbf{M}}_{\mathrm{T}}, \tag{4.99}$$

where a decomposition in parts parallel to the natural direction $\tilde{\mathbf{M}}_{\mathrm{N}}$, and its complement, the tangential direction $\tilde{\mathbf{M}}_{\mathrm{T}}$ has been made. The latter can be computed from the projection

$$\left(\mathbb{I} - \tilde{\mathbf{M}}_{\mathrm{N}} \otimes \tilde{\mathbf{M}}_{\mathrm{N}}\right)[\tilde{\mathbf{M}}] = \tilde{\mathbf{M}} - \alpha\tilde{\mathbf{M}}_{\mathrm{N}} \tag{4.100}$$

and normalization

$$\tilde{\mathbf{M}}_{\mathrm{T}} = \frac{\tilde{\mathbf{M}} - \alpha\tilde{\mathbf{M}}_{\mathrm{N}}}{\sqrt{1-\alpha^2}}. \tag{4.101}$$

The loading direction is described by the *loading parameter*

$$\alpha = \tilde{\mathbf{M}}_{\mathrm{N}} \cdot \tilde{\mathbf{M}}, \tag{4.102}$$

namely the direction cosine of $\tilde{\mathbf{M}}$ with respect to $\tilde{\mathbf{M}}_{\mathrm{N}}$. Accordingly, $\alpha = 1$ is loading in the natural direction, while $\alpha = -1$ is reversed loading. $\alpha = 0$ is a 90-degree kink, that is not necessarily connected with neutral loading.

Inserting (4.99) into the loading criterion of (4.98), we obtain

$$\alpha > \alpha_\beta(g, \tilde{\mathbf{M}}_{\mathrm{N}}, \tilde{\mathbf{M}}) = \frac{|\tilde{\mathbf{N}}_\beta \cdot \tilde{\mathbf{M}}_{\mathrm{T}}|}{\sqrt{\left(\tilde{\mathbf{N}}_\beta \cdot \tilde{\mathbf{M}}_{\mathrm{N}}\right)^2 + \left(\tilde{\mathbf{N}}_\beta \cdot \tilde{\mathbf{M}}_{\mathrm{T}}\right)^2}}. \tag{4.103}$$

In cases of linear yield functions $\phi\alpha$, such as the Schmid law (4.74), the modified normal direction $\tilde{\mathbf{N}}_\beta$ does not depend on $\tilde{\mathbf{C}}\tilde{\mathbf{S}}$, only on the dual hardening variables g.

If the natural direction coincides with $\mathbf{N}_\beta$, (4.103) implies $\alpha > 0$ for loading. This is the case in presence of a single mechanism.

Clarifying the dependence of $\mathcal{A}$,

$$\mathcal{A}(\tilde{\mathbf{C}}\tilde{\mathbf{S}}, g, \tilde{\mathbf{M}}_\mathrm{N}, \tilde{\mathbf{M}}) = \left\{ \beta |\, \phi_\beta(\tilde{\mathbf{C}}\tilde{\mathbf{S}}, g) = 0, \alpha > \alpha_\beta(g, \tilde{\mathbf{M}}_\mathrm{N}, \tilde{\mathbf{M}}) \right\}. \tag{4.104}$$

(4.104) is still an implicit definition, as α_β depends on $\mathcal{A}$ via $\tilde{\mathbf{N}}_\beta$. Formally inserting the resulting active set in the equations of evolution (4.58) and (4.59), one obtains rate-independent constitutive functions

$$\begin{aligned} \mathbf{P}^{-1}\dot{\mathbf{P}} &= \hat{\mathbf{\Pi}}(\mathbf{C}, \mathbf{P}, z, \tilde{\mathbf{M}}_\mathrm{N}, \tilde{\mathbf{M}}) \\ \dot{z} &= \hat{z}(\mathbf{F}, \mathbf{P}, z, \tilde{\mathbf{M}}_\mathrm{N}, \tilde{\mathbf{M}}) \end{aligned} \tag{4.105}$$

that are valid at a yield vertex characterized by $\tilde{\mathbf{M}}_\mathrm{N}$ for a process continuation expressed by $\tilde{\mathbf{M}}$, which in turn is a linear function of $\dot{\mathbf{C}}$.

In contradiction to the classical single surface theory of plasticity, a complicated dependence on the loading parameter α is obvious. This direction dependence of the plastic flow $\mathbf{\Pi}$, in particular of the direction of $\mathbf{\Pi}$ is the vertex effect.

A phenomenological vertex model of plasticity based on the structure of (4.105) will be proposed in Chapter 5 on page 67.

4.5.2 Symmetric planar double slip

The idea is outlaid by a simple planar double slip model (Fig. 4.3). This standard example has also been worked out in Lubarda (2002, Section 12.13) and used in Peirce et al. (1982), Asaro (1983). Both slip systems are symmetricaly inclined at an angle ψ (not shown in the Figure). Thus, the slip direction vectors are $\tilde{\mathbf{d}}_1 = (\cos\psi, \sin\psi)$, $\tilde{\mathbf{d}}_2 = (-\cos\psi, \sin\psi)$. The slip plane normals are $\tilde{\mathbf{n}}_1 = (-\sin\psi, \cos\psi)$, $\tilde{\mathbf{n}}_2 = (\sin\psi, \cos\psi)$. The according Schmid functions are given by

$$\phi_\alpha = \tilde{\mathbf{C}}\tilde{\mathbf{S}} \cdot \mathrm{sym}\tilde{\mathbf{d}}_\alpha \otimes \tilde{\mathbf{n}}_\alpha - g_\alpha. \tag{4.106}$$

Accordingly, the vertex can be found at the intersection, i.e. at the planar stress state

$$\begin{aligned} \tilde{\mathbf{C}}\tilde{\mathbf{S}} &= a_1\, \tilde{\mathbf{d}}_1 \otimes \tilde{\mathbf{n}}_1 + a_2\, \tilde{\mathbf{d}}_2 \otimes \tilde{\mathbf{n}}_2 \\ a_i &= -\frac{1}{4}\frac{g_i}{\cos^2\psi\,(\cos^2\psi - 1)}. \end{aligned} \tag{4.107}$$

The symmetric state at $g_1 = g_2 = g$ yields the simple results

$$\begin{aligned} \tilde{\mathbf{M}}_\mathrm{N} &= \frac{\sqrt{2}}{2}\begin{bmatrix} 1 & 0 \\ 0 & -1 \end{bmatrix} \\ \tilde{\mathbf{M}}_\mathrm{T} &= \frac{1}{\sqrt{\cos^4\psi + \sin^4\psi}}\begin{bmatrix} 0 & \cos^2\psi \\ -\sin^2\psi & 0 \end{bmatrix}. \end{aligned} \tag{4.108}$$

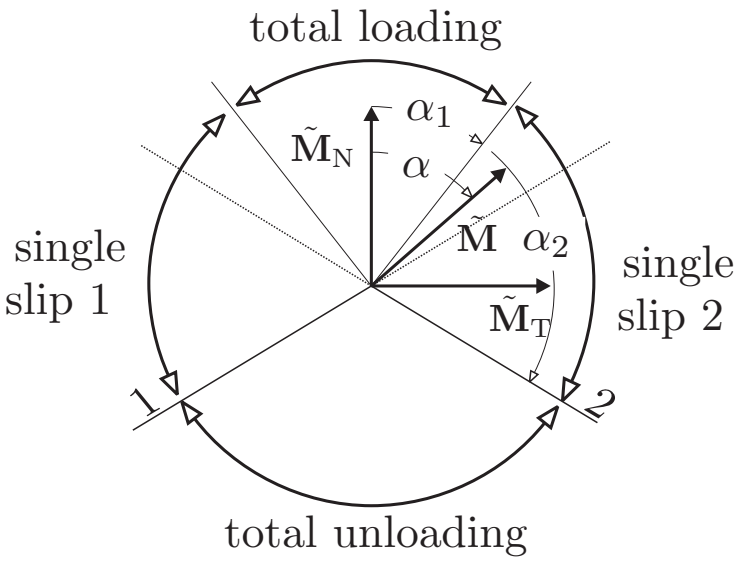

Fig. 4.3: Symmetric planar double slip model (Lubarda, 2002) outlined in Mandel's stress space

For simplicity, we assume isotropic elasticity at small elastic strain. The hardening model is

$$\dot{g}_\alpha = H\,[q + (1-q)\delta_{\alpha\beta}]\,\dot{\gamma}_\beta. \tag{4.109}$$

.

Double slip

For the case of double slip we obtain

$$\begin{aligned}
(g_{\alpha\beta}) &= \begin{pmatrix} 2G+H & -2G\,(\cos^2\psi - \sin^2\psi)^2 + q\,H \\ -2G\,(\cos^2\psi - \sin^2\psi)^2 + q\,H & 2G+H \end{pmatrix} \\
(g^{-1}_{\alpha\beta}) &= \frac{1}{\Gamma}\begin{pmatrix} (2G+H) & 2G\,(\cos^2\psi - \sin^2\psi)^2 - q\,H \\ 2G\,(\cos^2\psi - \sin^2\psi)^2 - q\,H & (2G+H) \end{pmatrix} \\
\Gamma &= (2G+H)^2 - \left(-2G\,(\cos^2\psi - \sin^2\psi)^2 + q\,H\right)^2
\end{aligned} \tag{4.110}$$

The generalized normals defined in (4.64) are

$$\begin{aligned}
\tilde{\mathbf{N}}_1 &= \Gamma^{-1}\left[(2G+H)\,\tilde{\mathbf{d}}_1 \otimes \tilde{\mathbf{n}}_1 + \left(2G\,(\cos^2\psi - \sin^2\psi)^2 - q\,H\right)\,\tilde{\mathbf{d}}_2 \otimes \tilde{\mathbf{n}}_2\right] \\
\tilde{\mathbf{N}}_2 &= \Gamma^{-1}\left[(2G+H)\,\tilde{\mathbf{d}}_2 \otimes \tilde{\mathbf{n}}_2 + \left(2G\,(\cos^2\psi - \sin^2\psi)^2 - q\,H\right)\,\tilde{\mathbf{d}}_1 \otimes \tilde{\mathbf{n}}_1\right]
\end{aligned} \tag{4.111}$$

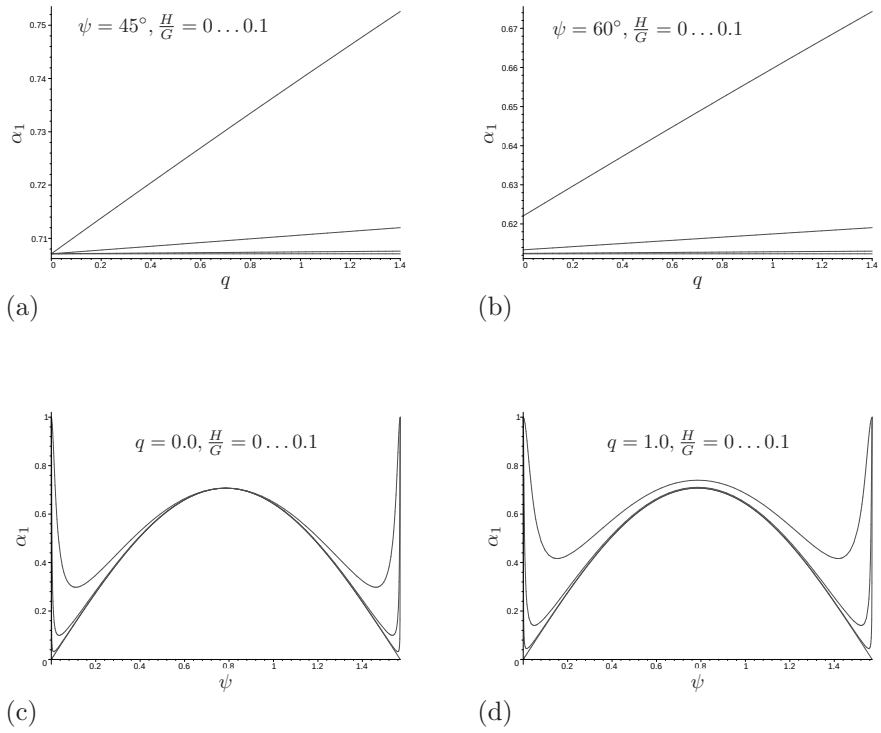

Fig. 4.4: Dependency of the total loading angle α_1 on $\frac{H}{G}$, q, and ψ

which results in a total loading cone confined due to symmetry by $A = \tilde{\mathbf{N}}_1 \cdot \tilde{\mathbf{M}}_{\mathrm{N}}$, $B = \tilde{\mathbf{N}}_1 \cdot \tilde{\mathbf{M}}_{\mathrm{T}}$, and

$$\alpha > \alpha_1 = \frac{B}{\sqrt{A^2 + B^2}}. \tag{4.112}$$

By simple manipulation one can express α_1 as a function of the dimensionless parameters $(\frac{H}{G}, q, \psi)$. The dependence on each of them is shown in Fig. 4.4. One finds that both $q = 0$ and $\psi = 45°$ have special properties. If both conditions coincide, $g_{\alpha\beta}$ is diagonal. Accordingly, α_1 is then independent of the nondimensional hardening modulus, $\frac{H}{G}$ (4.4 (a,c)). In the other cases the ratio of diagonal and non-diagonal terms that governs the direction of $\tilde{\mathbf{N}}_1$, is influenced by $\frac{H}{G}$ (4.4 (b,d)).

Note that $A = B$ for $q = 0$ or $H = 0$, leading to $\alpha_1 = \frac{\sqrt{2}}{2}$, and the total loading cone is the so called prolongation cone (Lubarda, 2002, Section 12.13). In the general case, α_1 is larger.

	$\mathcal{B}=\{1,2\}$	$\mathcal{B}=\{2\}$
Multi mode	$-(\tilde{\mathbf{M}}_1\otimes\tilde{\mathbf{M}}_1+\tilde{\mathbf{M}}_2\otimes\tilde{\mathbf{M}}_2)\cdot\mathbf{P}^\top\dot{\mathbf{E}}\mathbf{P}$	$-(\tilde{\mathbf{M}}_2\otimes\tilde{\mathbf{M}}_2)\cdot\mathbf{P}^\top\dot{\mathbf{E}}\mathbf{P}$
Regularized	$-(\tilde{\mathbf{M}}_\mathrm{N}\otimes\tilde{\mathbf{M}}_\mathrm{N})\cdot\mathbf{P}^\top\dot{\mathbf{E}}\mathbf{P}$	$-(\tilde{\mathbf{M}}_2\otimes\tilde{\mathbf{M}}_2)\cdot\mathbf{P}^\top\dot{\mathbf{E}}\mathbf{P}$

Tab. 4.2: Flow rules of multi-mode and regularized approach

Accordingly, we obtain the plastic multipliers from (4.57)

$$\begin{aligned}\lambda_1&=\tilde{\mathbf{N}}_1\cdot 2G\mathbf{P}^\top\dot{\mathbf{E}}\mathbf{P}\\ \lambda_2&=\tilde{\mathbf{N}}_2\cdot 2G\mathbf{P}^\top\dot{\mathbf{E}}\mathbf{P}.\end{aligned}\tag{4.113}$$

Insertion into the flow rule (4.58) results in

$$\begin{aligned}\mathbf{P}^{-1}\dot{\mathbf{P}}&=\sum_{\alpha,\beta=1}^{2} g^{-1}_{\beta\alpha}\tilde{\mathbf{d}}_\beta\otimes\tilde{\mathbf{n}}_\beta\otimes\tilde{\mathbf{d}}_\alpha\otimes\tilde{\mathbf{n}}_\alpha[2G\mathbf{P}^\top\dot{\mathbf{E}}\mathbf{P}]\\&=\mathbb{A}[\mathbf{P}\dot{\mathbf{E}}\mathbf{P}].\end{aligned}\tag{4.114}$$

The nonzero elements of the linear operator $\mathbb{A}$ are given by

$$\begin{aligned}
A_{1111} &= -2\tfrac{2G}{\Gamma}\cos^2\psi\sin^2\psi & \left(-2G(2\cos^2\psi-1)^2-(2G+H)+q\,H\right)\\
A_{1122} &= +2\tfrac{2G}{\Gamma}\cos^2\psi\sin^2\psi & \left(-2G(2\cos^2\psi-1)^2-(2G+H)+q\,H\right)\\
A_{2211} &= +2\tfrac{2G}{\Gamma}\cos^2\psi\sin^2\psi & \left(-2G(2\cos^2\psi-1)^2-(2G+H)+q\,H\right)\\
A_{2222} &= -2\tfrac{2G}{\Gamma}\cos^2\psi\sin^2\psi & \left(-2G(2\cos^2\psi-1)^2-(2G+H)+q\,H\right)\\
A_{1212} &= +2\tfrac{2G}{\Gamma}\cos^4\psi & \left(-2G(2\cos^2\psi-1)^2+(2G+H)+q\,H\right)\\
A_{1221} &= -2\tfrac{2G}{\Gamma}\cos^2\psi\sin^2\psi & \left(-2G(2\cos^2\psi-1)^2+(2G+H)+q\,H\right)\\
A_{2112} &= -2\tfrac{2G}{\Gamma}\cos^2\psi\sin^2\psi & \left(-2G(2\cos^2\psi-1)^2+(2G+H)+q\,H\right)\\
A_{2121} &= +2\tfrac{2G}{\Gamma}\sin^4\psi & \left(-2G(2\cos^2\psi-1)^2+(2G+H)+q\,H\right),
\end{aligned}\tag{4.115}$$

which once more can be shown not to depend on G but only on the nondimensional parameters $(\frac{H}{G},q,\psi)$. The particular simple case $H=0$, $\psi=45^\circ$ renders for the nonzero elements of above

$$A_{ijij}=1\qquad A_{ijji}=-1,\tag{4.116}$$

and the eigenvalues are 0 double (a matter of the insufficient number of mechanisms), and 1 double referring to the nondefective eigenspace spanned by $(\tilde{\mathbf{M}}_\mathrm{N},\tilde{\mathbf{M}}_\mathrm{T})$. Using any of the (here coincident) regularized approaches, we obtain

$$A_{1111}=A_{2222}=1\qquad A_{1122}=A_{2211}=-1,\tag{4.117}$$

with eigenvalues 0 triple (even less "mechanisms"), 1 single and the according eigenvector is $\tilde{\mathbf{M}}_\mathrm{N}$. Both flow rules are compared in Table 4.2. The two approaches yield flow rules that coincide for $\tilde{\mathbf{M}}=\tilde{\mathbf{M}}_\mathrm{N}$. The respective plastic potentials (and yield limits) are plotted in Fig. 4.5(a).

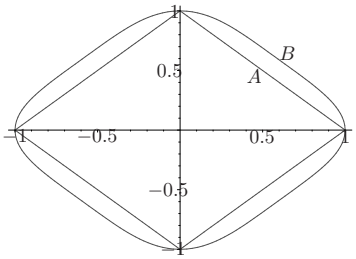

(a) Deviation of the yield limits of multi mode (A) and regularized (B) approach

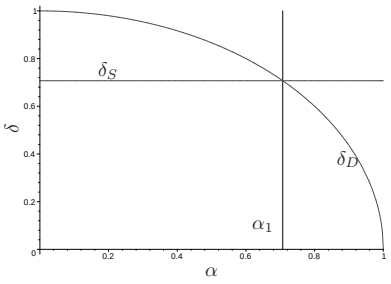

(b) Relative Error $\delta = \frac{\|\hat{\mathbf{\Pi}}_R - \hat{\mathbf{\Pi}}_{MM}\|}{\|\hat{\mathbf{\Pi}}_{MM}\|}$ vs. α for kinked processes on double (D) and single (S) slip

Fig. 4.5: Multi mode and regularized approach compared

Accordingly, straight processes are properly modeled by the regularized model, while it is only an approximation for kinked processes. In particular the lateral ($\tilde{\mathbf{M}}_{\mathrm{T}}$-) component of plastic flow is missing. To show the magnitude of error, the relative norm of the difference in the flow rule

$$\delta(\alpha) = \frac{\left\| \hat{\mathbf{\Pi}}_R - \hat{\mathbf{\Pi}}_{MM} \right\|}{\|\hat{\mathbf{\Pi}}_{MM}\|} \tag{4.118}$$

has been plotted vs. α in Fig. 4.5(b). It shows that only for $\alpha = 1$, i.e. for the straight process that is contained in the nondefective eigenspaces of both models, the two approaches yield the same result.

Single slip

If only slip system 2 is active, the solution is simple. One obtains

$$\lambda = \frac{2G}{2G + H} = \tilde{\mathbf{M}}_2 \cdot \mathbf{P}^{\top} \dot{\mathbf{E}} \mathbf{P}. \tag{4.119}$$

The flow rule has again been shown in Table 4.2.

The regularized approach is the same as above. One finds the deviation from the single slip solution δ_S even larger than the double slip case (Fig. 4.5(b)).

However, if only the single active mechanism is included in the set $\mathcal{B}$, the situation changes. For the double slip cone, the regularized plastic potential is as depicted in 4.5(a) (B), while in the single slip cone, the regularized approach results in the same equations as the single slip solution and 4.5(a) (A) is applied.

The relative error of the approximation of flow direction by the regularized

$\mathcal{B}$	A/B	$\|\delta(\alpha)\|_2$
$\{1,2\}$, $-\alpha_1 \leq \alpha \leq 1$	B only	0.8857
$\{2\}$, $-\alpha_1 \leq \alpha < \alpha_1$; $\{1,2\}$, $\alpha_1 \leq \alpha \leq 1$	A and B	0.2782

Tab. 4.3: Improvement of the approximation of a regularized flow rule by information about the active set

approach can be measured by

$$\|\delta(\alpha)\|_2 = \sqrt{\int_{\alpha=-1}^{1} (\delta(\alpha))^2 \, \mathrm{d}\alpha}. \tag{4.120}$$

The result for different approximations can be found in Table 4.3. If only the active set obtained in a cone is used for the regularization, the approach is much better.

The direction of plastic flow can most simply be described by

$$\beta_{\mathbf{\Pi}} = \frac{\mathbf{\Pi}}{\|\mathbf{\Pi}\|} \cdot \tilde{\mathbf{M}}_{\mathrm{N}}. \tag{4.121}$$

It has been plotted for the solution obtained by the multi mode approach for double slip β_D and single slip β_S, and the regularized approach for $\mathcal{B} = \{1,2\}$, β_R. One concludes that the separate regularization for each cone is like an approximation of the true solution by a step function, and a lateral component of plastic flow is generated.

At a single point in each cone, the proper multi mode direction is obtained.

4.5.3 Regularized plastic potential and multislip

By the investigation of the symmetric double slip example the last section showed that for all slip systems active, the regularization coincides with the multi-mode theory in a single direction.

To study the influence of a larger number of simultaneously active slip systems, the planar double slip model was extended by an addition of more and more mechanisms in the same plane, leading to $N \in \{3,5,7,9,11,13,23,43\}$ mechanisms (see last drawing in Fig. 4.7). Although this is not a physical example, the typical properties of single- and polycrystals in activating different sets of slip systems for different process directions are included.

For different processes, the active set $\mathcal{A}$ was investigated according to the loading condition (4.103). The whole range $\alpha \in [-1,1]$ was thus split in disjoint intervals $[-1,1] = \bigcup_i \mathcal{C}_i$ each describing one cone in the $\dot{\mathbf{E}}$-space with a distinct active set $\mathcal{A}_i$.

For each cone $\mathcal{C}_i$ separately, the regularized approach was used setting $\mathcal{B} = \mathcal{A}_i$ to obtain a flow potential $\Phi_i(\tilde{\mathbf{C}}\tilde{\mathbf{S}}, g)$ for each cone as introduced in (4.76). These functions Φ_i define a single but piecewise defined plastic potential Φ^* that

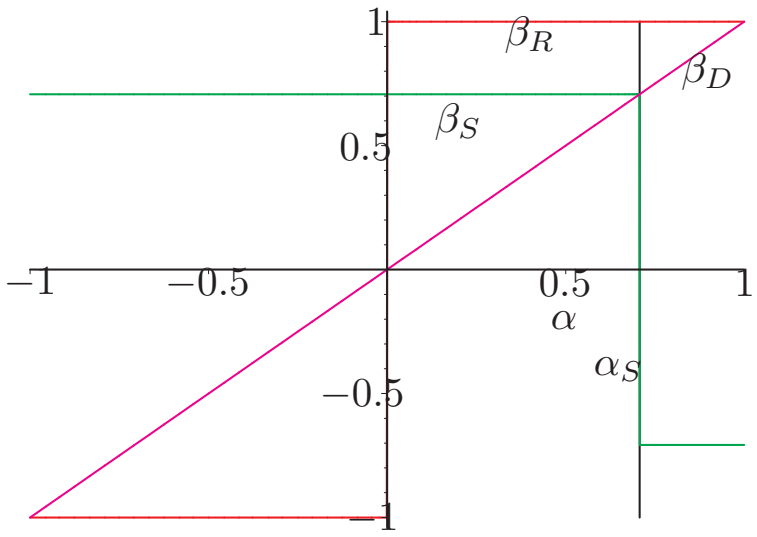

Fig. 4.6: Approximation of the flow direction by regularization for each cone separately

transfers the direction-dependence of $\mathcal{A}_i$ into the flow rule. By application of (4.58) to the case of a single mechanism, this piecewise plastic potential defines a flow rule,

$$\hat{\mathbf{\Pi}}(\tilde{\mathbf{C}}\tilde{\mathbf{S}}, g, \tilde{\mathbf{M}}_{\mathrm{N}}, \tilde{\mathbf{M}}_{\mathrm{T}}, \alpha) = -\frac{1}{g^*}\partial_{\tilde{\mathbf{C}}\tilde{\mathbf{S}}}\,\Phi^* \otimes \tilde{\mathbf{A}}[\mathbf{P}^\top \dot{\mathbf{E}}\mathbf{P}]. \tag{4.122}$$

β of (4.121) was used to compare the direction of plastic flow with the multi-mode approach (Fig. 4.7) Here, the loading domain and range of $\beta(\alpha)$ in were normalized to $[-1, 1]$ and $[0, 1]$ to facilitate the comparison.

One finds that the direction of plastic flow is constant in each cone of the multi-mode approach but varies in the regularization. Only in the total loading direction, both results coincide. However, the smooth result based on the combined plastic potential Φ^* yields a lower bound, i.e. the deviation from the response to a proportional process continuation is overestimated.

With an increasing number of mechanisms the sizes of each single constitutive cones shrink and in the limit a continuous dependence on the direction of $\dot{\mathbf{E}}$ results as shown by the vanishing rudiments of the steps can be found.

Accordingly, the piecewise defined plastic potential Φ^* turns into a continuous function of the process direction for a very large number of mechanisms.

4.5.4 Conclusion

In comparing the multi-mode plasticity in single and double slip and the according regularized approach, the vertex effect has been clarified:

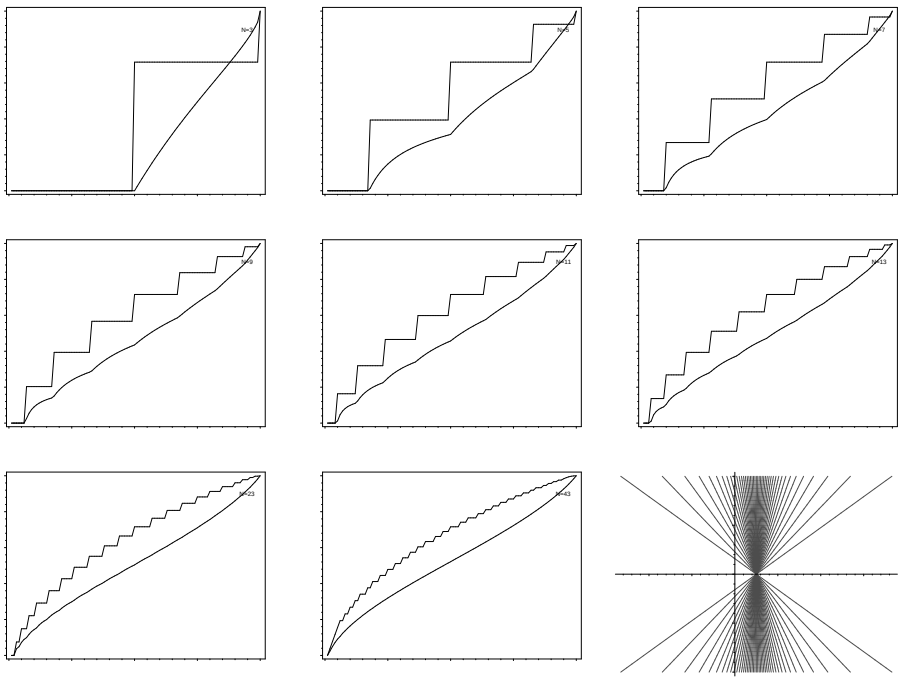

Fig. 4.7: The direction of plastic flow β vs. α obtained for multi-mode plasticity and its regularisation for each cone separately for an increasing number $(3 \ldots 43)$ of mechanisms.

The rank of the incremental material operator of the multi-mode approach is higher than in the according regularization, leading to the linear vertex effect, i.e. a dependence of the direction of plastic flow on the process continuation.

In addition, the loading condition changes the active set again in a process-dependent manner and incorporates a nonlinear kind of vertex effect.

In the presence of a large number of mechanisms, the gross effect is determined by the natural direction $\tilde{\mathbf{M}}_{\mathrm{N}}$ (proportional loading direction) and a scalar measure of deviation from this direction α in the lateral direction $\tilde{\mathbf{M}}_{\mathrm{T}}$.

It has been shown by the example of regularization in the distinct constitutive cones that it is at least in principle possible to reproduce such an effect by the introduction of a single scalar plastic potential with a dependence on the process continuation by ($\tilde{\mathbf{M}}_{\mathrm{N}}$, $\tilde{\mathbf{M}}_{\mathrm{T}}$, α) as a gross model for the many existing constitutive cones.

Part II

PLASTICITY WITH YIELD VERTICES

5. SIMULATION-BASED ANALYSIS OF YIELD-VERTEX DEVELOPMENT

Section Overview
The Taylor-Lin model is used to simulate the subsequent yield surfaces of a copper polycrystal. Using an appropriate criterion, the vertex formation near the prestress and the traveling of the vertex with the stress process can be found.

5.1 Micromechanical Investigation of subsequent yield surfaces

The vertex effect in metals is the consequence of the many existing mechanisms of plastic deformation. According to the results of Section 4.5, the flow rule has a tangential component in addition to the normal one of classical smooth theories of plasticity.

The connection with corners in yield surfaces and the insufficient experimental evidence for these corners lead to the necessity of numerical experiments with a polycrystal model.

The determination of subsequent yield surfaces after a defined prestrain is a classical application of crystal plasticity. From the early publications (Bishop and Hill, 1951b), computations of the macroscopic yield surface have been done based on averagein properties of the grains alone. However, in the presence of texture, nonisotropic hardening and residual stresses computations based on the elastic domain alone are questionable for the evolution of yield surface (Zattarin et al., 2004). Instead, overall process properties have to be taken into account.

However, fruitful approaches have been used in the literature, based on homogenization methods.

Kiryk and Petryk (1998) used a self-consistent approach to compute a macroscopic viscous flow potential as proposed by Hutchinson (1970). They compared isolines of this potential with experimentally obtained subsequent yield surfaces.

Using an FEM-based polycrystal model, Kraska and Bertram (1996) used the average dissipated power as a criterion for macroscopic plasticity. In Kraska (1998), yield surfaces for copper polycrystals were computed for different thresholds. Small thresholds exhibited a vertex-like structure in the direction of preloading, while larger critical values lead to smooth surfaces.

A rate independent self consistent model was used by Zattarin et al. (2004) for straight and kinked process paths. They reported primary and secondary

vertices (after a change of strain direction) to be formed in the vicinity of the prestress point. The yield criterion has been defined by an engineering strain of 0.01%.

5.1.1 Usage of the Taylor-Lin model

Here, the conceptually simpler Taylor-Lin model has been used as laid out in Schurig et al. (2005). It is up to a certain degree capable of representing the crystallographic texture, anisotropic and distortional hardening and to a certain degree the intergranular residual stresses (Aris, 2000).

Based on the assumption of homogeneous deformations established by Taylor (1938), we assume for every grain κ an identical (externally prescribed) velocity gradient,

$$\mathbf{L}_\kappa \equiv \bar{\mathbf{L}}. \tag{5.1}$$

Each one is treated by the theory of multi-mode plasticity. To facilitate the use of the viscous flow potential of (4.86), the slip rates were determined by the approach of Rice (1970),

$$\dot{\gamma}_\alpha = \dot{\gamma}_0 \left| \frac{\tau_\alpha}{\tau_\alpha^c} \right|^n \operatorname{sign}\tau_\alpha. \tag{5.2}$$

As a simple hardening model for the critical resolved shear stresses, the hardening model used by Böhlke (2001) and the material parameters used there were applied (see Table 5.1 for a summary).

$$\begin{aligned} \tau_{\kappa\alpha}^c &= \tau_0^c + \sum_{\alpha=1}^{N} H q_{\alpha\beta} \rho_\beta \\ q_{\alpha\beta} &= q + (1-q)\delta_{\alpha\beta} \\ \dot{\rho}_\alpha &= b(1-\rho_\alpha)|\dot{\gamma}_\alpha| \end{aligned} \tag{5.3}$$

The stress acting in a grain can be determined by (4.31) or equivalent formulations. According to the theorem of averaging (Hill, 1952, Krawietz, 1986, Petryk, 1998), the homogeneuos strain assumption allows to obtain the macroscopic Kirchhoff stress by averaging of the local Kirchhoff stresses, each of them assumed to be homogeneous in the according grain,

$$\bar{\boldsymbol{\tau}} = \frac{\sum_{\kappa=1}^{N} f_\kappa \boldsymbol{\tau}_\kappa}{\sum_{\kappa=1}^{N} f_\kappa}. \tag{5.4}$$

N is the number of grains and f_κ is their respective reference volume fraction. Equal grain size has been assumed, thus $f_\kappa = \frac{1}{N}$. Due to the summation in (5.4), $\bar{\boldsymbol{\tau}} = \mathbf{0}$ can be achieved in presence of a (self-equilibrated) transgranular residual stress state (residual stresses of the second kind, Aris (2000)). The model is not capable of representing macroscopic or sub-granular residual stresses (first and third kind). The complete model equations are summarized in Table 5.1.

$\mathbf{L}_\kappa \equiv \mathbf{L}$	(5.1)	strain localization
$\dot{\mathbf{F}}_\kappa \mathbf{F}_\kappa^{-1} = \mathbf{L}_\kappa$		evolution of $\mathbf{F}$
$\mathbf{L}_\kappa = \tilde{\mathbf{L}}_\kappa - \tilde{\mathbf{F}}_\kappa \mathbf{P}_\kappa^{-1} \dot{\mathbf{P}}_\kappa \tilde{\mathbf{F}}_\kappa^{-1}$	(4.35)	evolution of elastic transformation
$\mathbf{P}_\kappa^{-1} \dot{\mathbf{P}}_\kappa = -\sum_{\alpha=1}^{N} \dot{\gamma}_{\kappa\alpha} \partial_{\tilde{\mathbf{C}}_\kappa \tilde{\mathbf{s}}_\kappa} \phi_{\kappa\alpha}$	$(4.50)_1$	flow rule
$\tau^c_{\kappa\alpha} = \tau^c_0 + \sum_{\alpha=1}^{N} H q_{\alpha\beta} \rho_\beta$		
$q_{\alpha\beta} = q + (1-q)\delta_{\alpha\beta}$	(5.3)	hardening rule (Böhlke, 2001)
$\dot{\rho}_\alpha = b(1-\rho_\alpha)\lvert\dot{\gamma}_\alpha\rvert$		
$\dot{\gamma}_{\kappa\alpha} = \dot{\gamma}_0 \left\lvert \frac{\tau_{\kappa\alpha}}{\tau^c_{\kappa\alpha}} \right\rvert^n \operatorname{sign} \tau_{\kappa\alpha}$	(5.2)	slip rates

Tab. 5.1: Set of equations of the Taylor-Lin model

α	$\tilde{\mathbf{d}}_\alpha$	$\tilde{\mathbf{n}}^\alpha$
1	$(0,1,1)/\sqrt{2}$	$(1,1,-1)/\sqrt{3}$
2	$(1,0,1)/\sqrt{2}$	$(1,1,-1)/\sqrt{3}$
3	$(1,-1,0)/\sqrt{2}$	$(1,1,-1)/\sqrt{3}$
4	$(0,1,-1)/\sqrt{2}$	$(1,-1,-1)/\sqrt{3}$
5	$(1,0,1)/\sqrt{2}$	$(1,-1,-1)/\sqrt{3}$
6	$(1,1,0)/\sqrt{2}$	$(1,-1,-1)/\sqrt{3}$
7	$(0,1,1)/\sqrt{2}$	$(1,-1,1)/\sqrt{3}$
8	$(1,0,-1)/\sqrt{2}$	$(1,-1,1)/\sqrt{3}$
9	$(1,1,0)/\sqrt{2}$	$(1,-1,1)/\sqrt{3}$
10	$(0,1,-1)/\sqrt{2}$	$(1,1,1)/\sqrt{3}$
11	$(1,0,-1)/\sqrt{2}$	$(1,1,1)/\sqrt{3}$
12	$(1,-1,0)/\sqrt{2}$	$(1,1,1)/\sqrt{3}$

γ_0	$1e-3$
n	80
τ^c_0	16.0 MPa
b	15
H	10 MPa
c_{1111}	168.0 MPa
c_{1122}	121.4 MPa
c_{2323}	75.4 MPa

Tab. 5.2: Octahedral slip systems numbered after Kocks (1970) (left) and material parameters of the Taylor-Lin model (right)

Table 5.2 lists the according material parameters used for copper. The initial data for each grain contained the given values and an initial orientation distribution $\mathbf{P}_\kappa = \mathbf{Q}_\kappa$ optimized for isotropy using the algorithm proposed by Böhlke and Bertram (1998). The number of grains is $N = 1024$.

5.1.2 The viscous flow potential as a yield indicator

The regularized approaches of Section 4.4 can be used as a surrogate for the yield surface of a single crystal, if the conditions of 4.4.3 are fulfilled.

For each single grain, we use the viscous flow potential of (Rice, 1970) in (4.86). A homogenization is possible (Lubarda, 2002, e.g.) and results in a macroscopic flow potential,

$$\bar{\omega} = \frac{1}{|\mathcal{B}|} \int_{\mathcal{B}} \omega \, \mathrm{d}V. \tag{5.5}$$

Here, the integration takes place over the reference volume occupied by the polycrystal.

The computation of $\bar{\omega}$ is performed under the assumption that all deformations are elastic until a critical threshold is reached. Thus

$$\Phi_\omega(\tilde{\mathbf{C}}\tilde{\mathbf{S}}, \omega_c) = \bar{\omega} - \omega_c \tag{5.6}$$

defines an indicator function for a sub-level set of the macroscopic flow potential.

Thus, from the knowledge of the crystallite yield loci, the macroscopic yield locus can be obtained, provided that Φ_ω is a suitable indicator of yield.

5.1.3 The dissipated power as a path dependend yield criterion

Technical definitions of the yield point (Ikegami, 1982) cannot detect the boundary of the elastic domain without producing at least a small amount of plastic deformation.

A similar approach is to define the yield point on a prescribed process path as the instant where the dissipated power reaches a threshold value that can be regarded as small (Kraska and Bertram, 1996). Usually this is defined as a fraction of the total average stress power.

$$\bar{d} = \frac{\frac{1}{N} \sum_\kappa \sum_\alpha \tau_\alpha \dot{\gamma}_\alpha}{\bar{\boldsymbol{\tau}} \cdot \bar{\mathbf{D}}} \tag{5.7}$$

can be used to define such a criterion. Fig. 5.1 shows that the dissipation criterion is useful in the hardening and non-hardening case. By probing in different radial directions, an approximation of the macroscopic yield locus can be obtained.

5.1.4 The initial yield surface

Both approaches have been used to determine the initial yield locus of the copper polycrystal. For that purpose, a number of standard processes has been

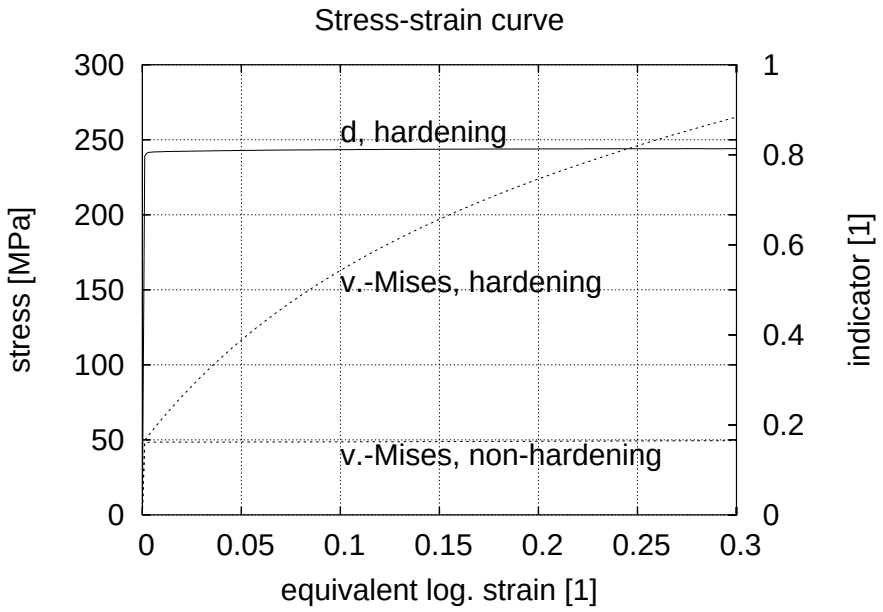

Fig. 5.1: Simulated stress-strain-curve of a polycrystal: von-Mises equivalent stress in hardening and non-hardening case, dissipated power fraction d.

used (Tab. 5.3). Tension describes an elongation with volume-preserving lateral contraction. Shear is a symmetric shear process which is similar to the idealized rolling process (identical for isotropic material).

The isoline of the flow potential at $\bar{\omega} = 1$ in the rolling-tension (see Tab. 5.3 for definition) section of the stress space has been determined out of the virgin state in Fig. 5.2a. In addition, radial processes with inelastic behaviour lead to isolines of the dissipation at $\bar{d} = 25\%$. Both yield comparable curves that approximate Tresca's criterion of maximum shear. A rounding of the vertices is obvious, an effect that is stronger in the flow potential for comparable thresholds.

The exact usage of both indicators for the first yield is shown in Fig. 5.2 b. A plane strain compression test with $\bar{\mathbf{L}} = 0.001 \frac{\mathbf{A}_{\text{rolling}}}{\|\mathbf{A}_{\text{rolling}}\|}$ was started out of the virgin state. Together with the v.-Mises equivalent stress, the dissipative power ratio (inelastic process) and the viscous flow potential (elastic process) were plotted.

A practically linear elastic behaviour is found up to $\bar{d} = 0.25$ or $\bar{\omega} = 1$ (marked C). At the same time, the dissipation increases massively.

Elastic reversal of the process reveals the plastic proof strain remaining at label A. At the total unloaded state $\bar{\omega}$ reaches a value as small as 10^{-99}. A value of $\epsilon_{\log} = 2 \times 10^{-5}$ is found. This can be regarded as a very strict criterion for the onset of yield, differing orders of magnitude from technical definitions.

It is possible to define even sharper criteria, such as $\bar{\omega} = 10^{-9}$. From (4.86) we conclude for only one slip system contributing,

$$\frac{\tau}{\tau^c} = \sqrt[n+1]{\frac{N(n+1)}{\dot{\gamma}_0 \tau^c} \bar{\omega}} \approx 0.93, \tag{5.8}$$

thus $\bar{\omega} = 10^{-9}$ really establishes an approximate criterion for first yield.

Further, the reversed process exhibits a small Bauschinger effect as the critical flow potential is reached in negative direction at a lower stress level. This effect has been explained by the residual microstresses by many authors, e.g. Kraska (1998), if kinematical hardening is absent.

5.1.5 Subsequent yield surfaces

First, volume preserving tension was chosen as the prestrain process. The equivalent strain finally reached $\epsilon_{eq} = 0.1$ (moderate strain). At different stages, the aggregate was elastically unloaded. From that state, radial processes were used to draw isolines of the viscous flow potential and the dissipated power fraction. These stages are shown by arrows in Fig. 5.3. Definitions of process directions and stages are shown in Table 5.3.

For $\bar{\omega} = 1$, the result is given in Fig. 5.4a. In the beginning, a strong distortion of the initially ellipsoidal shape can be seen. In the first subsequent line at a prestrain as small as $\epsilon_{\log} = 2.5 \times 10^{-4}$ at the very onset of plasticity, a rounded vertex can already be seen. The rounding could be minimized by using a smaller critical value.

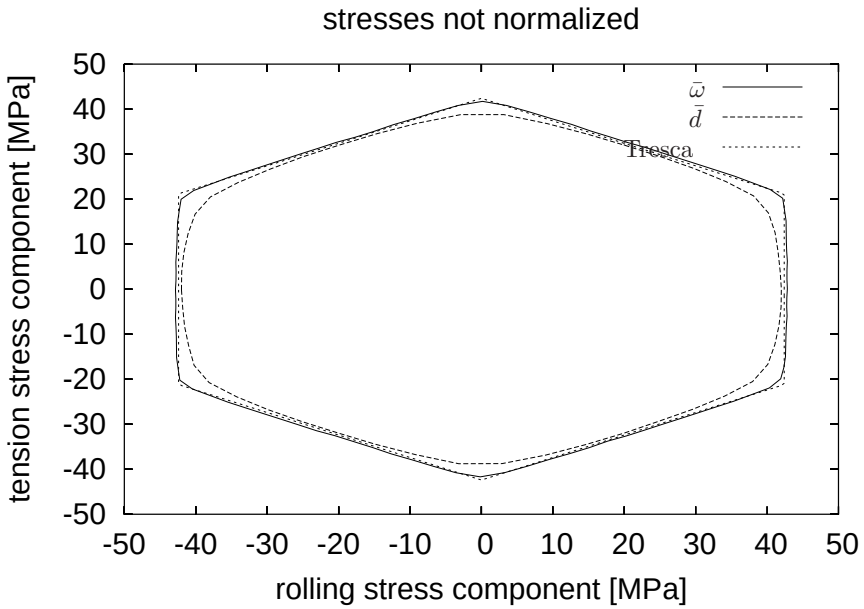

a

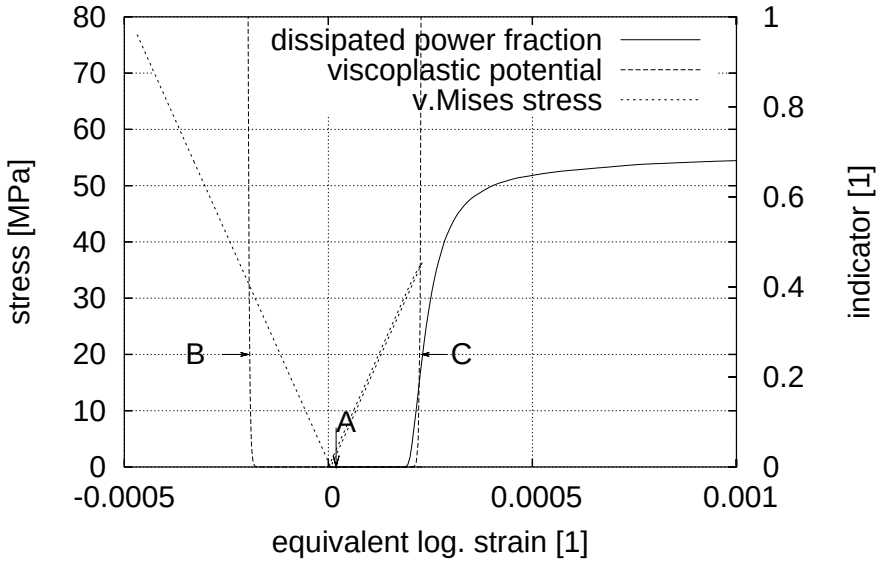

b

Fig. 5.2: Flow potential $\bar{\omega}$ and dissipation ratio $\bar{d}$ as indicators of yield. Initial yield surfaces (a) and comparison of stress and indicators on a loading-unloading-reversed loading process (b)

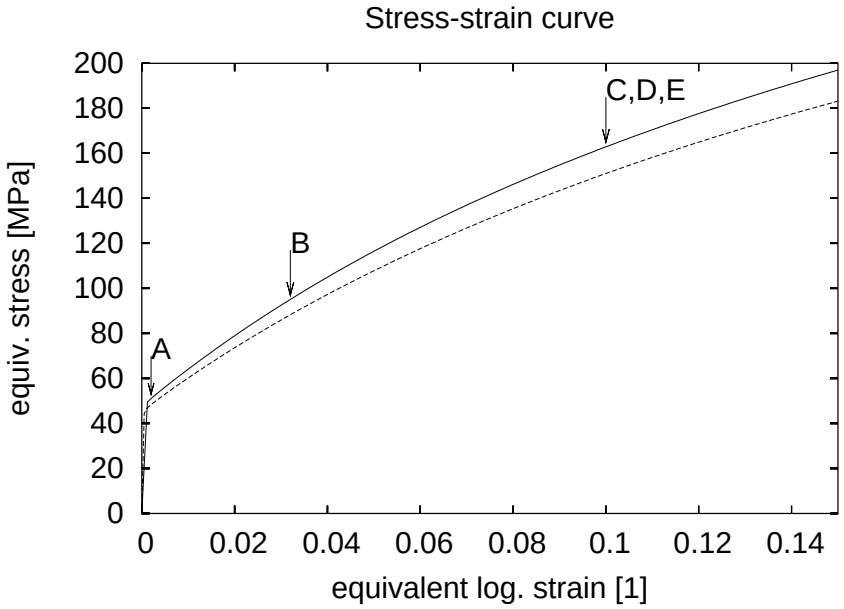

a

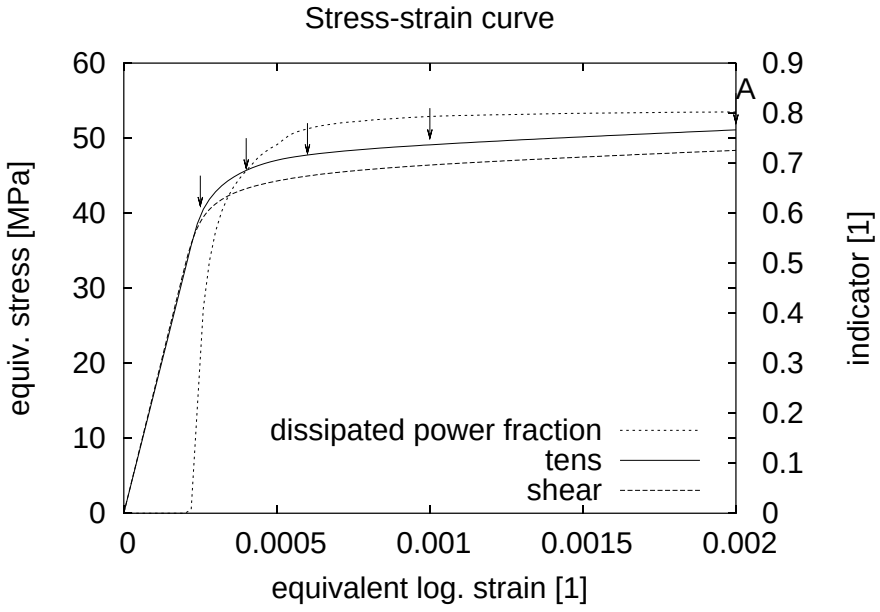

b

Fig. 5.3: Stress-strain curve and position of subsequent yield surfaces (arrows)

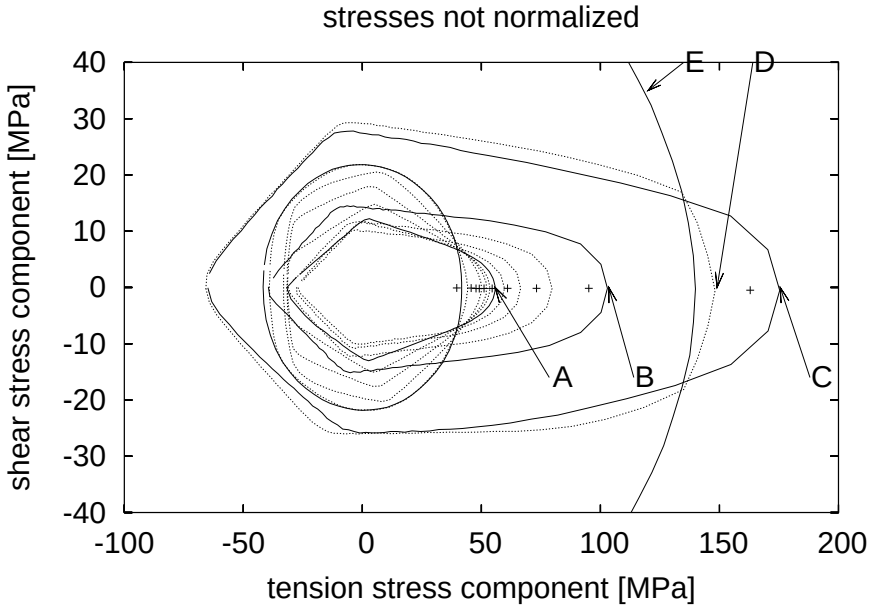

a

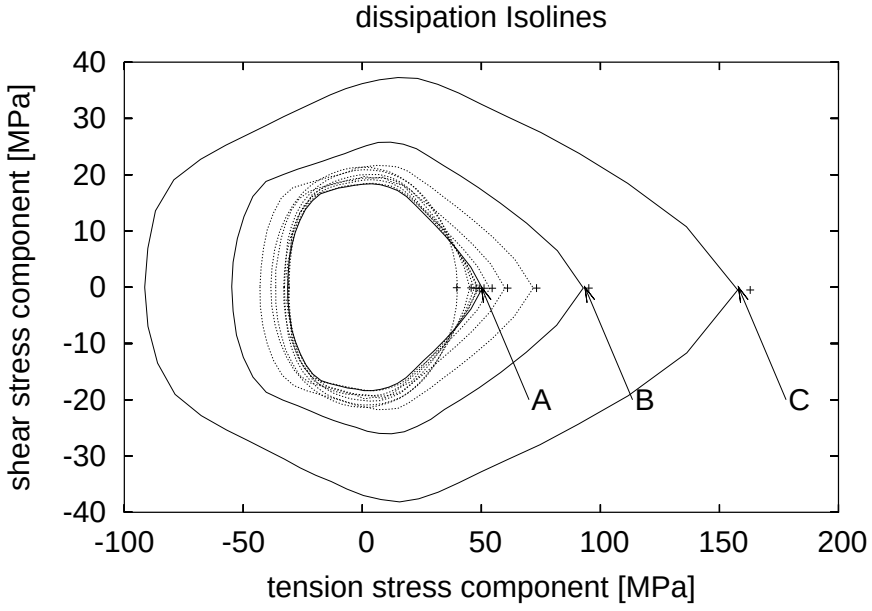

b

Fig. 5.4: Flow potential (a) and dissipation (b) isolines as indicators for subsequent yield surfaces after different tension prestrains

Label	**A**	Description
tension	$\begin{bmatrix} 1 & 0 & 0 \\ 0 & -\frac{1}{2} & 0 \\ 0 & 0 & -\frac{1}{2} \end{bmatrix}$	Volume-preserving tension
shear	$\begin{bmatrix} 0 & 1 & 0 \\ 1 & 0 & 0 \\ 0 & 0 & 0 \end{bmatrix}$	Symmetric shear
rolling	$\begin{bmatrix} 0 & 0 & 0 \\ 0 & 1 & 0 \\ 0 & 0 & -1 \end{bmatrix}$	Plane strain compression (idealized rolling)

$\epsilon_{\log}$	0	2.5×10^{-4}	4×10^{-4}	6×10^{-4}	1×10^{-3}	2×10^{-3}
Label						A
$\epsilon_{\log}$	4×10^{-3}	8×10^{-3}	1.6×10^{-2}	3.2×10^{-2}	1×10^{-1}	
Label				B	C	

Tab. 5.3: Definition of standard processes and process stages

From the line corresponding to $\epsilon_{\log} = 2 \times 10^{-3}$ on (labeled A), after the range of incipient plastic flow, the distortion is not predominant any more. Instead, a nearly self-similar growth takes place.

Also, for the same stages of a tension process, the dissipated power was used to produce isolines in Fig. 5.4b. While the initial isolines for both indicators are similar, in the follow-up they develop differently. The dissipation criterion exhibits a lower amount of distortion and a much more pointed vertex.

In a similar manner, prestrain processes defined by the shear and rolling direction have been explored. The results are shown in Fig. 5.5 and Fig. 5.6.

The initial shape of the isosurfaces is different, since the plots are in different sections of the stress space. However, in both cases the main features of development of the subsequent yield surfaces are similar.

The isolines of the flow potential after a certain plastic strain exhibit a strong distortion. Finally, the shape is completely changed and does not reproduce the expected shape of a finite area with a vertex any more.

In contrast, the distortion of the dissipation isolines is smaller, and the yield vertex can be clearly identified.

In all plots, the stress point that was reached during the prestrain process is marked. The critical thresholds were defined according to the initial yield point. Obviously, this threshold remains valid for the dissipation criterion, but not in the flow potential case.

An explanation of this different behaviour can be given based on the data stored in the polycrystal model. In particular, the crystallographic texture and a residual stress field are contained in the statistical distribution of $\tilde{\mathbf{F}}_\kappa$. In a

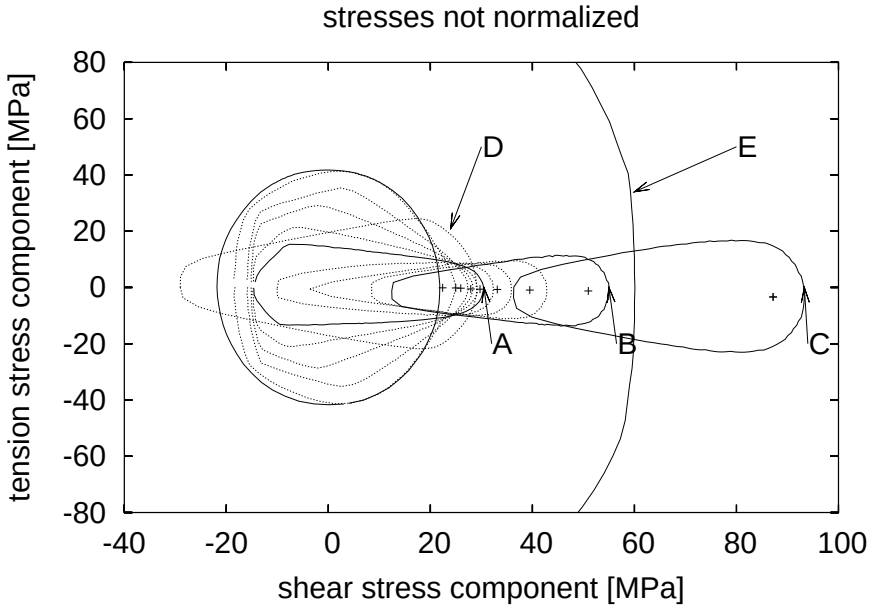

a

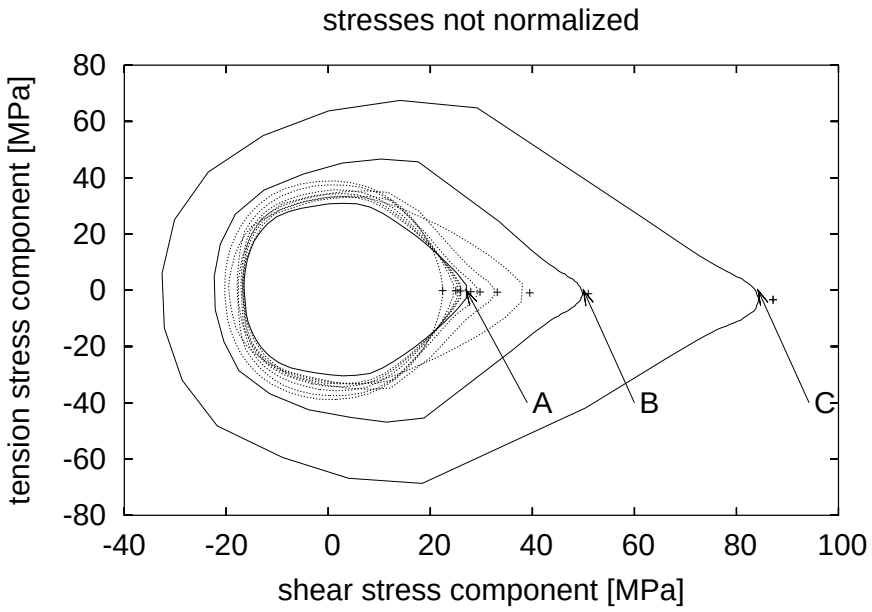

b

Fig. 5.5: Flow potential (a) and dissipation (b) isolines as indicators for subsequent yield surfaces after different tension prestrains

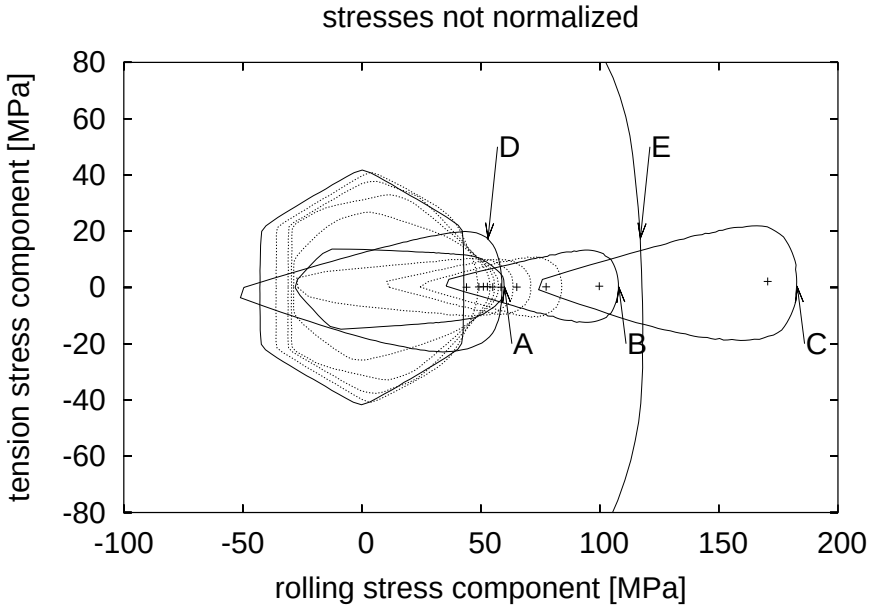

a

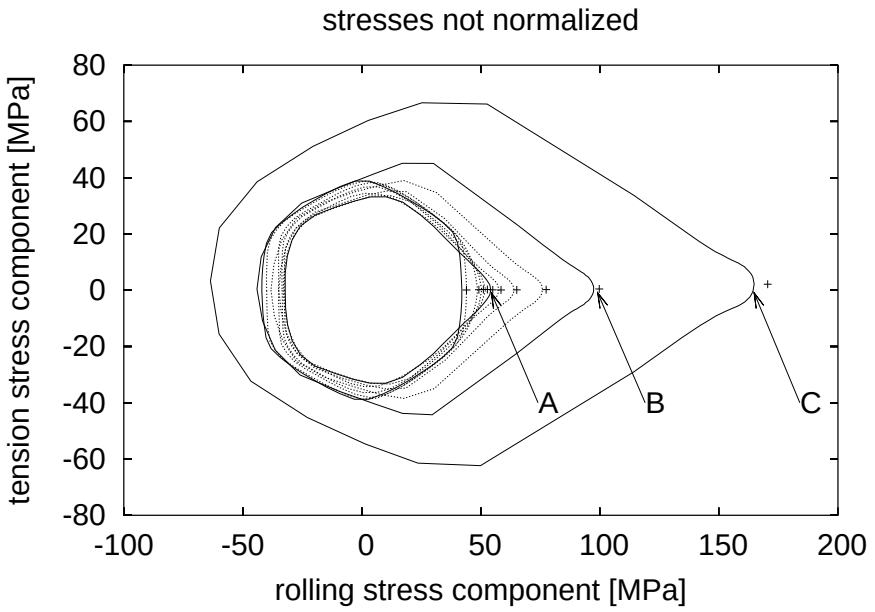

b

Fig. 5.6: Flow potential (a) and dissipation (b) isolines as indicators for subsequent yield surfaces after different tension prestrains

polar decomposition of the elastic transformation

$$\tilde{\mathbf{F}}_\kappa = \tilde{\mathbf{R}}_\kappa \tilde{\mathbf{U}}_\kappa, \tag{5.9}$$

$\tilde{\mathbf{R}}_\kappa$ describes the texture information while in a macroscopically unloaded state, and $\tilde{\mathbf{U}}_\kappa \neq \mathbf{1}$ indicates a residual stress field.

In such a state, by replacing $\tilde{\mathbf{F}}_\kappa$ with $\tilde{\mathbf{R}}_\kappa$, the residual stress field is deleted without changing the texture and the hardening information. Then the isolines of the flow potential were once more computed (Fig. 5.4a, labeled D). For comparison, the elastic transformations $\tilde{\mathbf{F}}$ were reset to the initial ones (Fig. 5.4a, labeled E, large ellipsoid only shown by part.). These are also pure rotations, but this time the early developed texture has been deleted, too. It is obvious that the texture information has substatially more influence on the shape of the isoline than the residual stress field.

This contradicts findings in the literature that attribute the early distortion of yield surface mainly to the residual stress field (Kraska, 1998, Zattarin et al., 2004).

An explanation can be found in the nature of shear processes on crystals. Due to the possible perpetuous lattice rotation, slip systems get active and inactive on a straight deformation path (Schurig and Bertram, 2003). Thus it is possible that a macroscopic reversal of stress does not unload but load a small number of slip systems. In such a case, an elastic domain in a strict sense ceases to exist.

The high exponent n in the definition of the viscous flow potential (4.86) results in large values, if a small number of slip systems exceed their critical stress by a small amount. Thus, the flow potential looses its predictive character for the elastic domain, if reversal of the process would not lead to total unloading as reflected by a value of $\bar{\omega} < 10^{-9}$ which has been shown to be of the order of magnitude of a single active slip system (5.8).

Fig. 5.7 shows the minimum of the flow potential that is eventually reached after different amounts of reversed strain. For shear prestrain, it does not fall below a finite value which depends on the level of prestrain. After the prestrain stage A, the flow potential does not fall below 1.16×10^{-6} (or 0.2% of its value at a straight continuation).

However, a tensile prestrain shows much smaller minima, indicating unloading of all mechanisms.

The dissipation criterion handles such situations by allowing yield on a few slip systems that are then filtered out by the critical threshold. Thus, it is more suitable for such situations.

The sharpening of the outer corner angle reaches further stages earlier in shear and rolling processes than in tension processes. A similar result has been obtained in the stress-strain curves, once more indicating that the equivalent stress/strain are not perfectly suitable for the model.

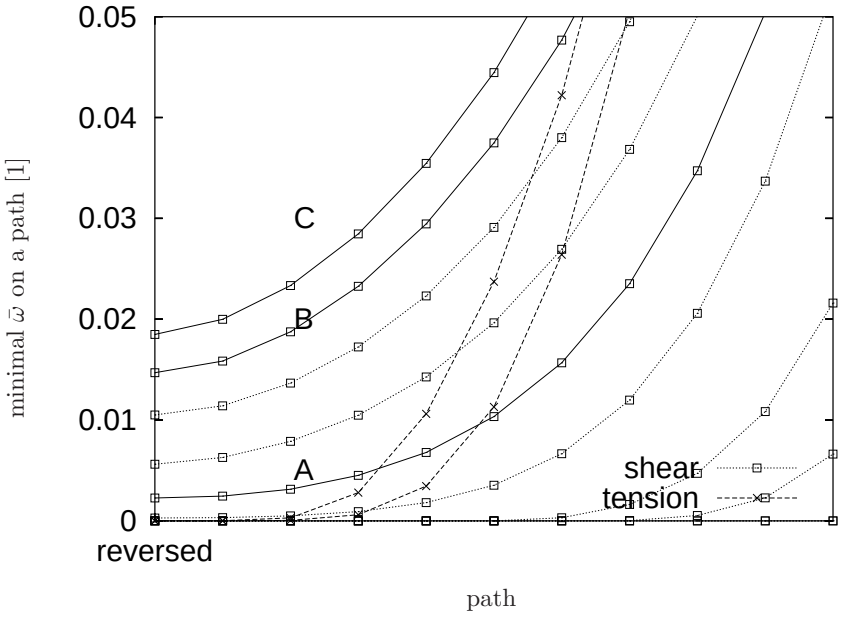

Fig. 5.7: Minima of flow potential on several continuation processes after previous prestrain stages

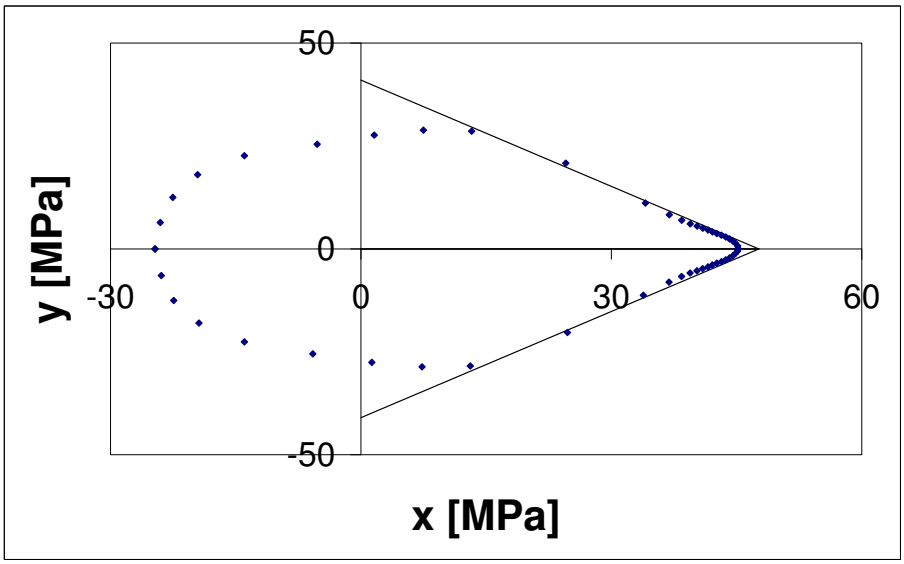

Fig. 5.8: Identification of the corner by linear regression

5.2 Development of the outer corner angle

In vertex models of plasticity, the outer corner angle of the yield vertex is a constitutive parameter of considerable importance (Christoffersen and Hutchinson, 1979, Gotoh, 1985a,b, Petryk and Thermann, 1997). From the isodissipation lines, it can be identified using a linear regression analysis in a twodimensional section of the stress space.

We use plot sheet coordinates in the non-normalized basis given by the process directions $\mathbf{A}_i$ of Tab. 5.3. $x = \mathbf{T} \cdot \mathbf{A}_x$ and $y = \mathbf{T} \cdot \mathbf{A}_y$. The resulting linear equations, $y = m_i\, x + b_i, \quad i = 1, 2$ can be retransferred to the deviatoric Cauchy stress space by

$$\mathbf{T}(x) = x \left(\frac{\mathbf{A}_x}{\mathbf{A}_x \cdot \mathbf{A}_x} + m_i \frac{\mathbf{A}_y}{\mathbf{A}_y \cdot \mathbf{A}_y} \right) + b_i \frac{\mathbf{A}_y}{\mathbf{A}_y \cdot \mathbf{A}_y} \tag{5.10}$$

Accordingly, the direction of these lines is given by

$$\mathbf{B}_i = \frac{\mathbf{A}_x}{\mathbf{A}_x \cdot \mathbf{A}_x} + m_i \frac{\mathbf{A}_y}{\mathbf{A}_y \cdot \mathbf{A}_y} \tag{5.11}$$

and the outer corner angle θ^c (Fig. 5.9) can be calculated from their full contraction,

$$\theta^c = \pi - \frac{1}{2} \arccos \frac{\mathbf{B}_1}{\|\mathbf{B}_1\|} \cdot \frac{\mathbf{B}_2}{\|\mathbf{B}_2\|}. \tag{5.12}$$

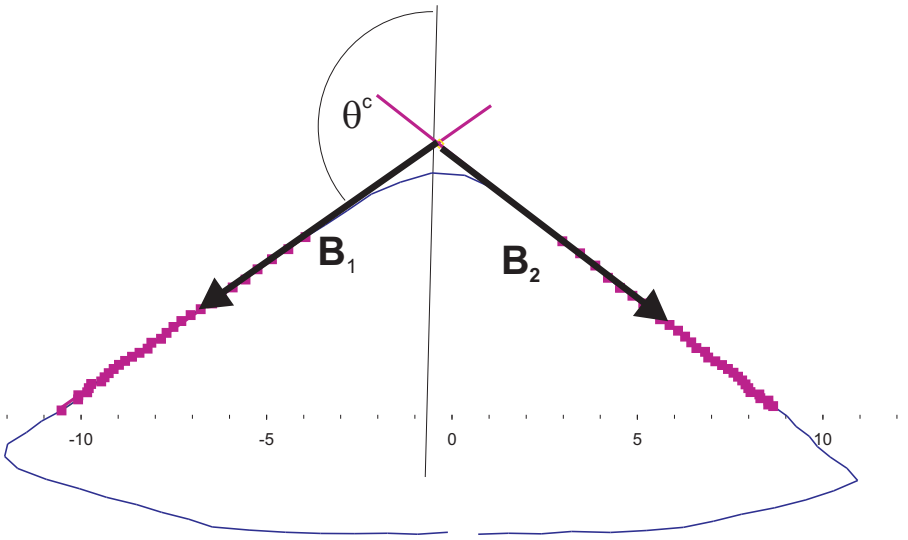

Fig. 5.9: Identification of corner angle

The intersection of the two regression lines is at

$$x_c = \frac{b_2 - b_1}{m_1 - m_2}. \tag{5.13}$$

Using (5.10), the according stress point $\mathbf{T}^c$ can be computed. It is regarded as the idealized vertex if no rounding were present.

$$\mathbf{T}^c = \frac{b_2 - b_1}{m_1 - m_2} \frac{\mathbf{A}_x}{\mathbf{A}_x \cdot \mathbf{A}_x} + \frac{m_1 b_2 - m_2 b_1}{m_1 - m_2} \frac{\mathbf{A}_y}{\mathbf{A}_y \cdot \mathbf{A}_y} \tag{5.14}$$

The development of θ^c for different prestrain processes and both criteria has been plotted in Fig. 5.10. Due to the above explained reasons, the results for the flow potential are not trustworthy for strains beyond stage A. The results obtained with the dissipation criterion in Fig. 5.10b start from a smooth initial surface ($\theta^c = 90°$). After a small amount of strain at stage A ($\epsilon_{\log} = 10^{-3}$) the vertex has developed.

From the flow potential, it was not possible to determine the corner angle for very small prestrains. The reason is that the strong rounding makes a linear regression inaccurate.

Thus the linear regression confirms the qualitative results of the isoline plots Fig. 5.4–5.6. At that strain level a second stage of sublinear growth of the outer corner angle is initiated. However, a saturation is not found.

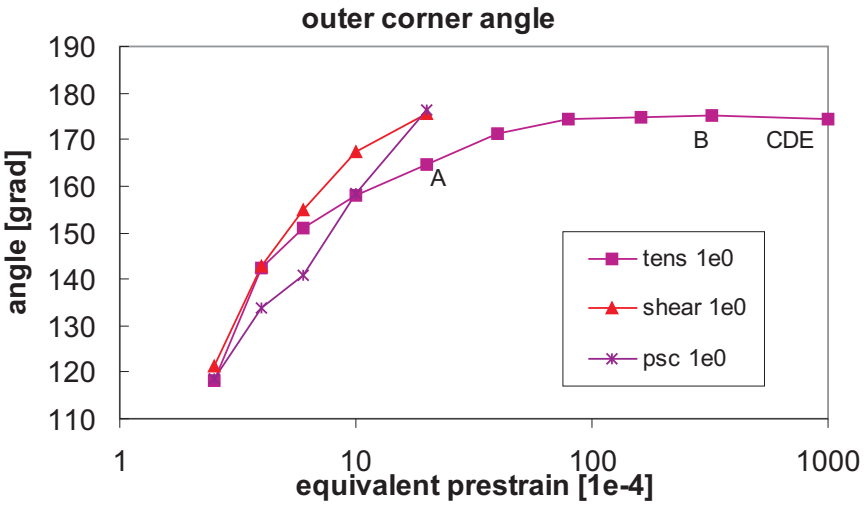

a

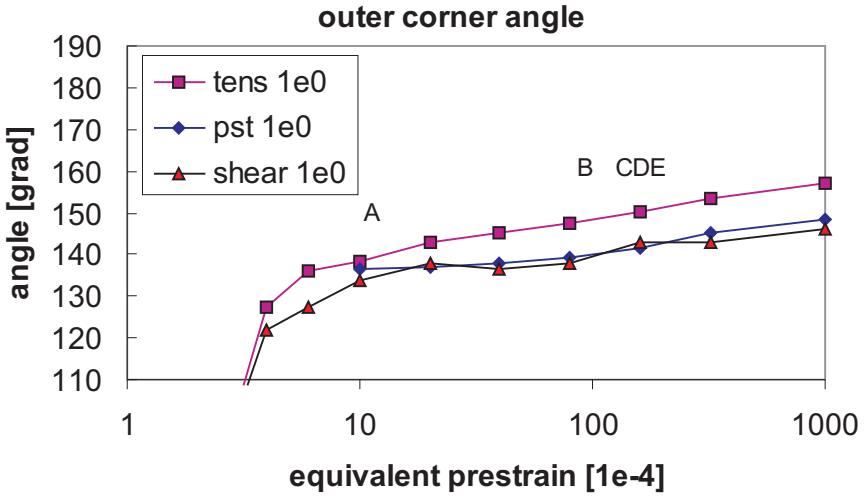

b

Fig. 5.10: Development of the outer corner angle a) in flow potential b) in dissipation

5.3 Complex strain processes

5.3.1 Shear after unloaded tension

A tension prestrain up to stage A (see Tab. 5.3) was followed by an elastic unloading process. From that state, the same program as prescribed above for shear has been performed as a secondary path. Fig. 5.11 shows the resulting potential and dissipation isolines together with the stress path obtained by this sequence.

Near the stress path, a secondary vertex can be found. While it is developing, the prior shape including the primary vertex is dissolved.

The outer corner angle of the secondary vertex has been obtained for a secondary shear of stage A as 135.5°. In comparison, shear without prior tension process at stage A reaches 138.0°.

5.3.2 Shear immediately after tension

Without intermediate unloading, after tension prestrain up to stage A, strain was continued by shear processes. Fig. 5.12 shows the resulting potential and dissipation isolines together with the stress path obtained by this sequence. Here, the vertex is not removed but turns along with the actual stress point. The prior shape of the primary vertex has completely transformed (Fig. 5.13). An outer corner angle of 137.7° is finally reached at stage A.

The irregular shape makes a regression analysis difficult in the first stages of secondary corner development. Thus, based on judgement of the outer corner angle reached after additional equivalent accumulated logarithmic strain of $\epsilon_{\log} = 0.001$, the secondary vertex develops like the primary one.

5.4 Consequences for a macroscopic vertex model

The analysis of subsequent yield surfaces is possible using the surrogate of isodissipation surfaces in stress space Kraska (1998), Kuwabara et al. (2000).

Using a critical threshold that is equivalent to a plastic offset strain of approximately 2×10^{-5}, the development of a corner near the actual stress point can be detected. This corner is well developed at strains of 10^{-3}, i.e. at the typical technical definition of the yield point.

After changing the strain path, a secondary vertex develops. Regardless whether unloading takes place at the point of strain change, it develops to similar sharpness as the primary vertex. The vertex tip point in the direction of the last prestress point in straight as well as in complex processes and has an approximately conical shape.

For that reason it is justified to speak about a traveling vertex in polycrystal plasticity, i.e. a vertex that is always immediately present at the actual stress point on the yield surface.

This assumption has been made in the literature on the vertex effect, mainly

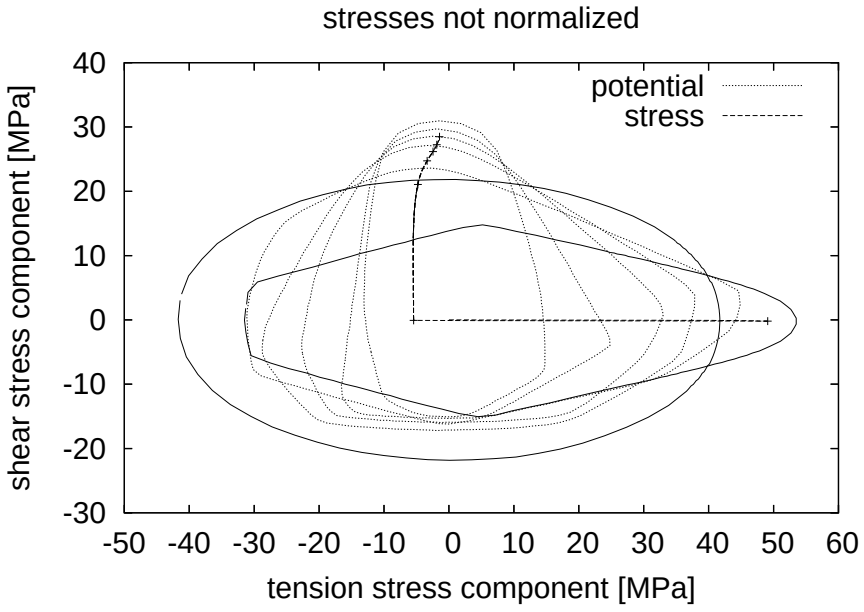

a

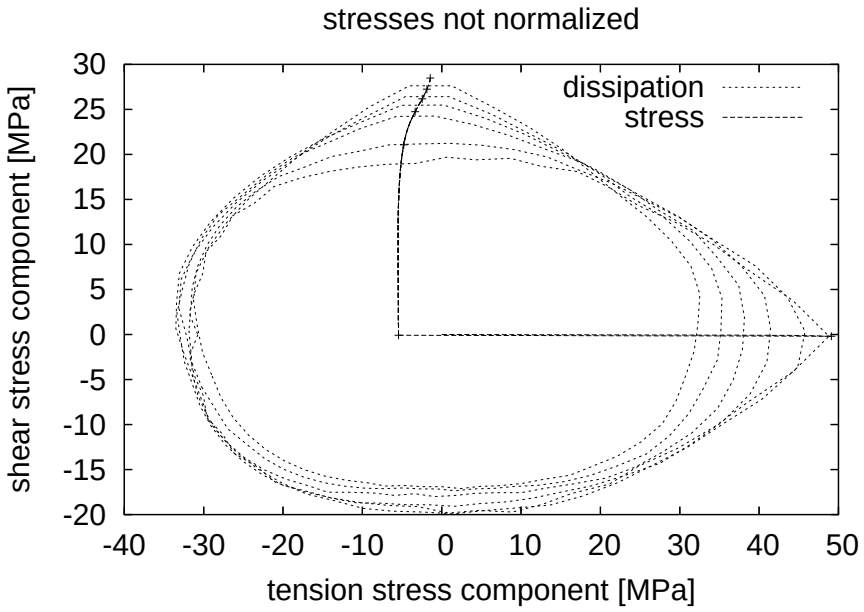

b

Fig. 5.11: Development of a secondary vertex with transient unloading

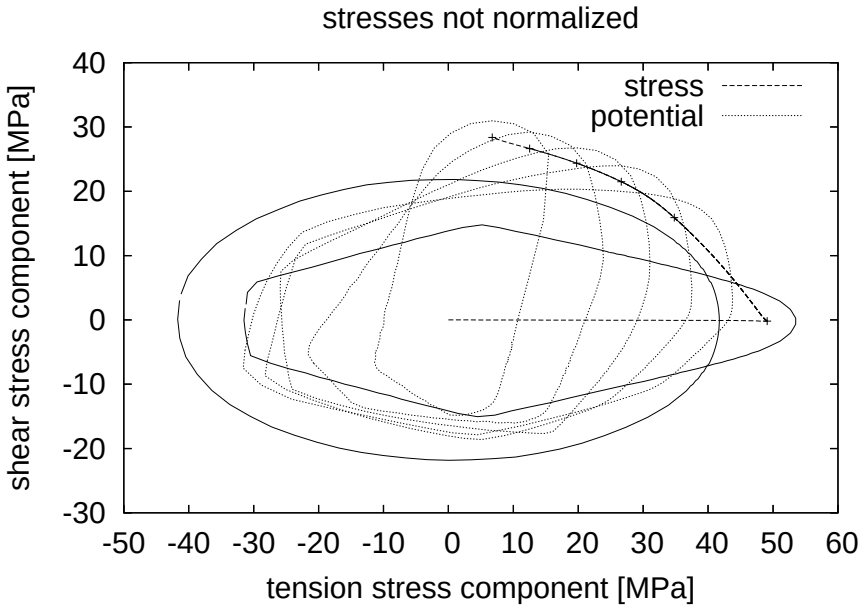

a

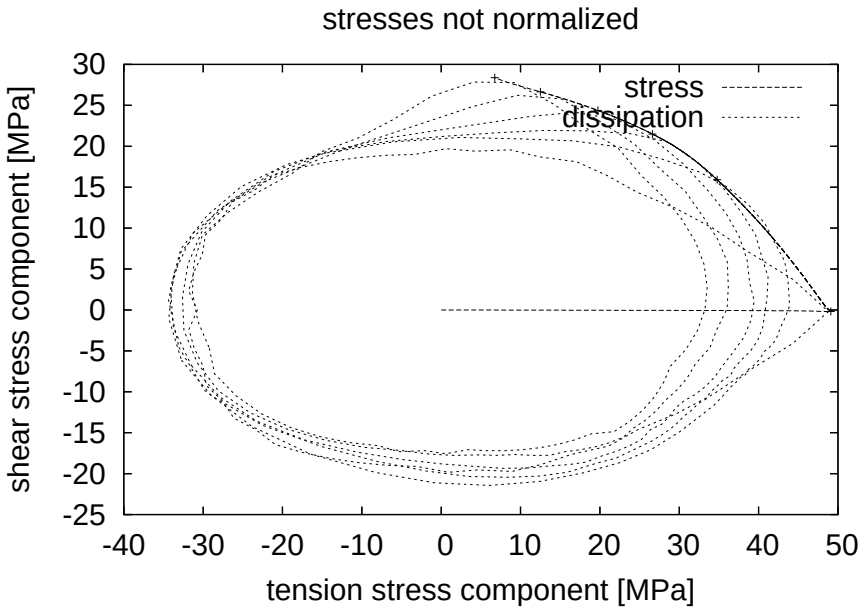

b

Fig. 5.12: Development of a secondary vertex without transient unloading

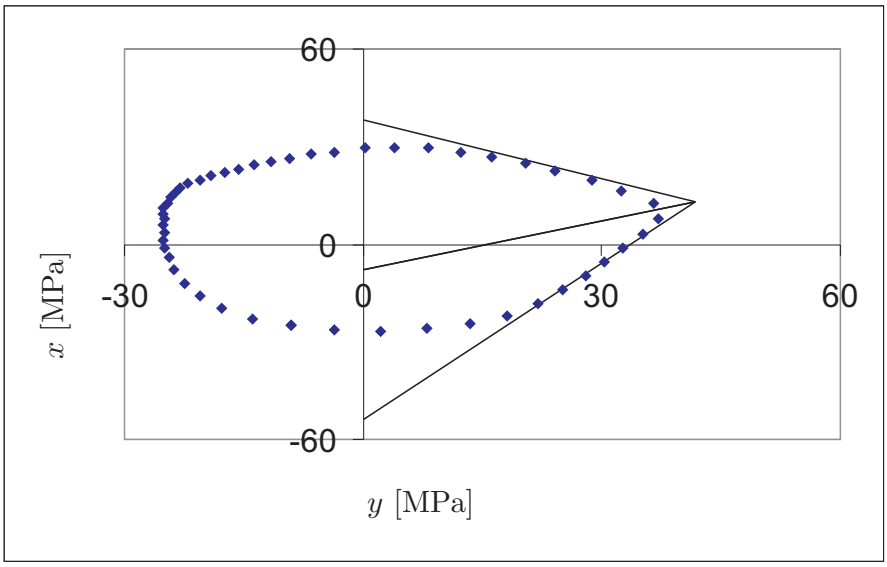

Fig. 5.13: Linear regression to identify secondary vertex in the last step of Fig. 5.12b. Note that axes have been interchanged.

based on evidence from theoretical considerations. The preceeding investigations provide a simulation-based foundation.

For the formulation of a flow rule incorporating the vertex effect, it allows for the following simplifications for a first approximation:

- The direction of prestress characterizes the vertex
- A flow rule is rotationally symmetric with regard to this direction.
- It can be used for proportional and non-proportional processes simultaneously.

6. A MACROSCOPIC VERTEX MODEL

Section Overview
A macroscopic theory of plasticity based on the theoretical considerations of Chapter 4.3 and the simulation results of Chapter 5 is proposed. It is an extension of the classical J_2 flow theory which is contained as a special case.
Parameters are estimated from additional polycrystal simulations and a numerical scheme for its implementation in numerical applications is proposed.

6.1 Process dependence of dissipation

As shown in Section 4.5, Fig. 4.2, the vertex effect in a macroscopic flow rule in the presence of a large number of microscopic mechanisms can be modeled by the following procedure:

- The flow rule additionally depends on the direction in which a stress process would be continued straight, which will be referred to as the *natural direction* $\tilde{\mathbf{M}}_{\mathrm{N}}$.
- A scalar loading parameter α models the deviation from this direction. In this manner the rate-independence is maintained.
- In the subspace spanned by the natural direction and the direction of Mandel's stress rate at fixed plastic state variables (the loading direction) $\tilde{\mathbf{M}}_{\mathrm{N}}$ and $\tilde{\mathbf{M}}_{\mathrm{T}}$ with $\tilde{\mathbf{M}}_{\mathrm{N}} \cdot \tilde{\mathbf{M}}_{\mathrm{T}} = 0$ can be used as a basis. $\tilde{\mathbf{M}}_{\mathrm{T}}$ is called the tangential direction.
- For convenience, we use the direction cosine as loading parameter which results in

$$\begin{aligned} \tilde{\mathbf{M}} &= \frac{\left.\frac{\mathrm{d}}{\mathrm{d}t}\,\tilde{\mathbf{C}}\tilde{\mathbf{S}}\right|_{\mathbf{P},z=\mathrm{const}}}{\left\|\left.\frac{\mathrm{d}}{\mathrm{d}t}\,\tilde{\mathbf{C}}\tilde{\mathbf{S}}\right|_{\mathbf{P},z=\mathrm{const}}\right\|} = \alpha\tilde{\mathbf{M}}_{\mathrm{N}} + \sqrt{1-\alpha^2}\tilde{\mathbf{M}}_{\mathrm{T}}, \\ \alpha &= \tilde{\mathbf{M}}_{\mathrm{N}} \cdot \tilde{\mathbf{M}}. \end{aligned} \tag{6.1}$$

In a microscopic model the vertex effect affects not only the direction of the plastic flow but also the size of the plastic zone resp. the volume fraction of that grains that are in a loading state. The reason is that the active set $\mathcal{A}$ is a

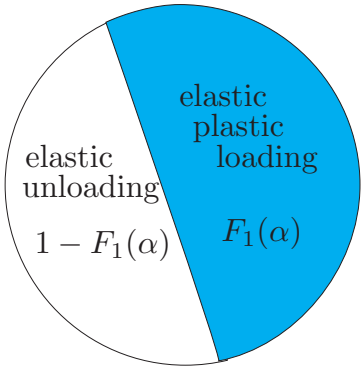

Fig. 6.1: Unloading on kinked paths

function of the process continuation through the loading condition (see Section 4.5).

Assuming that some grains or part of them return to the elastic state if all slip systems get inactive the according volume fractions are F_1 for the plastic and $1 - F_1$ for the elastic zone (Fig. 6.1).

The macroscopic internal stress power can be obtained from the zone averages of the zones under Hill's averaging theorem (Hill, 1952, Krawietz, 1986, Petryk, 1998), with the Kirchhoff stress $\boldsymbol{\tau}$,

$$\bar{\boldsymbol{\tau}} \cdot \bar{\mathbf{D}} = F_1 \boldsymbol{\tau}_1 \cdot \mathbf{D}_1 + (1 - F_1) \boldsymbol{\tau}_2 \cdot \mathbf{D}_2, \tag{6.2}$$

which by (4.36) can be splitted in elastic and plastic parts,

$$\bar{\boldsymbol{\tau}} \cdot \bar{\mathbf{D}} = F_1 \left(\boldsymbol{\tau}_1 \cdot \tilde{\mathbf{D}}_1 - (\tilde{\mathbf{C}}\tilde{\mathbf{S}})_1 \cdot (\mathbf{P}^{-1}\dot{\mathbf{P}})_1 \right) + (1 - F_1) \boldsymbol{\tau}_2 \cdot \tilde{\mathbf{D}}_2. \tag{6.3}$$

Here, elastic behaviour was assumed in zone 2, while zone 1 is elastic-plastic, and the according flow rule has to be inserted for $(\mathbf{P}^{-1}\dot{\mathbf{P}})_1$.

A simple assumption that fulfills Hill's Lemma is the Reuss hypothesis:

$$\boldsymbol{\tau}_1 = \boldsymbol{\tau}_2 = \bar{\boldsymbol{\tau}}. \tag{6.4}$$

Modeling the progressive unloading zone due to kinked process continuations, the assumption that both zones start from the same state, is natural. Taking the time derivative of (6.4),

$$\begin{aligned} \dot{\boldsymbol{\tau}}_i &= \tilde{\mathbf{L}}_i \boldsymbol{\tau}_i + \boldsymbol{\tau}_i \tilde{\mathbf{L}}_i^\top + \tilde{\mathbf{F}}_i \dot{\tilde{\mathbf{S}}}_i \tilde{\mathbf{F}}_i^\top \\ &= \tilde{\mathbf{L}}_i \boldsymbol{\tau}_i + \boldsymbol{\tau}_i \tilde{\mathbf{L}}_i^\top + \tilde{\mathbf{F}}_i \star \tilde{\mathbb{C}}[\tilde{\mathbf{D}}_i] \\ &= \left[\mathbb{I} \boldsymbol{\tau}_i + \boldsymbol{\tau}_i \mathbb{T} + \tilde{\mathbf{F}}_i \star \tilde{\mathbb{C}} \circ \frac{1}{2} (\mathbb{I} + \mathbb{T}) \right] [\tilde{\mathbf{L}}_i] \end{aligned} \tag{6.5}$$

one finds the incremental moduli in this equation only depending on state variables. From the equality of the rates (and not the appropriate objective rates of $(4.15)_3$), the elastic rates of stretching are equal[1]

$$\tilde{\mathbf{D}}_1 = \tilde{\mathbf{D}}_2 = \tilde{\mathbf{D}}, \tag{6.6}$$

by which we obtain

$$\bar{\boldsymbol{\tau}} \cdot \bar{\mathbf{D}} = \bar{\boldsymbol{\tau}} \cdot \tilde{\mathbf{D}} - F_1 \tilde{\mathbf{C}}\tilde{\mathbf{S}} \cdot (\mathbf{P}^{-1}\dot{\mathbf{P}})_1. \tag{6.7}$$

A comparison with the macroscopic version (4.36) yields

$$\mathbf{P}^{-1}\dot{\mathbf{P}} = F_1 \, (\mathbf{P}^{-1}\dot{\mathbf{P}})_1. \tag{6.8}$$

We assume a constitutive transition function

$$F_1 : \, [-1, 1] \to [0, 1], \alpha \mapsto F_1(\alpha). \tag{6.9}$$

This derivation is not a strict homogenization approach which would necessarily be based on distinct state variables for the zones and an equation of evolution for the volume fraction in the finite duration of a process. Instead, the present model accounts only for the influence of the changing direction of process on the dissipation by partial unloading. This dissipation modell is additional to the history-dependence through the flow rule $(\mathbf{P}^{-1}\dot{\mathbf{P}})_1$. In contrast, the classical J_2 flow theory has only the latter feature.

For this purpose the dissipation model shall prove valuable for an improved description of plastic processes on nonproportional process paths in spite of its simplified nature.

6.2 Process dependence of the flow rule

.

In Section 4.5, a regularization of the multi-mode approach separately for each constitutive cone lead to a process-dependence of the plastic potential via the process dependence of the active set.

For many mechanisms like in a polycrystal, this behaviour can be modeled by a smooth plastic potential for each constitutive cone, i.e. in the limit for each process continuation.

Accordingly, a nonlinear process-dependence of the plastic potential can be stated, which is used to enhance the single-mechanism plasticity contained in the results of Section 4.3. The variables that describe the process continuation, i.e. $\tilde{\mathbf{M}}_{\mathrm{N}}$, $\tilde{\mathbf{M}}_{\mathrm{T}}$, and α are assumed to be given at any instance.

Starting with a (given) macroscopic yield criterion that describes the elastic domain (4.41),

$$\Phi(\tilde{\mathbf{C}}\tilde{\mathbf{S}}', g) \leq 0, \tag{6.10}$$

[1] Of course, this model is a rough one. The simplification is the lack of individual state variables for the zones.

an associated flow rule results in $(4.46)_1$,

$$\mathbf{P}^{-1}\dot{\mathbf{P}} = \boldsymbol{\Pi}_{\mathrm{N}} = -\lambda_{\mathrm{N}}\partial_{\tilde{\mathbf{C}}\tilde{\mathbf{S}}}\Phi. \tag{6.11}$$

(6.11) is not process-dependent and lacks a flow component parallel to the elastic domain as existent in the multi-mode theory (see Section 4.5.4). An enhancement by an additional flow component can be derived from

$$\begin{aligned} \boldsymbol{\Pi}_{\mathrm{T}} &= -\lambda_{\mathrm{T}}\partial_{\tilde{\mathbf{C}}\tilde{\mathbf{S}}}\Pi_{\mathrm{T}}, \\ \Pi_{\mathrm{T}} &= \tilde{\mathbf{M}}_{\mathrm{T}} \cdot \tilde{\mathbf{C}}\tilde{\mathbf{S}}. \end{aligned} \tag{6.12}$$

The two parts can be summed up to a single plastic potential Π,

$$\mathbf{P}^{-1}\dot{\mathbf{P}} = -\lambda\,\partial_{\tilde{\mathbf{C}}\tilde{\mathbf{S}}}\Pi, \tag{6.13}$$

$$\Pi = \frac{\lambda_{\mathrm{N}}}{\lambda}\Phi + \frac{\lambda_{\mathrm{T}}}{\lambda}\Pi_{\mathrm{T}}. \tag{6.14}$$

Π is a function of $(\mathbf{F}, z, \tilde{\mathbf{M}}_{\mathrm{N}}, \tilde{\mathbf{M}})$. This includes the crucial influence of $\alpha = \tilde{\mathbf{M}}_{\mathrm{N}} \cdot \tilde{\mathbf{M}}$. A second transition function,

$$F:\ [-1,1] \to [0,1], \alpha \mapsto F(\alpha) \tag{6.15}$$

is used to model the exact dependence on non-straight processes through the ratios

$$\begin{aligned} \frac{\lambda_{\mathrm{N}}}{\lambda} &= F(\alpha), \\ \frac{\lambda_{\mathrm{T}}}{\lambda} &= 1 - F(\alpha). \end{aligned} \tag{6.16}$$

Accordingly, we arrive at

$$\begin{aligned} \mathbf{P}^{-1}\dot{\mathbf{P}} &= -\lambda\,\partial_{\tilde{\mathbf{C}}\tilde{\mathbf{S}}}\Pi \\ \hat{\Pi}(\tilde{\mathbf{C}}\tilde{\mathbf{S}}, g, \tilde{\mathbf{M}}_{\mathrm{N}}, \tilde{\mathbf{M}}) &= F(\alpha)\Phi + (1 - F(\alpha))\tilde{\mathbf{M}}_{\mathrm{T}} \cdot (\tilde{\mathbf{C}}\tilde{\mathbf{S}})'. \end{aligned} \tag{6.17}$$

Here, $(\cdot)'$ denotes the deviator. It is sufficient because $\tilde{\mathbf{M}}_{\mathrm{T}}$ is deviatoric.

6.2.1 The associated elastic domain

Following the traveling vertex assumption of Section 5.4 and the results of Section 4.5.4, we identify the natural direction $\tilde{\mathbf{M}}_{\mathrm{N}}$ with the direction of the normal of the elastic domain,

$$\tilde{\mathbf{M}}_{\mathrm{N}} = \partial_{\tilde{\mathbf{C}}\tilde{\mathbf{S}}}\Phi. \tag{6.18}$$

Hence, on any radial stress path we find at $\Phi = 0$ a value of the plastic potential of

$$\Pi|_{\Phi=0} = (1 - F(\alpha))\,\tilde{\mathbf{M}}_{\mathrm{T}} \cdot (\tilde{\mathbf{C}}\tilde{\mathbf{S}})'. \tag{6.19}$$

Accordingly, the plastic potential can also be used as an indicator for the elastic domain if

$$\tilde{\mathbf{M}}_{\mathrm{T}} \cdot (\tilde{\mathbf{C}}\tilde{\mathbf{S}})' = 0. \tag{6.20}$$

This is the case if the elastic domain is given by the Huber-von-Mises criterion,

$$\Phi(\tilde{\mathbf{C}}\tilde{\mathbf{S}}, g) = \sqrt{\frac{3}{2}(\tilde{\mathbf{C}}\tilde{\mathbf{S}})' \cdot (\tilde{\mathbf{C}}\tilde{\mathbf{S}})'} - g. \tag{6.21}$$

In this case

$$\tilde{\mathbf{M}}_{\mathrm{N}} = \frac{(\tilde{\mathbf{C}}\tilde{\mathbf{S}})'}{\|(\tilde{\mathbf{C}}\tilde{\mathbf{S}})'\|} \tag{6.22}$$

and, thus, (6.20) is fulfilled. The direction of plastic flow is finally

$$\partial_{\tilde{\mathbf{C}}\tilde{\mathbf{S}}}\Pi = F(\alpha)\frac{(\tilde{\mathbf{C}}\tilde{\mathbf{S}})'}{\|(\tilde{\mathbf{C}}\tilde{\mathbf{S}})'\|} + (1 - F(\alpha))\tilde{\mathbf{M}}_{\mathrm{T}}. \tag{6.23}$$

6.2.2 The hardening rule

For the hardening variables we introduce the equation of evolution $(4.46)_2$ in a suitable way:

$$\begin{aligned} g &= \hat{g}(z) \\ \dot{z} &= -\lambda\partial_g\Pi. \end{aligned} \tag{6.24}$$

6.2.3 Exploitation of the condition of consistency

This result can be utilized for the formulation of the condition of consistency. For fixed process continuation parameters (4.56) can be applied accordingly

$$\frac{\mathrm{d}}{\mathrm{d}t}\Pi = F(\alpha)\,\frac{\mathrm{d}}{\mathrm{d}t}\Phi(\tilde{\mathbf{C}}\tilde{\mathbf{S}}, g) = 0 \tag{6.25}$$

allowing for a standard way of determination of the single plastic multiplier with all consequences that shall be exploited in the sequel.

6.2.4 Thermodynamic consistency

In the formulation of the second law, the Clausius-Planck-Equation (3.31) has to be fulfilled.

Insertion of the specific stress power (4.36) and the flow rule (6.8), we obtain

$$\begin{aligned} \rho\dot{\psi} &\leq \tilde{\mathbf{C}}\tilde{\mathbf{S}} \cdot \left[\tilde{\mathbf{F}}^{-1}\dot{\tilde{\mathbf{F}}} - F_1(\alpha)\left(F(\alpha)\tilde{\mathbf{M}}_{\mathrm{N}} + (1 - F(\alpha))\tilde{\mathbf{M}}_{\mathrm{T}}\right)\right] \\ &= \tilde{\mathbf{C}}\tilde{\mathbf{S}} \cdot \left[\tilde{\mathbf{F}}^{-1}\dot{\tilde{\mathbf{F}}} - F_1(\alpha)F(\alpha)\tilde{\mathbf{M}}_{\mathrm{N}}\right]. \end{aligned} \tag{6.26}$$

The second expression is a consequence of the choice of the natural direction according to (6.20).

For $0 < (F(\alpha)F_1(\alpha)) \leq 1$, the right hand side of (6.26) is increased in comparison to the same equation if the J_2 flow theory is adopted.

Accordingly, the second law is fulfilled at least in all cases where it is by the J_2 flow theory.

$\mathbf{F} = \mathbf{u} \otimes \nabla_0$	(3.3)	Deformation gradient
$\tilde{\mathbf{F}} = \mathbf{F}\mathbf{P}$	(4.28)	Elastic transformation
$\tilde{\mathbf{C}} = \tilde{\mathbf{F}}^\top \tilde{\mathbf{F}}$	(4.30)	Elastic right Cauchy-Green tensor
$\tilde{\mathbf{E}} = \frac{1}{2}(\tilde{\mathbf{C}} - \mathbf{1})$	(3.13)	Elastic Green's Tensor
$\tilde{\mathbf{S}} = \frac{E}{1+\nu}\left[\tilde{\mathbf{E}} + \frac{\nu}{1-2\nu}\tilde{\mathbf{E}} \cdot \mathbf{1} \otimes \mathbf{1}\right]$		Isotropic elastic law
$\Phi(\tilde{\mathbf{C}}\tilde{\mathbf{S}}, g) = \sqrt{\frac{3}{2}(\tilde{\mathbf{C}}\tilde{\mathbf{S}})' \cdot (\tilde{\mathbf{C}}\tilde{\mathbf{S}})'} - g$	(6.21)	Huber-von-Mises criterion
$0 = \Pi(\tilde{\mathbf{C}}\tilde{\mathbf{S}}, g, \mathbf{M}_0)$ $= F(\alpha)\Phi + (1 - F(\alpha))\mathbf{M}_\mathrm{T} \cdot (\tilde{\mathbf{C}}\tilde{\mathbf{S}})'$	$(6.17)_2$, (6.20)	Plastic Potential and Consistency
$\mathbf{P}^{-1}\dot{\mathbf{P}} = -\lambda\, F_1(\alpha)\partial_{\tilde{\mathbf{C}}\tilde{\mathbf{S}}}\Pi$	$(6.17)_1$, (6.8)	Flow rule corrected for plastic zone
$g = \hat{g}(z)$	$(6.24)_1$	Hardening curve
$\dot{z} = -\lambda\, \partial_g \Pi$	$(6.24)_2$	Hardening rule
$\mathbf{M} = \frac{\frac{\mathrm{d}}{\mathrm{d}t}(\tilde{\mathbf{C}}\tilde{\mathbf{S}})'\big\vert_{\mathbf{P},z=\mathrm{const}}}{\left\|\frac{\mathrm{d}}{\mathrm{d}t}(\tilde{\mathbf{C}}\tilde{\mathbf{S}})'\big\vert_{\mathbf{P},z=\mathrm{const}}\right\|}$	(4.97)	Loading direction
$\mathbf{M}_\mathrm{N} = \frac{(\tilde{\mathbf{C}}\tilde{\mathbf{S}})'}{\|(\tilde{\mathbf{C}}\tilde{\mathbf{S}})'\|}$	(6.18)	Natural direction
$\alpha = \mathbf{M} \cdot \mathbf{M}_\mathrm{T}$	(4.102)	Loading parameter
$\mathbf{M}_\mathrm{T} = \frac{\mathbf{M} - \alpha\mathbf{M}_\mathrm{N}}{\sqrt{1-\alpha^2}}$	(4.101)	Tangential direction

Tab. 6.1: Set of equations for the vertex model

6.3 Incremental elastic-plastic law

6.3.1 General formulation

Exploiting the indicator property of the plastic potential Π established in Section 6.2.1, we set $\phi_\alpha = \Pi$ and procede as in Section 4.3.5 to obtain a rate law for the rate of the second Piola-Kirchhoff stress,

$$\dot{\mathbf{S}} = \mathbf{P} \star \tilde{\mathbb{K}}[\dot{\mathbf{E}}]. \tag{6.27}$$

The incremental moduli tensor is

$$\begin{aligned}
\tilde{\mathbb{K}} &= \tilde{\mathbb{C}} - g_{11}^{-1}\tilde{\mathbf{A}} \otimes \tilde{\mathbf{A}}, \\
g_{11} &= (\tilde{\mathbf{A}} \cdot \tilde{\mathbf{C}}\, \partial_{\tilde{\mathbf{C}}\tilde{\mathbf{S}}}\Pi - a\partial_g\Pi)/F_1(\alpha) \\
\tilde{\mathbf{A}} &= 2\mathrm{sym}(\partial_{\tilde{\mathbf{C}}\tilde{\mathbf{S}}}\Pi\, \tilde{\mathbf{S}}) + \tilde{\mathbb{C}}[\tilde{\mathbf{C}}\partial_{\tilde{\mathbf{C}}\tilde{\mathbf{S}}}\Pi] \\
&= (2\mathbb{I}^s\tilde{\mathbf{S}} + \tilde{\mathbb{C}} \circ \tilde{\mathbf{C}}\mathbb{I})[F(\alpha)\tilde{\mathbf{M}}_\mathrm{N} + (1 - F(\alpha))\tilde{\mathbf{M}}_\mathrm{T}] \\
a &= \partial_g\Pi\frac{\partial g}{\partial z}.
\end{aligned} \tag{6.28}$$

For small elastic strain, (6.28) can be simplified (Schurig and Bertram, 2005),

$$\begin{aligned}\tilde{\mathbb{K}} &= \tilde{\mathbb{C}} - F_1(\alpha)\frac{\mathbb{C}[F(\alpha)\tilde{\mathbf{M}}_{\mathrm{N}}+(1-F(\alpha))\tilde{\mathbf{M}}_{\mathrm{T}}]\otimes\mathbb{C}[F(\alpha)\tilde{\mathbf{M}}_{\mathrm{N}}+(1-F(\alpha))\tilde{\mathbf{M}}_{\mathrm{T}}]}{\left(F(\alpha)\tilde{\mathbf{M}}_{\mathrm{N}}+(1-F(\alpha))\tilde{\mathbf{M}}_{\mathrm{T}}\right)\cdot\mathbb{C}[\left(F(\alpha)\tilde{\mathbf{M}}_{\mathrm{N}}+(1-F(\alpha))\tilde{\mathbf{M}}_{\mathrm{T}}\right)]+F^2(\alpha)\frac{\partial g}{\partial z}} \\ &= 2G(\mathbb{I}^s + \tfrac{\nu}{1-2\nu}\mathbf{1}\otimes\mathbf{1}) \\ &\quad - F_1(\alpha)\frac{4G^2\left(F(\alpha)\tilde{\mathbf{M}}_{\mathrm{N}}+(1-F(\alpha))\tilde{\mathbf{M}}_{\mathrm{T}}\right)\otimes\left(F(\alpha)\tilde{\mathbf{M}}_{\mathrm{N}}+(1-F(\alpha))\tilde{\mathbf{M}}_{\mathrm{T}}\right)}{2G(F(\alpha)^2+(1-F(\alpha))^2)+F^2(\alpha)\frac{\partial g}{\partial z}},\end{aligned} \tag{6.29}$$

where the last expression is valid for isotropic elasticity.

The existence of a single plastic potential that is also used as a yield criterion assures the symmetry of the incremental moduli tensor. Accordingly, a rate potential exists,

$$\begin{aligned}\mathcal{U} &= \frac{1}{2}\dot{\mathbf{E}}\cdot\mathbb{K}[\dot{\mathbf{E}}], \\ \dot{\mathbf{S}} &= \partial_{\dot{\mathbf{E}}}\mathcal{U}, \\ \mathbb{K} &= \frac{\partial^2\mathcal{U}}{\partial\dot{\mathbf{E}}\,\partial\dot{\mathbf{E}}}.\end{aligned} \tag{6.30}$$

For other measures of stress, (4.69) can be applied to obtain the according equations.

The incremental moduli as well as the rate potential depend in a nonlinear manner on α. This allows for modelling a smooth transition from total loading ($\alpha = 1$) to total unloading as suggested by Hill (1967).

6.3.2 Plain stress formulation

For twodimensional application like plates and shells (see Section 7), the plane stress moduli can be obtained using the constraint

$$\mathbf{e}_z\cdot\dot{\mathbf{S}}\mathbf{e}_z = 0. \tag{6.31}$$

The according twodimensional incremental moduli tensor can be obtained as

$$\tilde{\mathbb{K}}_2 = \tilde{\mathbb{K}} - \frac{\tilde{\mathbb{K}}[\mathbf{e}_z\otimes\mathbf{e}_z]\otimes\tilde{\mathbb{K}}[\mathbf{e}_z\otimes\mathbf{e}_z]}{\mathbf{e}_z\otimes\mathbf{e}_z\cdot\tilde{\mathbb{K}}[\mathbf{e}_z\otimes\mathbf{e}_z]}. \tag{6.32}$$

For further use we define

$$\begin{aligned}\mathrm{K}_{ii}(\mathbf{X}) &= \mathbf{X}\cdot\tilde{\mathbb{K}}_2[\mathbf{X}] \\ &= \mathbf{X}\cdot\tilde{\mathbb{C}}[\mathbf{X}] - \frac{(\mathbf{X}\cdot\tilde{\mathbf{A}})^2}{x} - \frac{\left(\mathbf{X}\cdot\tilde{\mathbb{C}}[\mathbf{e}_z\otimes\mathbf{e}_z] - \frac{(\mathbf{e}_z\otimes\mathbf{e}_z\cdot\tilde{\mathbf{A}})(\mathbf{X}\cdot\tilde{\mathbf{A}})}{x}\right)^2}{\mathbf{e}_z\otimes\mathbf{e}_z\cdot\tilde{\mathbb{C}}[\mathbf{e}_z\otimes\mathbf{e}_z] - \frac{(\mathbf{e}_z\otimes\mathbf{e}_z\cdot\tilde{\mathbf{A}})^2}{x}} \\ x &= \left(2G(F(\alpha)^2+(1-F(\alpha))^2) + F^2(\alpha)\frac{\partial g}{\partial z}\right)F_1(\alpha)^{-1}.\end{aligned} \tag{6.33}$$

We obtain the incremental moduli K_{11} for $\mathbf{X} = \mathbf{e}_1\otimes\mathbf{e}_1$ and K_{33} for $\mathbf{X} = \mathrm{sym}\,(\mathbf{e}_1\otimes\mathbf{e}_2)$, i.e. the tangential shear modulus.

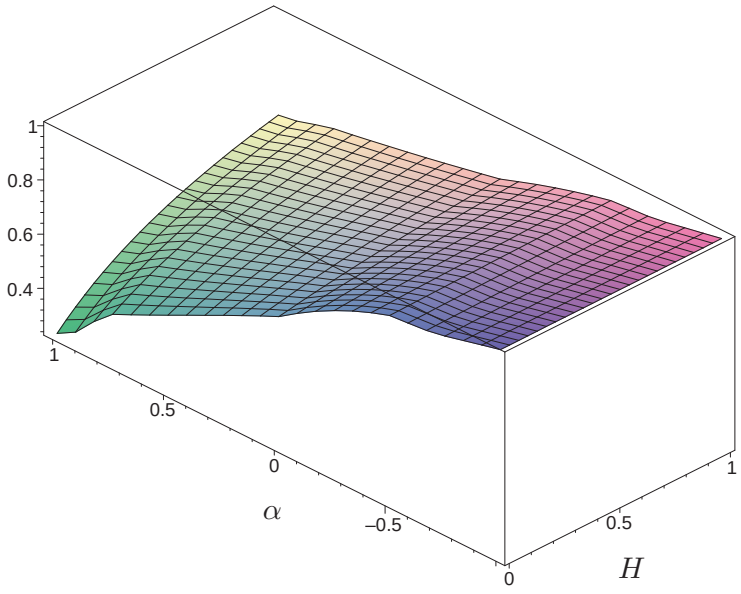

Fig. 6.2: The incremental modulus $K_{11}(H, \alpha)$

For the J_2 flow theory, $F(\alpha) \equiv F_1(\alpha) \equiv 1$ in the plastic regime leads to $x = 2G + \frac{\partial g}{\partial z}$ and $\tilde{\mathbf{A}} = 2G\,\tilde{\mathbf{M}}_{\mathrm{N}}$. If $\tilde{\mathbf{M}}_{\mathrm{N}}$ has no shear component, like in the case of tensile predeformation, $\mathbf{X} \cdot \tilde{\mathbf{A}} = 0$, and thus $\mathrm{K}_{33} = 2G$. This excessive stiffness for strongly nonproportional processes is a major drawback of the J_2 flow theory (see Fig. 6.5).

The incremental moduli K_{11} and K_{33} have been normalized by the according elastic values. Figures 6.2 and 6.3 show plots of these moduli as a function of $H = \frac{\frac{\partial g}{\partial z}}{2G}$ and α. For the determination of the functions $F(\alpha)$ and $F_1(\alpha)$ see the next Section 6.4.

The longitudinal modulus increases steadily with deviation from a proportional process ($\alpha = 1$) and finally enters the elastic value for the reversed process ($\alpha = -1$).

The shear modulus shows different behaviour. In addition to the reversed process, for $\alpha = 1$ the elastic modulus is obtained. This seems to be a parellelism to J_2 flow theory. However, one should bear in mind that after a tensile process, shear cannot be obtained in a process of $\alpha = 1$. For a total shift to a shear processes, $\alpha = 0$ and accordingly the incremental modulus of the vertex model is much lowered in comparison to J_2 flow theory.

Both moduli in general depend on the hardening modulus.

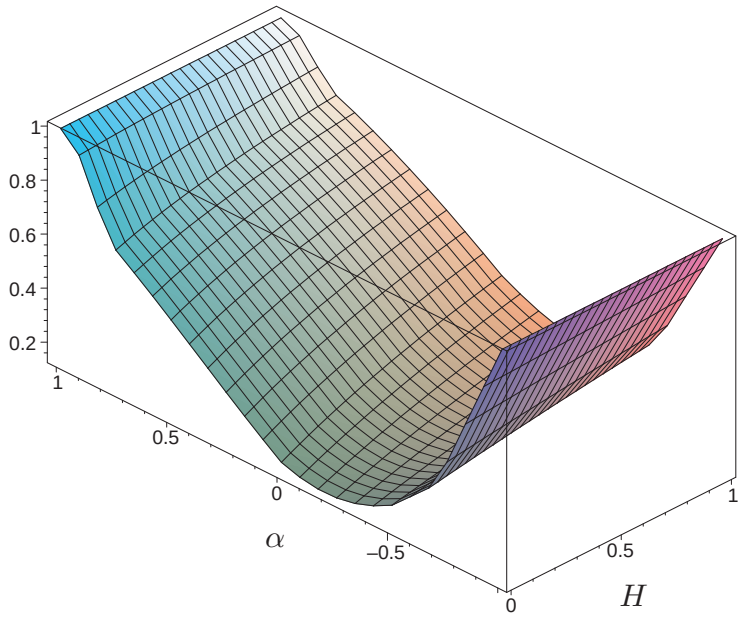

Fig. 6.3: The incremental shear modulus $K^*_{33}(H^*, \alpha)$

E	123000 MPa	ν	0.30
$\frac{\partial g}{\partial z}$	$0.01\,E$		

Tab. 6.2: Material parameters for Copper of the macroscopic model

6.3.3 Rotational symmetric moduli

6.4 Parameter estimation by micro-macro-simulation

To estimate the parameters of the governing equations, a 1000-grain Taylor-Lin model of a polycrystal was used. The parameters were adopted to the elastic properties of copper as well as the stress-strain-curve. A strain-controlled predeformation in a volume preserving tension process was prescribed (cf. Table 5.3). The prestrain reached an equivalent logarithmic strain of 2×10^{-2}.

For the macroscopic vertex model summarized in Table 6.1, this state was assumed as the reference state and thus $\mathbf{P} = \mathbf{1}$ was used. For the smallness of predeformation, the isotropy of the aggregate was still given. The elastic parameters were adopted to the known values of copper, as well as the hardening modulus of a straight continuation. The resulting parameters are summarized in Table 6.2.

From this state, different continuation processes with an additional shear component of the strain rate were simulated. As measure of outcome, the stress

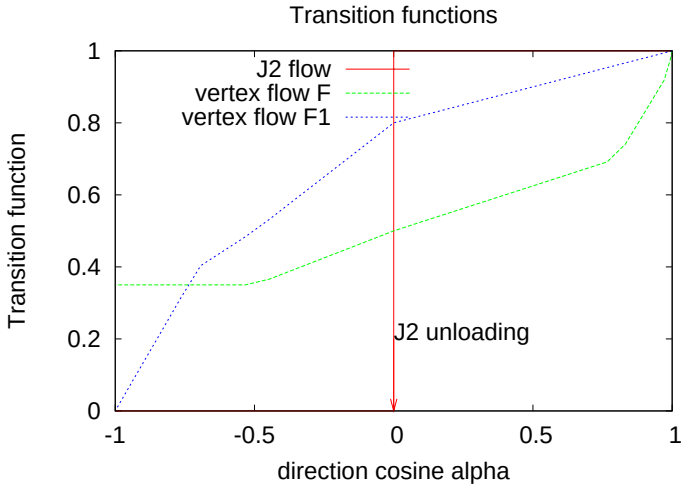

Fig. 6.4: Transition function for the macroscopic vertex model

response upon small strain steps ($\Delta\epsilon_{\log} = 10^{-5}$) in different directions as well as the dissipated power on these processes has been used.

The transition functions $F(\alpha)$ and $F_1(\alpha)$ were treated as fit functions and modeled with piecewise defined functions (Fig. 6.4). In addition, the transition function leading to the classical J_2 flow theory is shown, which is identical to the Heaviside jump function .

The stress increments following from the continuation paths for the macroscopic vertex model and the Taylor-Lin model (with opposite direction of shear strain to improve readability) show a good agreement (Fig. 6.5).

For comparison the J_2 flow theory is shown. Due to the restriction of the plastic flow in direction of the history stress, it is unable to exhibit the additional shear component. Thus, the shear stress increments are elastic and by far exceed the values obtained by the Taylor-Lin model.

The vertex angle θ^c delimits processes that are nearly dissipation free. It has been taken from Fig. 5.10b. For $\alpha < \cos\theta^c$, elastic behaviour gives an acceptable approximation of the material behavior. However, differences can still be identified.

The exact dependence of the stress and strain increment directions can be found in Fig. 6.6. Here the deviation of the actual stress increments from the proportional path, $\beta_2 = \frac{\Delta\tilde{\mathbf{C}}\tilde{\mathbf{S}}\cdot\tilde{\mathbf{C}}\tilde{\mathbf{S}}}{\|\Delta\tilde{\mathbf{C}}\tilde{\mathbf{S}}\|\|\tilde{\mathbf{C}}\tilde{\mathbf{S}}\|}$ has been used. It is compared to $\alpha = \left.\frac{\Delta\tilde{\mathbf{C}}\tilde{\mathbf{S}}\cdot\tilde{\mathbf{C}}\tilde{\mathbf{S}}}{\|\Delta\tilde{\mathbf{C}}\tilde{\mathbf{S}}\|\|\tilde{\mathbf{C}}\tilde{\mathbf{S}}\|}\right|_{\mathbf{P}=\text{const}}$ that is computed under the assumption of elastic behaviour and thus directly connected with the strain rate direction. The definition is in accordance with the other measures of deviation from proportional path. The improvement by the macroscopic vertex model compared to the J_2

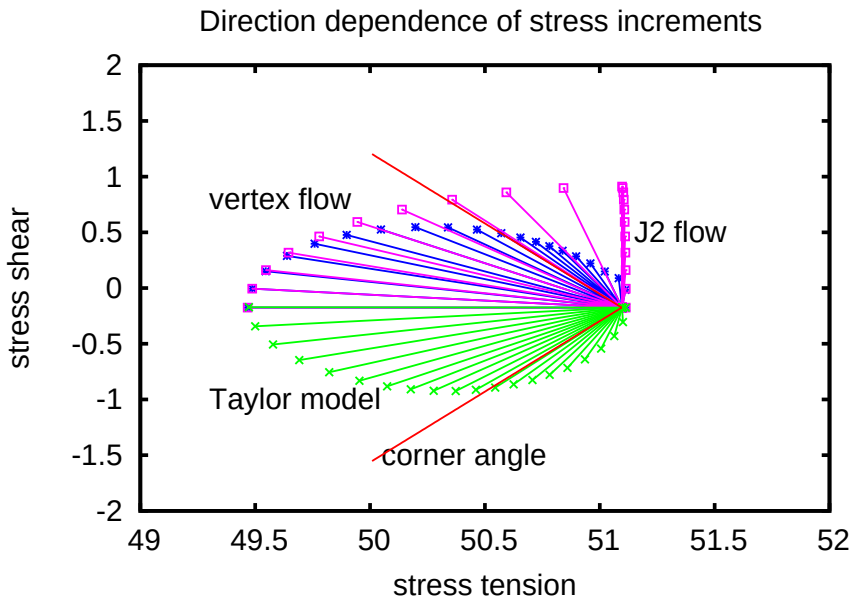

Fig. 6.5: Stress increments upon strain path change

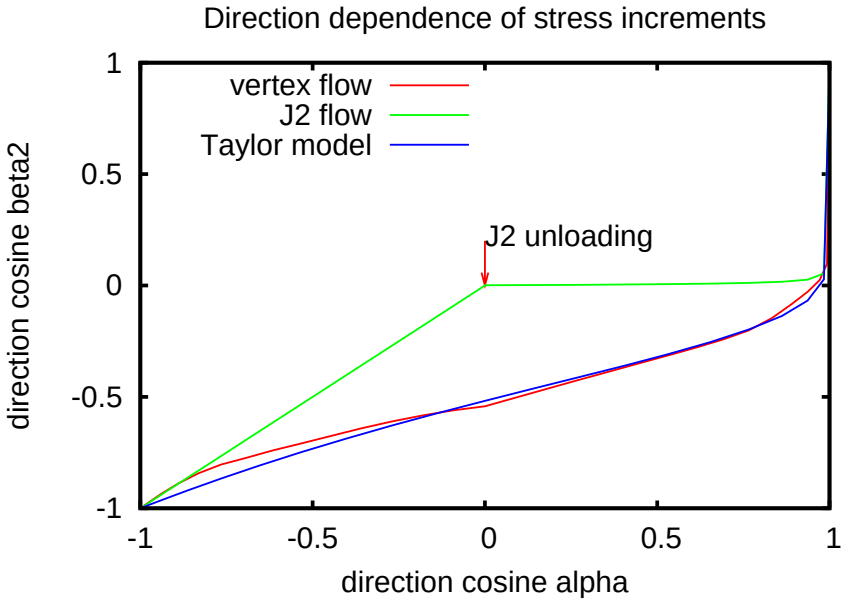

Fig. 6.6: Direction of stress increment vs. direction of strain increment

flow theory is obvious.

The sudden decrease in the transition function $F(\alpha)$ even for small deviations from proportional straining reflects the fact that the yield-surface-parallel component of the plastic flow is absent only for strictly proportional processes. This additional component is necessary to compensate for the otherwise observed excessive lateral stress increments due to the elastic response.

But these must also not be suppressed completely. 6.6 shows, that only in a proportional process stress and strain rate keep in line ($\beta_2 = 1$). For all nonproportionals paths, the Taylor model predicts stress increment components in the lateral direction that are of similar size as those in the proportional direction. The lateral component is also present in the J_2 flow theory, but it is much too large. Accordingly, it dominates over the proportional component, maintaining the zero level of β_2.

For the vertex model, the lowered lateral component restores the influence of the (negative) proportional component, resulting in a direction of the stress rate that is not oriented laterally, but inclined backwardly, as observed in the Taylor model prediction.

In the unloading range, the direction of the actual stress rate approaches a totally reversed stress process. In the case of J_2 theory this happens in a linear manner, as expected, because in the elastic unloading range $\alpha = [-1, 0]$, $\alpha = \beta_2$.

The Vertex model has smaller values of β_2 because it avoids the large elastic stress increments and the unloading range is smaller. Still, stress and strain are in line only for strictly proportional processes.

As a second measure of outcome, the changing dissipation on different continuation paths is compared. Here, the second transition function $F_1(\alpha)$ gains importance. The dissipation is always larger than the result of the classical plasticity, in accordance with the second law.

Additionally, zero-lines of the plastic potential $\hat{\Pi}(\tilde{\mathbf{C}}\tilde{\mathbf{S}}, g, \mathbf{M}_\mathrm{N}, \mathbf{M})$ were determined in stress space (Fig. 6.8) at fixed values of g but for different values of the loading direction $\mathbf{M}_0$. They all intersect at one stress point, $(\tilde{\mathbf{C}}\tilde{\mathbf{S}})'$. This point lies on the yield locus defined by $\Phi = \hat{\Phi}((\tilde{\mathbf{C}}\tilde{\mathbf{S}})', g) = 0$. It is the actual stress reached in the prestrain process, according to the traveling vertex assumption. The normal of the distinct lines is the process-dependend direction of plastic flow. One finds that the normal at the actual stress point rotates toward the direction of strain rate for nonproportional processes.

6.5 Comparisons with Experiments

For a prescribed strain process, the material model has been implemented in the implicit integration code `RADAU5` (Hairer and Wanner, 1996). The stress-strain curve has been reproduced by linear interpolation of $\hat{g}(z)$ between sample points (Fig. 6.9).

In accordance with a nonproportional tension-torsion experiment on a tubular specimen as reported by Lensky (1960), a complex strain path was prescribed. It includes several stages of loading and unloading, each with a con-

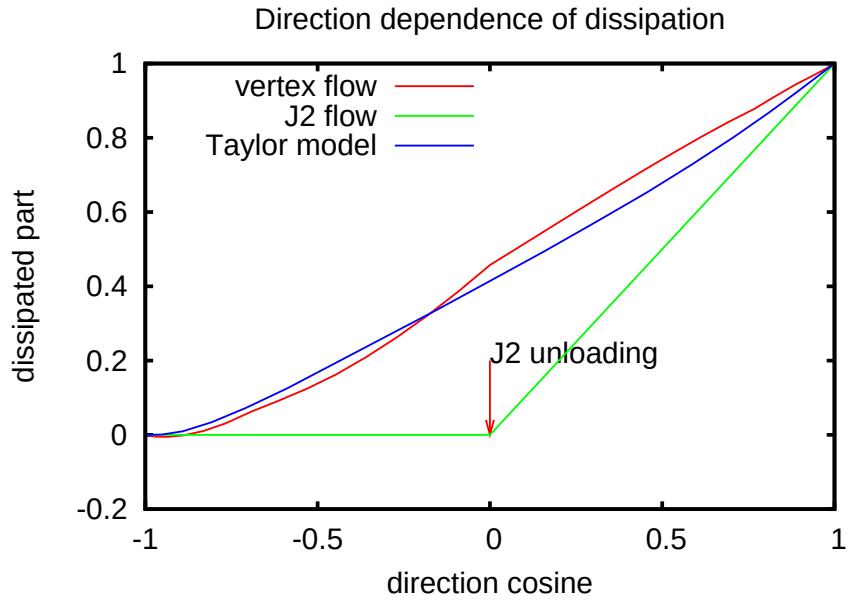

Fig. 6.7: Dissipation upon strain path change

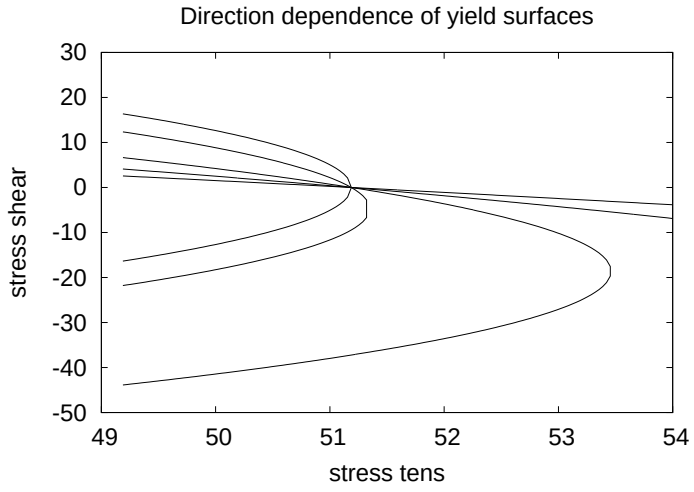

Fig. 6.8: Process dependent yield surfaces for different proportional and non-proportional continuation processes from one point.

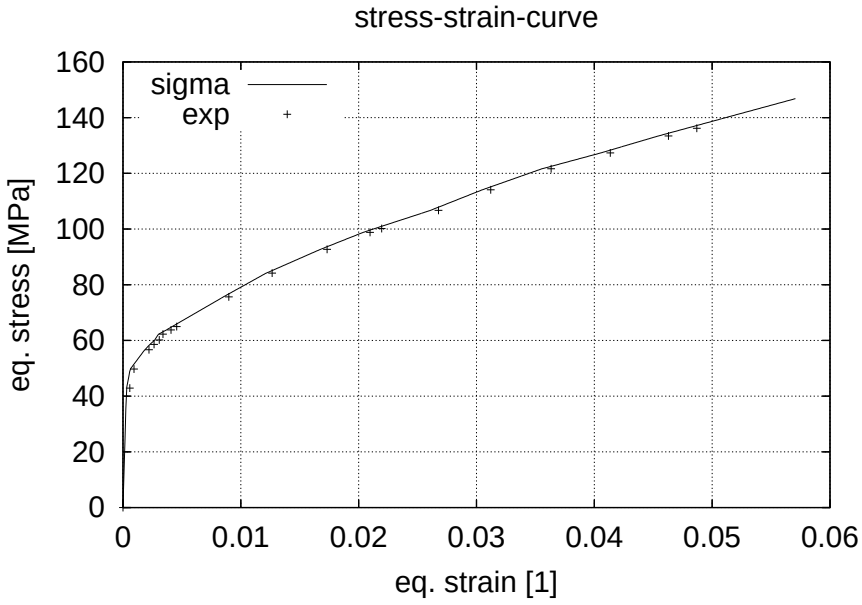

Fig. 6.9: Stress-strain curve reported by Lensky (1960)

stant strain rate (Fig. 6.10a, points Oe-Ae-...-Fe correspond to Os-As-...-Fs for strain and stress, respectively).

The numerical simulation resulted in the internal variables and the stress response. For comparison, both the transition functions $F(\alpha)$ by which the direction of plastic flow is adapted according to the process direction and $F_1(\alpha)$ which does the same for the dissipation, have been adjusted to the Heaviside function, resulting in the J_2 flow theory of plasticity. For both cases, identical strain processes were used.

At the beginning of each stage, a stress transient can be found. Stress and strain rate have different directions. Additional straining in the new direction makes the stress point to run quickly along the yield surface until stress and strain are parallel (Kuroda and Tvergaard, 1999, Kuwabara et al., 2000). After that, the direction of the stress rate is constant. This proportional behaviour is reached at less additional strain with the J_2-Theory, as indicated by the smaller stress level after less strain hardening. However, at the beginning of the next stage, both results are in line again.

This effect of deviation from coaxiality of stress and strain rate and regaining after some plastic strain has been labeled *delay effect* by Lensky (1960)

Fig. 6.10b clarifies the nature of the effect: From every point on the strain path, the stress scaled by an appropriate factor has been drawn. After a change of the prescribed strain rate direction, a transient phase with a rotation of the

stress direction can be seen, that corresponds to the above explanation. The J_2 flow theory has a shorter transient.

Qualitatively similar results have been obtained by Gotoh (1985a,c).

For a quantitative comparison we follow the way Lensky (1960) reported his results. The tension-torsion stress and strain processes have been parametrized in a twodimensional subspace of the symmetric tensors. As a natural basis, the components tangential (T) and normal (N) to the strain path were used. In accordance with the above findings, the normal component has to decay with further strain. This is in fact the case for both theories. However, the decay is finished prematurely for the J_2-Theory, while a realistic behavior is obtained with the vertex model (Fig. 6.11).

A second type of experiments has been conducted with smooth nonproportional paths. By prescription of a circular path in the strain space, hardening plasticity results in a spiral-shaped stress process (Fig. 6.12(a)). For changing curvature, the stresses of the competing theories have been plotted together in Fig. 6.12(b) and 6.13(a). The nonproportional nature of the process results in increasing deviation of the stress from the respective direction of strain rate. This effect is more pronounced for smaller radii of curvature.

Accordingly, for nearly proportional processes with curvatures as in Fig. 6.12(b), the J_2-theory gives satisfactory results and is thus appropriate for such processes. An explanation for such behavior can be given in accordance with Lensky (1960): Based on Fig. 6.11 one can estimate the *trace of delay*, i.e. the strain that is necessary to re-obtain proportional behaviour after a kink in the process path, approx. 0.007. This value is in between the radii of curvature of the Figures 6.12(b) and 6.13(a), explaining the differences between the two constitutive approaches. For a radius below 0.007, an approximation using the J_2-theory that is certainly suitable for proportional processes is not appropriate, while the vertex model yields results as the experiments reproduced in Fig. 6.13(b).

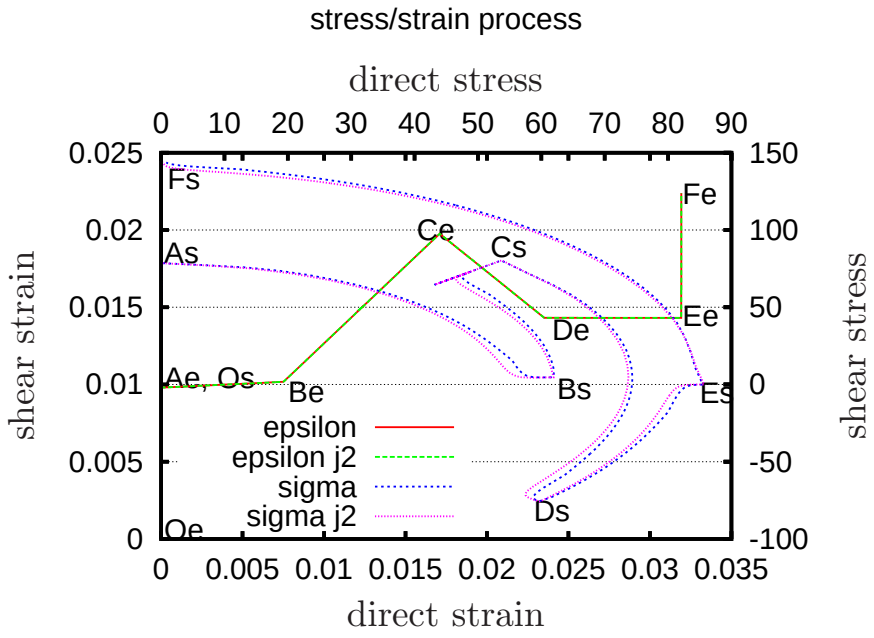

a

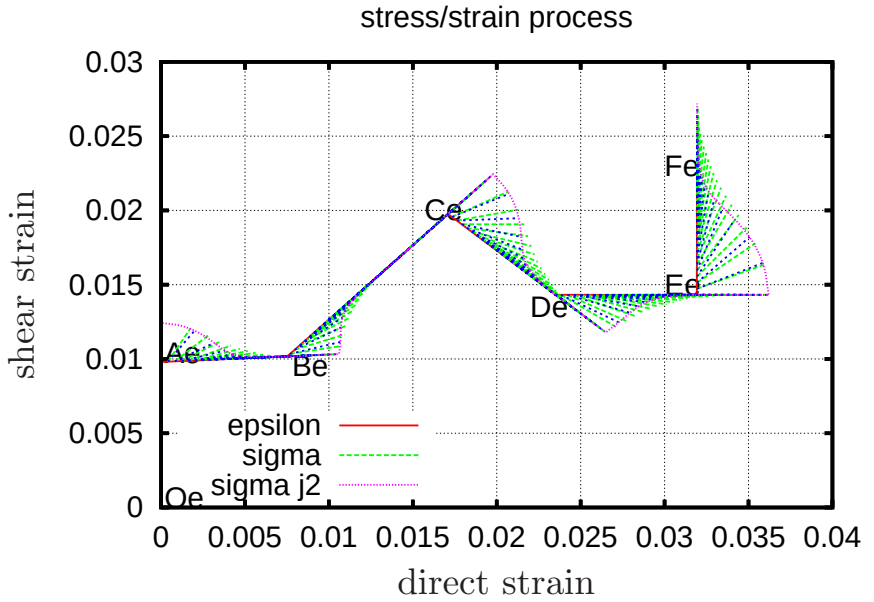

b

Fig. 6.10: Stress and strain process after Lensky (1960)

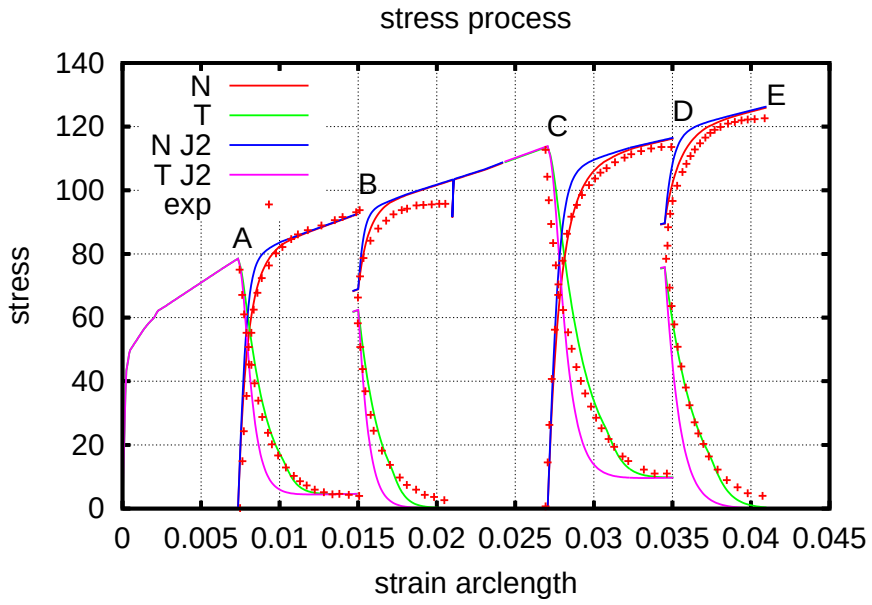

Fig. 6.11: Comparison with experimental results

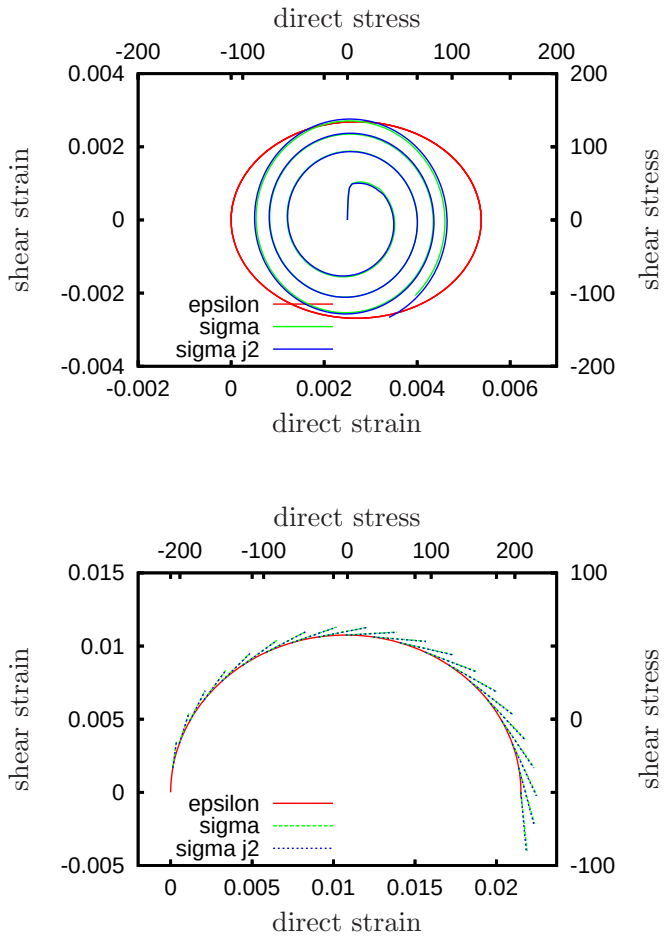

Fig. 6.12: Stress response on smooth curved strain process paths 1

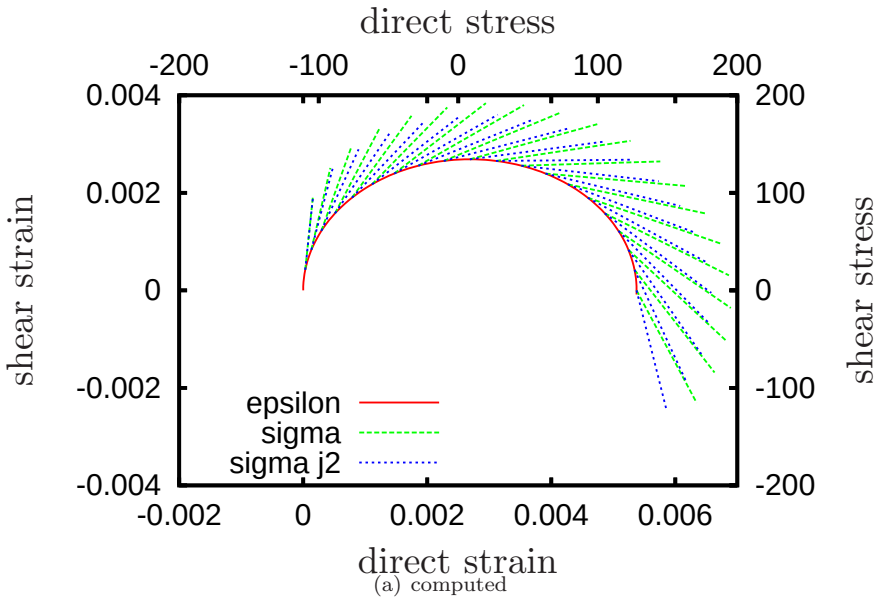

(a) computed

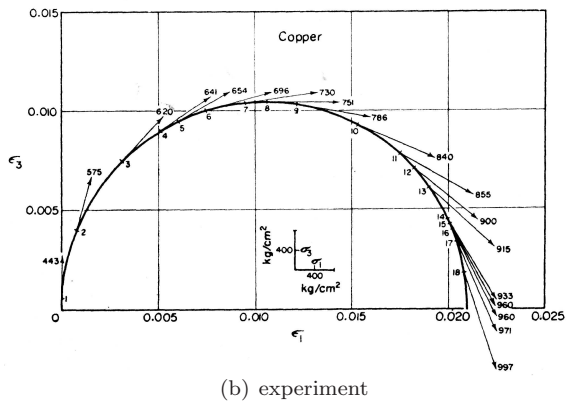

(b) experiment

Fig. 6.13: Stress response on smooth curved strain process paths 2

7. PLASTIC BUCKLING OF A CRUCIFORM COLUMN

Section Overview
The proposed vertex model of plasticity is applied to the torsional buckling of a cruciform column in the plastic regime. The problem is solved analytically based on the von Kármán shallow shell theory and the virtual work principle. Solutions found in the literature are extended for process-dependend incremental behaviour as typically found in the presence of the vertex effect.

This approach accounts for the often observed problems in assigning the proper incremental stiffness to such problems. It is shown that a reduced modulus based on a weighted cross-section average has to be used.

Petryk's energy criterion of path stability is used in conjunction with the rate potential to find the stable secondary solution after a bifurcation. Using the proposed vertex model, a comparison with experimental buckling tests shows good agreement.

The same applies to a numerical solution based on finite element eigenvalue buckling.

7.1 The cruciform as a standard example for plastic buckling

Thin walled open structures tend to buckle in the torsion mode under applied compressive loads. If the applied load exceeds the yield load, the twisted structure is still in the total plastic state. In contrast the bending mode that governs very slender columns leads to unloading in the stretched fibres.

Moreover, bending is a completely one-dimensional case without any influence of the vertex effect. In contrast, in the torsion mode the flanges of the column show additional twisting and thus change from compression to a combination of compression and shear.

Gerard and Becker (1957, Fig. 5) compared experimental results for cruciform columns made out of 2024-T4 Aluminum alloys with analytical approaches. Various ratios of flange width and thickness were tested. The J_2 flow theory of plasticity and the deformation theory were used to obtain analytical results. They appeared to favor the deformation theory. These results gave experimental evidence for certain shortcomings of the J_2 flow theory for the first time (Caner et al., 2002).

Using a nonlinear von Kármán shell theory with an inelastic incremental law, Hutchinson and Budiansky (1976) showed that the reason is the shear stiffness in a precompressed column. The J_2 flow theory predicts elastic behavior after

such a change of the strain path. However, by introducing an imperfection (pretwist) of the column, useful results could be obtained. According to Lubliner (1990, sect. 5.3) models using thin shells and the J_2 flow theory generally exhibit very strong sensitivity for imperfections.

Black et al. (2002) studied the inelastic buckling behaviour of cruciform columns used as dissipative elements in earthquake-sustaining steel constructions. They applied a torsion theory enhanced by the consideration of equilibrium in the deformed state of an imperfect (pretwisted) column. As a result, the incremental shear modulus is linked to the (inelastic) compressive modulus, instead to the elastic modulus as otherwise predicted.

Falgoust (2004) took cruciform columns as an example to establish the existence of the Wagner effect (Wagner, 1929) in such structures, i.e. the rotation of the principal stresses with the material in elastic thinwalled structures. This is the same effect that has been exploited in the treatment by Black et al. (2002).

The plastic cruciform is a standard example for the failure of J_2 flow theory in prediction of buckling loads of perfect structures (Lubliner (1990, sect. 5.3), Bažant and Cedolin (1991, sect. 8.1), Nguyen (2000, sect. 14.3.2.2)).

7.2 The analytical model

We model the behaviour of the cruciform 7.1(a) by the nonlinear von Kármán plate theory as proposed in the literature (e.g. Hutchinson and Budiansky, 1976, Nguyen, 2000). The presentation given in the sequel is valid for shallow shells as well.

Let x_1 and x_2 be the in-plane coordinates that parametrize the shell's mid-surface, while $x_3 \equiv z$ is the thickness coordinate. Accordingly, $\mathbf{x}_2 = (x_1, x_2)$ is the planar position vector component. For differentiation, we use the planar operator ∇_2.

The displacement vector is decomposed in the same way, $\mathbf{u}_2 = (u_1, u_2)$, $u_3 \equiv w$. If the reference coordinates of the shell are given by $\bar{Z}(x_1, x_2)$, the planar von Kármán strain acting in the mid-surface is

$$\begin{aligned} \mathbf{E}_2^p(\mathbf{x}_2) &= \boldsymbol{\epsilon}_2 + \frac{1}{2}\left(\nabla_2\bar{Z} \otimes \nabla_2 w + \nabla_2 w \otimes \nabla_2\bar{Z} + \nabla_2 w \otimes \nabla_2 w\right) \\ \boldsymbol{\epsilon}_2^p(\mathbf{x}_2) &= \frac{1}{2}(\mathbf{u}_2 \otimes \nabla_2 + \nabla_2 \otimes \mathbf{u}_2). \end{aligned} \tag{7.1}$$

Plate kinematics are introduced using the tensor of curvature

$$\mathbf{K}(\mathbf{x}_2) = \nabla_2 w \otimes \nabla_2 \tag{7.2}$$

and the Bernoulli-Kirchhoff hypothesis resulting in the strain

$$\mathbf{E}_2(\mathbf{x}_2, z) = \mathbf{E}_2^p(\mathbf{x}_2) - z\,\mathbf{K}(\mathbf{x}_2). \tag{7.3}$$

We model torsional displacement of a single flange in the x_1-x_2-plane by an ansatz

$$w(\mathbf{x}_2) = x_2\,\Phi(x_1), \tag{7.4}$$

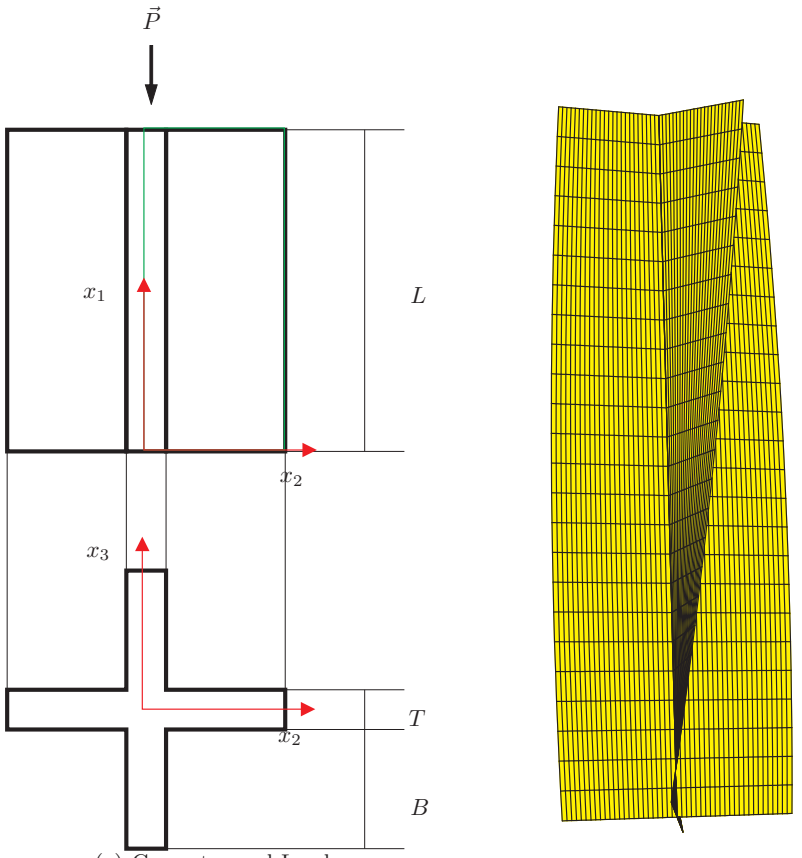

(a) Geometry and Load

(b) Buckling mode (7.22)

Fig. 7.1: Buckling mode (7.4) of a cruciform column

and a similar one for a torsional imperfection mode,

$$\bar{Z}(\mathbf{x}_2) = x_2\,\bar{\Phi}(x_1). \tag{7.5}$$

For the in-plane displacement, Hutchinson and Budiansky (1976) made the following proposal:

$$\begin{aligned} u_1 &= \epsilon_0 x_1 \\ u_2 &= -(\bar{\Phi}\Phi + \Phi^2 - \epsilon_1)x_2 \end{aligned} \tag{7.6}$$

The in-plane shear and the 22 components of the linear and nonlinear part cancel each other and the midsurface strain tensor is

$$\mathbf{E}_2^p = \begin{pmatrix} \epsilon_0 + (\Phi'\bar{\Phi}' + \frac{1}{2}\Phi'^2)x_2^2 & 0 \\ 0 & +\epsilon_1 \end{pmatrix}. \tag{7.7}$$

The according tensor of curvature

$$\mathbf{K} = \begin{pmatrix} \Phi'' x_2 & \Phi' \\ \Phi' & 0 \end{pmatrix} \tag{7.8}$$

gives the planar Green's strain field in the von Kármán approximation

$$\mathbf{E}_2 = \begin{pmatrix} \epsilon_0 + (\Phi'\bar{\Phi}' + \frac{1}{2}\Phi'^2)x_2^2 - \Phi'' x_2 z & -\Phi' z \\ -\Phi' z & \epsilon_1 \end{pmatrix}. \tag{7.9}$$

By introducing the torsion rate $\varphi = \dot{\Phi}$, the according strain rate field is

$$\dot{\mathbf{E}}_2 = \begin{pmatrix} \dot{\epsilon}_0 + (\varphi'\bar{\Phi}' + \varphi'\Phi')x_2^2 - \varphi'' x_2 z & -\varphi' z \\ -\varphi' z & \dot{\epsilon}_1 \end{pmatrix}. \tag{7.10}$$

Application of the plain strain incremental material law (6.32) yields the second Piola-Kirchhoff stress rate,

$$\begin{aligned} \dot{\mathbf{S}} &= \mathbb{K}[\dot{\mathbf{E}}] \\ \mathbb{K} &= \frac{\partial \dot{\mathbf{S}}}{\partial \dot{\mathbf{E}}} \\ \dot{S}_{11} &= \mathrm{K}_{11}(\dot{\mathbf{E}}_2)_{11} + \mathrm{K}_{12}(\dot{\mathbf{E}}_2)_{22} \\ \dot{S}_{22} &= \mathrm{K}_{12}(\dot{\mathbf{E}}_2)_{11} + \mathrm{K}_{22}(\dot{\mathbf{E}}_2)_{22} \\ \dot{S}_{12} &= \mathrm{K}_{33}(\dot{\mathbf{E}}_2)_{12} \end{aligned} \tag{7.11}$$

Following Hutchinson and Budiansky (1976) we use the virtual work principle in the presence of the normal force $N_{11} = \int_{-\frac{T}{2}}^{\frac{T}{2}} S_{11}\,\mathrm{d}z$ and the twisting moment $M_{12} = \int_{-\frac{T}{2}}^{\frac{T}{2}} S_{12} z\,\mathrm{d}z$, where the S_{ij} are the according components of the second Piola-Kirchhoff stress,

$$\int_0^L \int_0^B 2M_{12}\,\delta K_{12} + N_{11}\,\delta(\mathbf{E}_2)_{11}\,\mathrm{d}x_2 + P\,\delta\epsilon_0\,\mathrm{d}x_1 = 0. \tag{7.12}$$

After insertion,

$$\int_0^L \int_0^B \int_{-\frac{T}{2}}^{\frac{T}{2}} -2S_{12}z\,\delta\Phi' + S_{11}\left(\delta\epsilon_0 + x_2^2(\bar{\Phi}' + \Phi')\,\delta\Phi'\right)\,\mathrm{d}z\,\mathrm{d}x_2 + P\,\delta\epsilon_0\,\mathrm{d}x_1 = 0, \tag{7.13}$$

time differentiation of this material equation yields a rate equation for the rates $\dot{\epsilon}_0$ and $\varphi = \dot{\Phi}$,

$$\begin{aligned}\int_0^L \Bigg(\int_0^B \int_{-\frac{T}{2}}^{\frac{T}{2}} \left[-2\dot{S}_{12}z + S_{11}x_2^2(\varphi') + \dot{S}_{11}x_2^2(\bar{\Phi}' + \Phi')\right]\,\mathrm{d}z\,\mathrm{d}x_2\;\delta\Phi' \\ + \left[\int_0^B \int_{-\frac{T}{2}}^{\frac{T}{2}} \dot{S}_{11}\,\mathrm{d}z\,\mathrm{d}x_2 + \dot{P}\right]\;\delta\epsilon_0\Bigg)\,\mathrm{d}x_1 = 0.\end{aligned} \tag{7.14}$$

By a standard procedure two independend results can be obtained,

$$\begin{aligned}\int_0^B \int_{-\frac{T}{2}}^{\frac{T}{2}} \dot{S}_{11}\,\mathrm{d}z\,\mathrm{d}x_2 + \dot{P} = 0,\\ \int_0^L \int_0^B \int_{-\frac{T}{2}}^{\frac{T}{2}} \left[-2\dot{S}_{12}z + S_{11}x_2^2(\varphi') + \dot{S}_{11}x_2^2(\bar{\Phi}' + \Phi')\right]\,\delta\Phi'\,\mathrm{d}z\,\mathrm{d}x_2\,\mathrm{d}x_1 = 0.\end{aligned} \tag{7.15}$$

Starting from a undisturbed placement on the primary path as given by $\bar{\Phi} \equiv \Phi \equiv 0$, and using $\dot{S}_{12} = \mathrm{K}_{33}\dot{E}_{12} = -\mathrm{K}_{33}z\varphi'$, the bifurcation equation

$$\int_0^L \int_0^B \int_{-\frac{T}{2}}^{\frac{T}{2}} \left[2\mathrm{K}_{33}z^2 + S_{11}x_2^2\right]\varphi'\,\delta\Phi'\,\mathrm{d}z\,\mathrm{d}x_2\,\mathrm{d}x_1 = 0 \tag{7.16}$$

has a solution which is independend of the actual shape of the eigenmode φ.

7.3 The valid reduced modulus

The choice of the valid modulus K_{33} has been of major interest to research, due to the finding that the elastic shear modulus as predicted by the J_2 flow theory (see Section 6.3) overestimates the experimental results.

For the proposed vertex model, $\mathrm{K}_{33} = \mathrm{K}_{33}(\alpha)$ is a function of the process continuation, and in particular, of the loading direction α (6.33). Its determination is beyond the scope of classical treatments of this problem.

In the proportional fundamental (primary) path before buckling occurs, the natural direction is given by

$$\tilde{\mathbf{M}}_{\mathrm{N}} = \frac{1}{\sqrt{\frac{2}{3}(\dot{\epsilon}_0^2 + \dot{\epsilon}_0\dot{\epsilon}_1 + \dot{\epsilon}_1^2)}} \begin{pmatrix} -\frac{2}{3}\dot{\epsilon}_0 - \frac{1}{3}\dot{\epsilon}_1 & 0 & 0 \\ 0 & +\frac{2}{3}\dot{\epsilon}_0 + \frac{1}{3}\dot{\epsilon}_1 & 0 \\ 0 & 0 & \frac{\dot{\epsilon}_0 - \dot{\epsilon}_1}{3} \end{pmatrix}. \tag{7.17}$$

The secondary path's additional twisting mode from (7.10) gives the strain rate deviator

$$\begin{aligned}\dot{\mathbf{E}}' = &\begin{pmatrix} -\frac{2}{3}\dot\epsilon_0 - \frac{1}{3}\dot\epsilon_1 & 0 & 0 \\ 0 & +\frac{2}{3}\dot\epsilon_0 + \frac{1}{3}\dot\epsilon_1 & 0 \\ 0 & 0 & \frac{\dot\epsilon_0 - \dot\epsilon_1}{3} \end{pmatrix} \\ &- z \begin{pmatrix} \frac{2}{3}x_2\varphi'' & \varphi' & 0 \\ \varphi' & -\frac{1}{3}x_2\varphi'' & 0 \\ 0 & 0 & -\frac{1}{3}x_2\varphi'' \end{pmatrix}\end{aligned} \tag{7.18}$$

and accordingly

$$\begin{aligned}\tilde{\mathbf{M}}_0 = &\frac{1}{\sqrt{\frac{2}{3}(\dot\epsilon_0^2 + \dot\epsilon_0\dot\epsilon_1 + \dot\epsilon_1^2 + z^2x_2^2\varphi''^2) + 2z^2\varphi'^2}}[\\ &\begin{pmatrix} -\frac{2}{3}\dot\epsilon_0 - \frac{1}{3}\dot\epsilon_1 & 0 & 0 \\ 0 & +\frac{2}{3}\dot\epsilon_0 + \frac{1}{3}\dot\epsilon_1 & 0 \\ 0 & 0 & \frac{\dot\epsilon_0 - \dot\epsilon_1}{3} \end{pmatrix} \\ &- z \begin{pmatrix} \frac{2}{3}x_2\varphi'' & \varphi' & 0 \\ \varphi' & -\frac{1}{3}x_2\varphi'' & 0 \\ 0 & 0 & -\frac{1}{3}x_2\varphi'' \end{pmatrix}]\end{aligned} \tag{7.19}$$

Thus the direction parameter varies in the cross-section. With $\mu = \frac{\dot\epsilon_1}{\dot\epsilon_0}$,

$$\alpha = \frac{1 + \mu + \mu^2 - zx_2\frac{\varphi''}{\dot\epsilon_0}[-\frac{7}{6} - \frac{1}{3}\mu]}{\sqrt{1+\mu+\mu^2}\sqrt{1 + \mu + \mu^2 + z^2x_2^2\left(\frac{\varphi''}{\dot\epsilon_0}\right)^2 + 3z^2\left(\frac{\varphi'}{\dot\epsilon_0}\right)^2}} \tag{7.20}$$

For a uniaxial deformation process, $\mu = \dot\epsilon_1 = 0$ and we obtain

$$\alpha = \frac{1 + \frac{7}{6}zx_2\frac{\varphi''}{\dot\epsilon_0}}{\sqrt{1 + z^2x_2^2\left(\frac{\varphi''}{\dot\epsilon_0}\right)^2 + 3z^2\left(\frac{\varphi'}{\dot\epsilon_0}\right)^2}}. \tag{7.21}$$

Hutchinson and Budiansky (1976) proposed a linear x_1-dependence of the bifurcation eigenmode,

$$\Phi' = \Theta \Leftrightarrow \varphi'' \equiv 0, \varphi' = \theta \tag{7.22}$$

(see Fig. 7.1(b)), which further reduces the result to

$$\alpha = \frac{1}{\sqrt{1 + 3z^2\left(\frac{\theta}{\dot\epsilon_0}\right)^2}}. \tag{7.23}$$

This arbitrariness is justified by the shape-independence of the bifurcation equation (7.16).

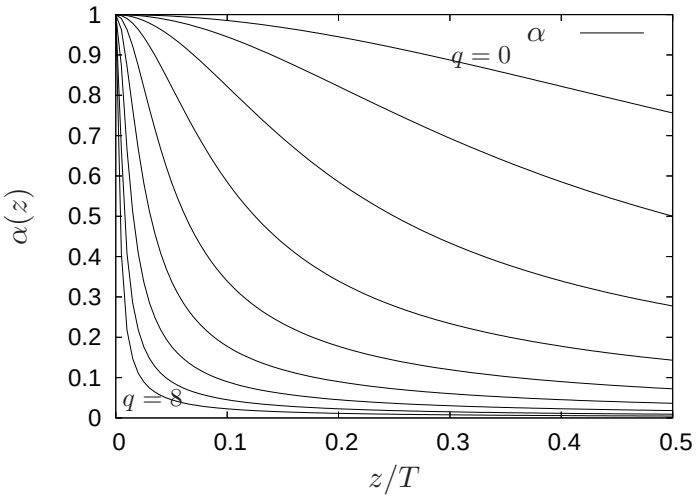

Fig. 7.2: Variability of α in the cross section for different $\frac{\theta}{\dot{\epsilon}_0} = 2^q$

The only remaining variability is in z-direction. It has been plotted in Fig. 7.2 for different values of $\frac{\theta}{\dot{\epsilon}_0} = 2^q$, $q = 0 \ldots 8$. Obviously, on the midsurface $z = 0$, $\alpha = 1$. There is a range in the vicinity of the midsurface where the J_2 flow theory (which is characterized exactly by $\alpha = 1$) is a good approximation. Its thickness shrinks with growing dominance of the buckling mode. For the limit case, we obtain

$$\lim_{\frac{\theta}{\dot{\epsilon}_0} \to \infty} \alpha = \begin{cases} 1 & \text{at } z = 0 \text{ only} \\ 0 & \text{almost everywhere} \end{cases} . \tag{7.24}$$

We integrate the essential part of $(7.16)_2$,

$$\int_0^B \int_{-\frac{T}{2}}^{\frac{T}{2}} \left[2\mathrm{K}_{33} z^2 + S_{11} x_2^2 \right] \mathrm{d}z \, \mathrm{d}x_2 = \frac{BT^3}{6} \bar{\mathrm{K}}_{33} + S_{11} \frac{TB^3}{3} = 0 \tag{7.25}$$

where the reduced shear modulus $\bar{\mathrm{K}}_{33}$ has been obtained by application of the mean value. It can be explicitely obtained by substitution,

$$\begin{aligned} z &= (3u)^{\frac{1}{3}} \\ \alpha &= \frac{1}{\sqrt{1 + 3^{\frac{5}{3}} u^{\frac{2}{3}} \left(\frac{\theta}{\dot{\epsilon}_0} \right)^2}} \\ \bar{\mathrm{K}}_{33} &= \frac{24}{T^3} \int_0^{\frac{T^3}{24}} \mathrm{K}_{33}(\alpha) \, \mathrm{d}u. \end{aligned} \tag{7.26}$$

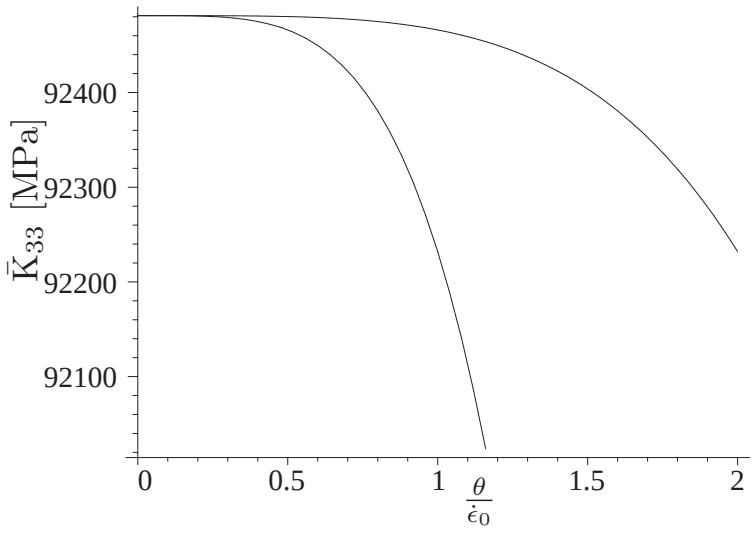

Fig. 7.3: The reduced shear modulus $\bar{\mathrm{K}}_{33}$ as a function of $\frac{\theta}{\dot{\epsilon}_0}$ at $T = 0.1$ mm (upper) and $T = 0.2$ mm (lower line)

The result for the critical buckling load is

$$S_{11}^c = -\frac{1}{2}\bar{\mathrm{K}}_{33}\left(\frac{T}{B}\right)^2 . \tag{7.27}$$

For z-independent modulus, $\bar{\mathrm{K}}_{33} = \mathrm{K}_{33}$. The latter is the classical result. It has been used with different choices for the modulus K_{33}.

Gerard and Becker (1957) preferred the incremental modulus from J_2 deformation theory due to its better fitting of experimental results than the elastic shear modulus. Hutchinson and Budiansky (1976), Black et al. (2002) used the J_2 flow theory in conjunction with a preexisting imperfection that cured the problem raised by the excessive lateral stiffness by application of the plastic tangential modulus. Based on such experience, Bažant and Cedolin (1991, sect. 8.1) propose to use the tangential modulus on the secondary path for structural buckling. This algorithm improves the obtained results at the cost of violating the principle of determinism: The process continuation after the bifurcation influences the bifurcation point itself.

The proposed vertex model automatically uses a well defined reduced modulus on a strictly deterministic basis. The exact function for $\bar{\mathrm{K}}_{33}$ has been integrated numerically for different values of $\frac{\theta}{\dot{\epsilon}_0}$ and T at perfect plastic ($g = \mathrm{const}$) behaviour and can be found in Fig. 7.3.

With increasing influence of the buckling mode, the reduced shear modulus decreases. Fig. 7.2 shows, that the lowest possible value can be obtained in the limit for an infinite ratio $\frac{\theta}{\dot{\epsilon}_0}$ leading to $\alpha = 0$ almost everywhere. An increasing thickness of the shell leads to smaller reduced moduli.

7.4 Determination of the secondary path by the rate functional

Section Overview
In analogy to the threedimensional theory, the virtual work principle is transferred into a rate problem which is submitted to Petryk's energy criterion of path stability. It results in a selection criterion for the secondary path and allows for a final exploitation of the buckling equation (7.27).

For rate-independent materials with a rate potential, insertion of the incremental material law (6.32) starting from the primary path without torsional displacement results in a rate functional

$$H(\dot\epsilon_0,\varphi)=\int_0^L\left(\int_0^B\int_{-\frac{T}{2}}^{\frac{T}{2}}\left(\left[2\mathrm{K}_{33}z^2+S_{11}x_2^2\right]\frac{(\varphi')^2}{2}+\mathrm{K}_{11}\frac{\dot\epsilon_0^2}{2}\right)\mathrm{d}z\,\mathrm{d}x_2+\dot P\,\dot\epsilon_0\right)\mathrm{d}x_1. \tag{7.28}$$

(7.28) is at the same time the second order time derivative of the energy consumption (Petryk, 1991, Nguyen, 2000),

$$\begin{aligned}\frac{1}{2}\Delta\ddot E&=\frac{\mathrm{d}^2}{\mathrm{d}t^2}\int_0^t\int_0^L\left(\int_0^B\left(2M_{12}\,\dot K_{12}+N_{11}\,(\dot{\mathbf{E}}_2)_{11}\right)\mathrm{d}x_2+P\,\dot\epsilon_0\right)\mathrm{d}x_1\,\mathrm{d}t\\&=H(\dot\epsilon_0,\varphi).\end{aligned} \tag{7.29}$$

Accordingly, processes that do not minimize the rate functional but give only a saddle point are not stable (Petryk, 1991, 2000a, Fedelich and Ehrlacher, 1997).

The variation with respect to the two variables $\dot\epsilon_0,\varphi(x_1)$ yields (7.14). By the previously used ansatz for the eigenmode, $\varphi'=\theta$, the integration results after division by L in

$$H(\dot\epsilon_0,\theta)=\frac{TB^3}{3}\left[S_{11}+\frac{1}{2}\left(\frac{T}{B}\right)^2\bar{\mathrm{K}}_{33}\right]\frac{\theta^2}{2}+BT\bar{\mathrm{K}}_{11}\,\frac{\dot\epsilon_0^2}{2}+\dot P\,\dot\epsilon_0. \tag{7.30}$$

Here, a reduced longitudinal modulus

$$\bar{\mathrm{K}}_{11}=\frac{1}{T}\int_{-\frac{T}{2}}^{\frac{T}{2}}\mathrm{K}_{11}\,\mathrm{d}z \tag{7.31}$$

has been introduced similar to (7.26).

In minimizing, we calculate the partial derivatives

$$\begin{aligned}H_{,\dot\epsilon_0}&=BT\bar{\mathrm{K}}_{11}\,\dot\epsilon_0+\dot P=0\\H_{,\theta}&=\frac{TB^3}{3}\left[S_{11}+\frac{1}{2}\left(\frac{T}{B}\right)^2\bar{\mathrm{K}}_{33}\right]\theta=0,\end{aligned} \tag{7.32}$$

leading to a minimum at $\theta=0$, $BT\bar{\mathrm{K}}_{11}\,\dot\epsilon_0=-\dot P$. This is exactly the primary path.

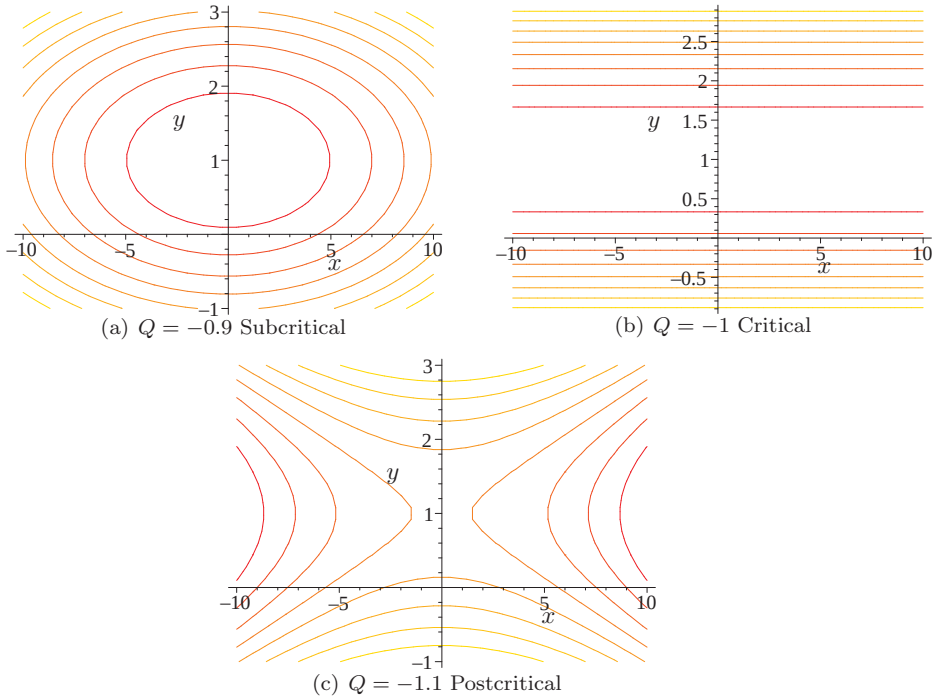

(a) $Q = -0.9$ Subcritical (b) $Q = -1$ Critical

(c) $Q = -1.1$ Postcritical

Fig. 7.4: Plot of the second variation of the energy functional $\frac{BT\bar{\mathrm{K}}_{11}}{\dot{P}^2} H(x, y)$ which governs the buckling behaviour of the cruciform

The minimum exists, if the second variation is positive, i.e. the bracketed term is positive. At the critical load, the minimum and the related equilibrium state get indefinite. For a further increasing compressive load an instable process results.

We represent the rate functional in a normalized way,

$$H(x, y) = \frac{BT}{R^2} \left[\frac{S_{11}^c}{3} (1 - Q) \frac{x^2}{2} + \bar{\mathrm{K}}_{11} \left(\frac{y^2}{2} + y \right) \right], \tag{7.33}$$

$S_{11}^c = \frac{1}{2} \left(\frac{T}{B} \right)^2 \bar{\mathrm{K}}_{33}$, $Q = -\frac{S_{11}}{S_{11}^c}$, $R = \frac{BT\bar{\mathrm{K}}_{11}}{\dot{P}}$, $x = BR\theta$, $y = R\dot{\epsilon}_0$. The parameter $Q \in \{0.9, 1, 1.1\}$ selects examples of subcritical, critical and postcritical loads. At the critical point, the quadratic form changes from the elliptic to the hyperbolic range, supporting the above finding of lost stability. Fig. 7.4 shows contour lines of the normalized rate functional for the mentioned cases, assuming a constant value of $\bar{\mathrm{K}}_{11}$ and of $\bar{\mathrm{K}}_{33}$, which corresponds to replacing H by its second variation.

In the critical case, an indifferent situation can be found, assigning a minimum to every path with $y = -1 \Rightarrow BT\bar{\mathrm{K}}_{11}\, \dot{\epsilon}_0 = -\dot{P}$.

In considering the dependence of $\bar{\mathrm{K}}_{11}$ on α and thus on $\frac{\theta}{\dot{\epsilon}_0} = \frac{1}{B}\frac{x}{y}$, the picture differs somewhat. The rate potential at the critical load can be written as

$$H^c = \underbrace{\frac{\dot{P}^2}{BT\bar{\mathrm{K}}_{11}}}_{f(\frac{x}{y})} \cdot \left(\frac{y^2}{2} + y\right), \tag{7.34}$$

Accordingly, the minimum of $f(\frac{x}{y})$ is reached by an independent adjustment of $\frac{x}{y}$ at a given rate of applied force, $\dot{P}$.

As shown in Fig. 6.2, K_{11} grows with decreasing α. Thus, the limit state

$$\frac{x}{y} \to \infty \;\Rightarrow\; \alpha \to 0 \tag{7.35}$$

reaches the minimum almost everywhere. As a consequence, $\bar{\mathrm{K}}_{11} = \mathrm{K}_{11}$, $\bar{\mathrm{K}}_{33} = \mathrm{K}_{33}$.

For the postcritical case, the minimum has changed into a saddle point, which is a typical result for buckling problems. Such results have also been reported for other structural stability problems, namely the discrete Shanley's column (Petryk, 1991).

7.5 Comparison with buckling experiments

To asses the capability of the proposed vertex model, the minimizing incremental shear modulus has been inserted into (7.27),

$$S_{11} = -\frac{1}{2}\bar{\mathrm{K}}_{33}(\alpha = 0)\left(\frac{T}{B}\right)^2. \tag{7.36}$$

The experimental results reported by Gerard and Becker (1957) for 2024-T4 Aluminium by plotting the buckling reduction factor

$$\eta(S_{11}) = \frac{S_{11}}{S_{11}^{\mathrm{el}}} = \frac{\bar{\mathrm{K}}_{33}}{\mathrm{K}_{33}^{\mathrm{el}}} \tag{7.37}$$

show the reduction of the critical stress compared to the elastic theory. It is easily obtained if the reduced shear modulus $\bar{\mathrm{K}}_{33}$ is given. As noted before, the J_2 flow theory is unable to reproduce this difference.

To evaluate (7.37), an analytical expression has been adopted for the hardening behaviour, as proposed by Papadopoulos and Lu (1998).

$$\begin{aligned} g(z) &= \sigma_Y^0 + q(z) \\ q(z) &= H_0 z + \left(\sigma_Y^\infty - \sigma_Y^0\right)\left(1 - \exp(-\zeta z)\right). \end{aligned} \tag{7.38}$$

The graph has been shown in Fig. 7.5 and the parameters can be found in Tab. 7.1. For different values of z, (7.37) has been evaluated. These values are typically in the transitory nonlinear hardening range.

E	73789 MPa	ν	0.33
σ_Y^0	200 MPa	σ_Y^∞	350 MPa
H_0	8060 MPa	ζ	8042

Tab. 7.1: Material data for the macroscopic vertex model for 2024-T4 Aluminum (Adapted from Papadopoulos and Lu, 1998)

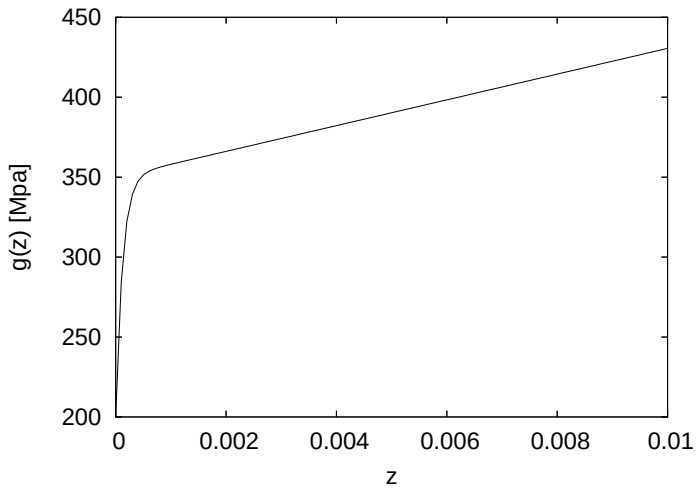

Fig. 7.5: The hardening curve of 2024-T4 (Al)

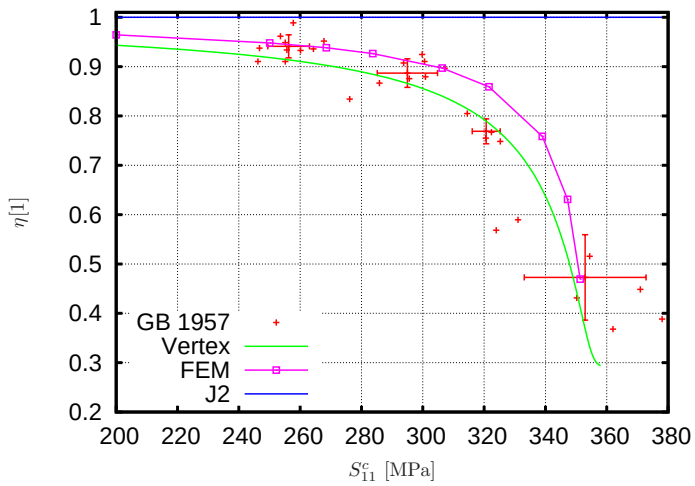

Fig. 7.6: The buckling reduction factor η of the vertex model (analytical solution from (7.37) and FEM solution from (7.43)) in comparison to experimental data by Gerard and Becker (1957), added mean values for every cluster. Error bars denote double standard deviation.

To compare the results with the experimental observations, the experimental data from Gerard and Becker (1957) have been digitized and the units converted to the SI system. In addition, clusters of repeated tests with similar results have been identified. For each cluster, the mean value and the standard deviation have been computed. Fig. 7.6 reports this data, together with the respective result of the vertex model.

The latter exhibits a hardening-dependent reduction of the critical buckling load compared to the elastic response. The theoretical prediction in the plastic regime (for which the line has been drawn) is within the double standard deviation around the centers of gravity of the experimental clusters. As further experimental data is lacking, an extrapolation to a larger range of strain has not been done.

From the structure of the gouverning equations (7.37),(7.38), it is clear that in the linear hardening range the reduced modulus is constant, leading also to a constant value for the buckling reduction factor.

7.6 Numerical approach

Section Overview
A numerical treatment of the cruciform column based on the torsion dominant incremental moduli $\alpha = 0$ and eigenvalue buckling in an iterative approach confirms the above results.

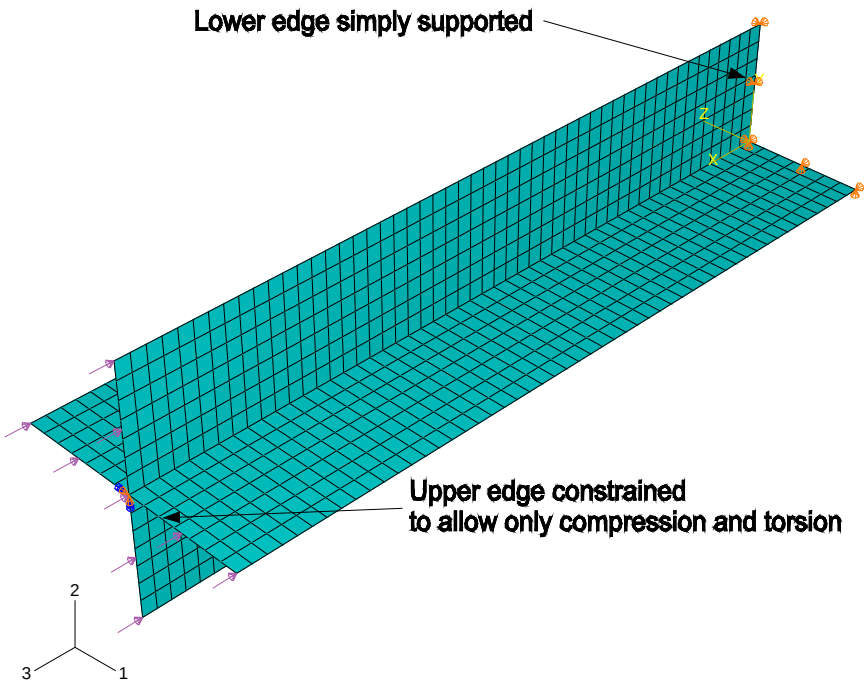

Fig. 7.7: FEM model of the cruciform column

7.6.1 The structural model

The cruciform column has been modelled with the finite element code ABAQUS. Bi-linear four-node shell elements with reduced integration (S4R) elements have been used.

As for the boundary conditions, each flange has been modeled simply supported at the bottom end. The upper end edges have been constrained to follow the rigid body motion of the center line end point which was additionally constrained excluding rotations except in torsion mode. Thus bending-like buckling has been prevented. At the upper edges a uniform compressive line load has been applied. A typical mesh is shown in Fig. 7.7.

7.6.2 Eigenvalue buckling

For the numerical approach, an equivalent to the bifurcation equation (7.25) has to be found.

A solution for a material of the rate type is supplied by the eigenvalue buckling analysis. For a prescribed unit load case, the load factor can be obtained from the general eigenvalue problem of the incremental system stiffness matrix,

$$\left(\underline{\underline{K}}_d + \lambda \underline{\underline{K}}_{g0}\right) \cdot \underline{\Delta \dot{v}} = \underline{0}. \tag{7.39}$$

Besides the definition of geometry and load case, the user has to supply the appropriate incremental stiffness tensor.

According to the vertex model, all directions othogonal to $\tilde{\mathbf{M}}_{\mathrm{N}}$ are equivalent, as the theory automatically adjusts to each of them. Such complicated computations are impossible with the eigenvalue buckling analysis where the secondary direction and thus $\tilde{\mathbf{M}}_{\mathrm{T}}$ are not known in advance. From (6.29),

$$\begin{aligned} \tilde{\mathbb{K}}_p &\propto \left(F(\alpha)\tilde{\mathbf{M}}_{\mathrm{N}} + (1-F(\alpha))\tilde{\mathbf{M}}_{\mathrm{T}}\right) \otimes \left(F(\alpha)\tilde{\mathbf{M}}_{\mathrm{N}} + (1-F(\alpha))\tilde{\mathbf{M}}_{\mathrm{T}}\right) \\ &= F^2\, \tilde{\mathbf{M}}_{\mathrm{N}} \otimes \tilde{\mathbf{M}}_{\mathrm{N}} + F\,(1-F)\,\mathrm{sym}\tilde{\mathbf{M}}_{\mathrm{N}} \otimes \tilde{\mathbf{M}}_{\mathrm{T}} + (1-F)^2 \tilde{\mathbf{M}}_{\mathrm{T}} \otimes \tilde{\mathbf{M}}_{\mathrm{T}} \end{aligned} \tag{7.40}$$

yields different contributions in the $\tilde{\mathbf{M}}_{\mathrm{N}}$ and the $\tilde{\mathbf{M}}_{\mathrm{T}}$ directions. These are independent from the particular choice of $\tilde{\mathbf{M}}_{\mathrm{T}}$ according to the construction of the vertex model. A rotational symmetric incremental plastic stiffness tensor

$$\tilde{\mathbb{K}}_p^{\mathrm{rot}} = F^2\, \tilde{\mathbf{M}}_{\mathrm{N}} \otimes \tilde{\mathbf{M}}_{\mathrm{N}} + F\,(1-F)\,\mathrm{sym}\tilde{\mathbf{M}}_{\mathrm{N}} \otimes \left(\sum \tilde{\mathbf{M}}_{\mathrm{T}i}\right) + (1-F)^2 \sum \tilde{\mathbf{M}}_{\mathrm{T}i} \otimes \tilde{\mathbf{M}}_{\mathrm{T}i} \tag{7.41}$$

can be obtained using all 5 symmetric tensorial direction perpendicular to $\tilde{\mathbf{M}}_{\mathrm{N}}$, called $\tilde{\mathbf{M}}_{\mathrm{T}i}$. Thus the matrix representation in the tensorial base $\left\{\tilde{\mathbf{M}}_{\mathrm{N}}, \tilde{\mathbf{M}}_{\mathrm{T}i}\right\}$ of $\tilde{\mathbb{K}}_p$ is changed according to

$$\begin{bmatrix} a & b & 0 & 0 & 0 & 0 \\ b & c & 0 & 0 & 0 & 0 \\ 0 & 0 & 0 & 0 & 0 & 0 \\ 0 & 0 & 0 & 0 & 0 & 0 \\ 0 & 0 & 0 & 0 & 0 & 0 \\ 0 & 0 & 0 & 0 & 0 & 0 \end{bmatrix} \rightarrow \begin{bmatrix} a & b & b & b & b & b \\ b & c & 0 & 0 & 0 & 0 \\ b & 0 & c & 0 & 0 & 0 \\ b & 0 & 0 & c & 0 & 0 \\ b & 0 & 0 & 0 & c & 0 \\ b & 0 & 0 & 0 & 0 & c \end{bmatrix} \tag{7.42}$$

allowing for an arbitrary secondary path with a constant incremental stiffness.

For the α-dependence we choose the minimizing result for $\alpha = 0$ (7.35).

7.6.3 Iterative buckling solution

The solution process is complicated by the persisting dependence of the incremental stiffness on the hardening modulus $\hat{h}(z) = \frac{\partial g}{\partial z}$ that is linked with the stress in the plastic state due to the critical stress $\hat{g}(z)$.

Accordingly, an iterative approach is mandatory. Considerable simplification is achieved by keeping the stiffness constant and iterating over geometric parameters. For a fixed length L and arm width B of the cruciform, a simple fix point iteration for the thickness T is used (see Table 7.2). The update equation

1. Fix a value of z and compute the hardening modulus $h(z)$, the rotationally symmetric incremental stiffness $\tilde{\mathbb{K}}_e + \tilde{\mathbb{K}}_p^{\text{rot}}$ and the equivalent stress $g(z)$. Estimate the initial thickness T_0.
2. Create the FEM model for the given geometry and material parameters and compute the buckling load factor λ_i. Being a line load, it determines the uniaxial stress $\sigma_i = \frac{\lambda_i}{T_i}$.
3. From the analytical result, compute the next iterate for the Thickness, $T_{i+1} = T_i \left(\frac{g(z)}{\sigma_i}\right)^2$.
4. Until convergence of T (and thus λ) repeat from 2.

Tab. 7.2: Iterative solution of the buckling problem

is based on the analytical buckling equation (7.27). It is found that a single iteration step is sufficient to obtain four significant figures of the thickness.

To facilitate the iterative approach, a PYTHON (www.python.org) script has been implemented that computes the incremental stiffness matrix, uses the preprocessor ABAQUS CAE (Abaqus, Inc., 2005) in the model building process, submits the created jobs to ABAQUS ANALYSIS, and displays the results. The reading of the buckling load cannot be automated in the same fashion as it is not included in the machine readable ABAQUS output database. Thus it has to be read from the displayed result and typed in the iteration script manually by the user.

Typical buckling modes for the vertex model and the according elastic behaviour can be found in the Figures 7.8–7.9. The differences between elastic and inelastic buckling shapes are marginal. Obviously, the shape is dominated by the shell kinematics and the support of the different edges and not by the material equations.

Both the first and the second mode have a torsion angle varying with the length coordinate. In contrast, analytical torsion theory would predict a constant twist per unit length.

The resulting buckling loads have been converted to stresses and with the definition of the buckling reduction factor

$$\eta = \frac{\frac{\lambda_{\text{vertex}}}{T_{\text{vertex}}}}{\frac{\lambda_{\text{elastic}}}{T_{\text{elastic}}}} \tag{7.43}$$

the results can be added to the diagram in Fig. 7.6, reproducing the analytical curve at a little too high level.

Similar results have been obtained by Papadopoulos and Lu (1998). However, their computational approach is based on Naghdi's version of finite plasticity with a symmetric plastic state variable. Moreover, a return-mapping

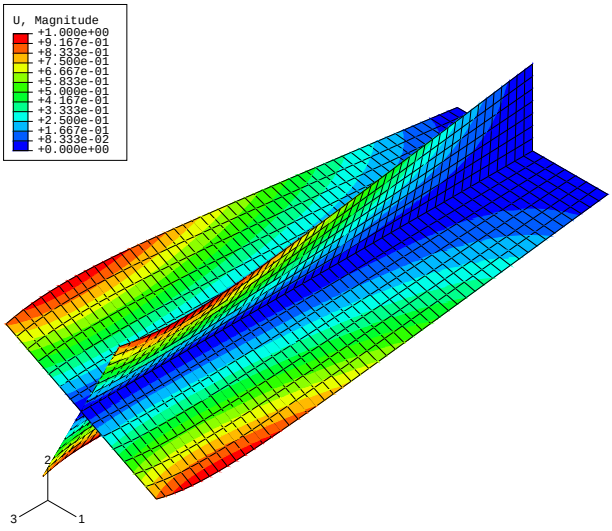

(a) Mode 1 vertex

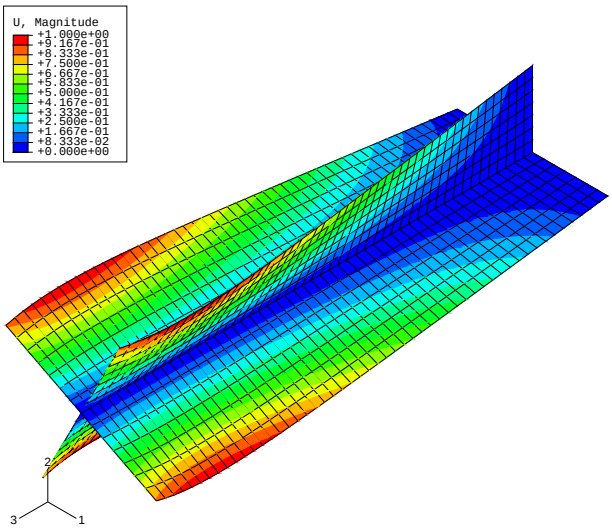

(b) Mode 1 elastic

Fig. 7.8: First buckling modes for the vertex model and for elastic behaviour

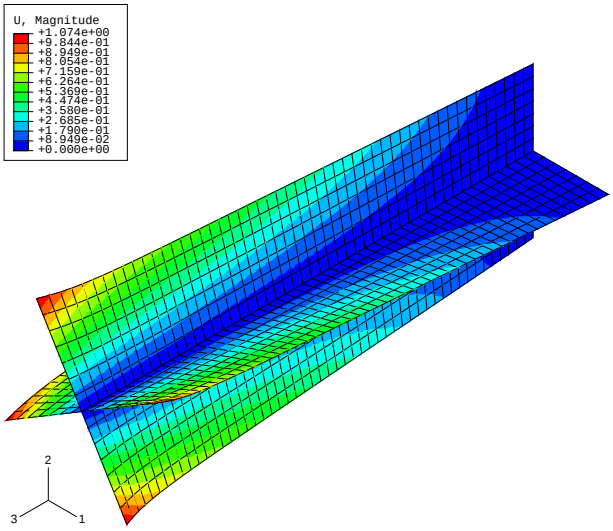

(a) Mode 2 vertex

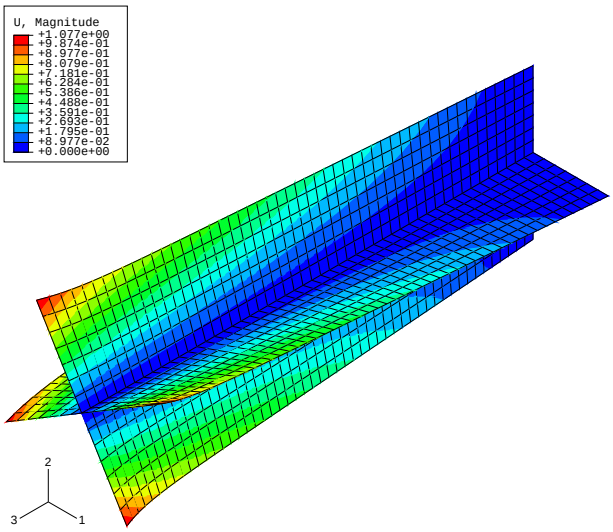

(b) Mode 2 elastic

Fig. 7.9: Second buckling modes for the vertex model and for elastic behaviour

algorithm is used that artificially introduces a vertex into smooth models of plasticity if only the time step is large enough.

8. CONCLUSIONS AND OUTLOOK

In the present work the difference between the multi-mode theory of plasticity and its regularized counterparts have been worked out to introduce the vertex effect, i.e. the dependence of the plastic flow on the direction of process continuation, whether proportional or not.

The name of the effect is based on the theoretical prediction of vertices in subsequent yield surfaces after prestrain processes. Using a polycrystal simulation with the Taylor-Lin model, it has been shown that such corners or vertices are formed due to the interaction of many single mechanisms.

Based on a single mechanism, a phenomenological vertex model has been proposed. It is an extension of the classical J_2 flow theory which is enhanced with yield-surface parallel terms in the flow rule. In addition, it is shown that the resulting plastic potential can be used as a yield surface. Thus the prerequisites for the existence of an incremental rate potential are fulfilled.

Its parameters, namely the transitory behaviour upon gradual or sudden strain path changes have been identified from a comparison with homogenized results of the above mentioned polycrystal model.

An experimental verification has been given by tension-torsion tests in hollow tubular copper specimens as reported by Lensky (1960) with obvious improvements in the transient results after a sudden strain path change as well as in smooth non-proportional processes. This delay effect is properly predicted by the vertex model.

A possible structural application has been demonstrated by the example of the plastic buckling of a cruciform column. Besides an enhancement of the classical analytical result to the present case that is characterized by a variation of the incremental stiffness in the columns cross-section, the buckling reduction factor has been computed using an energetic stability analysis based on the rate functional. In contrast to the J_2 flow theory, experiments conducted by Gerard and Becker (1957) have been reproduced within the experimental accuracy. The same result has been obtained by a finite element eigenvalue buckling analysis.

The relevance of the vertex effect is in processes where small additional deformations are of importance. In large strain applications as in the forming analysis, other effects gain more importance like the development of microstructural parameters based on texture or dislocation dynamics. Such behaviour is not implemented in the present vertex model.

Only the most simple isotropic hardening effect has been introduced in the present work. A more sophisticated model could introduce anisotropic harden-

ing which accounts for another source of nonproportional effects as well as for proper cyclic behaviour by introduction of a back stress.

The present version has no isotropic incremental moduli (similar to the J_2 flow theory), but the underlying theory is nevertheless isotropic. An anisotropic extension would impose the need for a redefinition of the natural direction of plastic flow on a proportional path.

Part III

APPENDIX

LIST OF FIGURES

LIST OF TABLES

IMPORTANT SYMBOLS

A	$\mathcal{A}$	(4.47)	Active set
	$\tilde{\mathbf{A}}_\alpha$	(4.54)	
	a_α	(4.54)	
B	$\mathcal{B}$	(4.76)	Set of slip systems
C	$\mathbf{C}$	(3.8)	Right Cauchy-Green tensor
	$\tilde{\mathbf{C}}$	(4.30)	Elastic right Cauchy-Green tensor
	$\tilde{\mathbb{C}}$	(4.9)	Reference stiffness
	$\tilde{\mathbf{C}}\tilde{\mathbf{S}}$	(4.36)	Elastic Mandel tensor
D	$\mathbf{D}$	(3.12)	Stretching tensor
	$\bar{d}$	(5.7)	Dissipated power fraction
E	$\mathbf{E}$	(3.13)	Green's strain
	$\tilde{\mathbf{E}}$	(4.30)	Elastic Green's strain
	$\mathbf{E}^x$	(3.25)	Generic work conjugate strain tensor
F	$\mathbf{F}$	(3.3)	Deformation gradient
	$\tilde{\mathbf{F}}$	(4.28)	Elastic transformation
	F_1	(6.2)	Transition function for dissipation
	F	(6.15)	Transition function for plastic flow
G	g	(4.37)	Dual hardening variables
	$g_{\alpha\beta}$	(4.55)	Consistency Matrix
I	$\mathbb{I}$	(6.28)	Identity on second order tensors
	$\mathbb{I}^S$	(6.28)	Identiry on symmetric second order tensors
J	J	(3.6)	Jacobian of $\mathbf{F}$
K	$\mathbb{K}$	(4.66)	Incremental elastic-plastic moduli tensor
	$\tilde{\mathbb{K}}$	(4.66)	Incremental elastic-plastic moduli tensor
L	L^+		Set of tensors with positive determinant
	$\mathbf{L}$	(3.11)	Spatial velocity gradient
	$\tilde{\mathbf{L}}$	(4.35)	Apparent elastic velocity gradient

M	$\tilde{\mathbf{M}}$	(4.97)	Loading direction
	$\tilde{\mathbf{M}}_{\mathrm{N}}$	(4.99)	Natural direction
	$\tilde{\mathbf{M}}_{\mathrm{T}}$	(4.99)	Tangential direction
P	$\mathbf{P}$	(4.27)	Plastic transformation
S	$\mathbf{S}$	(3.28)	Second Piola-Kirchhoff stress
	$\tilde{\mathbf{S}}$	(4.30)	Elastic second Piola-Kirchhoff stress
	$\mathbf{S}^x$	(3.25)	Generic work conjugate stress tensor
T	$\mathbf{T}$	(3.19)	Cauchy stress
	$\mathbf{T}_0$	(3.22)	First Piola-Kirchhoff stress
	$\mathbb{T}$	(6.28)	Transposes a second order tensor
U	$\mathcal{U}$	(4.19)	Rate potential
Z	z	(4.37)	Primal Hardening variables
α	α	(4.102)	Loading parameter
ϵ	$\epsilon_{\log}$		Logarithmic equivalent strain
λ	λ_α	(4.45)	Plastic multipliers
π	$\hat{\mathbf{\Pi}}$	(4.39)	RHS of flow rule
	Π	(6.14)	Process dependent plastic potential
τ	$\boldsymbol{\tau}$	(3.25)	Kirchhoff stress
	τ_α	(4.74)	Schmid stress
	τ_α^c	(4.74)	Critical Schmid stress
ϕ	ϕ	(4.38)	Yield limit
ω	ω	(4.86)	Viscous flow potential
	$\bar{\omega}$	(5.5)	Homogenized flow potential

BIBLIOGRAPHY

Abaqus, Inc. ABAQUS, Version 6.5. 2005.

L. Anand and M. Kothari. A computational procedure for rate-independent crystal plasticity. *J. Mech. Phys. Solids*, 44(4):525–558, 1996.

S. Aris. *Simulation von Textur und texturbedingten Kristallitmikrodehnungen kubischer Werkstoffe und Vergleich mit experimentellen Daten*. Diss., TU Berlin, 2000. Berichte des Hahn-Meitner-Instituts Berlin, HMI-B 570, ISSN 0936-0891.

M. Arminjon. A regular form of the schmid law, application to the ambiguity problem. *Textures and Microstructures*, 14-18:1121–1128, 1991.

R.J. Asaro. Micromechanics of crystals and polycrystals. *Advances in Applied Mechanics*, 23, 1983.

S.B. Batdorf and B. Budiansky. A mathematical theory of plasticity based on the concept of slip. NACA Technical Note 1871, NACA, Washington, 1949.

Z.P. Bažant and L. Cedolin. *Stability of Structures: Elastic, Inelastic, Fracture and Damage Theories*. Oxford University Press, Oxford, 1991.

A. Bertram. *Axiomatische Einführung in die Kontinuumsmechanik*. BI Wissenschaftsverlag, Mannheim, 1989.

A. Bertram. Description of finite inelastic deformations. In A. Benallal, R. Billardon, and D. Marquis, editors, *Proceedings of MECAMAT 92, International Seminar on Multiaxial Plasticity*, 821–835, 1992.

A. Bertram. An alternative approach to finite plasticity based on material isomorphisms. *Int. J. Plast.*, 15:353–374, 1999.

A. Bertram. *Elasticity and Plasticity of Large Deformations – an Introduction*. Springer, Berlin Heidelberg, 2005.

P.K. Bertsch and W.N. Findley. An experimental study of subsequent yield surfaces–corners, normality, Bauschinger and allied effects. In *Proc. 4th U.S. Nat. Congr. Appl. Mech.*, 1962.

J. F. W. Bishop and R. Hill. A theory of the plastic distortion of a polycrystal aggregate under combined stresses. *Phil. Mag.*, 42:414–427, 1951a.

J. F. W. Bishop and R. Hill. A theoretical derivation of the plastic properties of a polycrystalline face-centred metal. *Phil. Mag.*, 42:1298–1307, 1951b.

C. Black, N. Makris, and I. Aiken. Component testing, stability analysis, and characterization of buckling-restrained unbonded braces. PEER report 2002/08, Pacific Earthquake Engineering Research Center, University of California, Berkeley, 2002.

T. Böhlke. *Crystallographic Texture Evolution and Elastic Anisotropy.* Diss., Otto-von-Guericke-Universität Magdeburg, 2001. Shaker Verlag Aachen, ISBN 3-8265-8758-8.

T. Böhlke and A. Bertram. Simulation of texture development and induced anisotropy of polycrystals. In S. Atluri and P. O'Donoghue, editors, *Proceedings of ICES'98, Modelling ans Simulation Based Engineering*, 1390–1395, 1998.

M. Boucher, P. Cayla, and J.P. Cordebois. Experimental studies of yield surfaces of aluminium alloy and low carbon steel under complex biaxial loadings. In *Proceedings of MECAMAT 92*, 300–320, 1992.

S. Boyd and L. Vandenberghe. *Convex Optimization.* Cambridge University Press, Cambridge, 2004. URL `http://www.stanford.edu/~boyd/cvxbook.html`.

F.C. Caner, Z. P. Bažant, and J. Červenka. Vertex effect in strain-softening concrete at rotating principal axes. *J. Eng. Mech.*, 128:24–33, 2002.

G. Y. Chin and W. L. Mammel. Generalization and equivalence of the minimum work (taylor) and maximum work (bishophill) principles for crystal plasticity. *Trans. Metall. Soc., AIME*, 1211–1214, 1969.

J. Christoffersen and J.W. Hutchinson. A class of phenomenological corner theories of plasticity. *J. Mech. Phys. Solids*, 27:465–487, 1979.

M. K. Falgoust. On the validity of the Wagner hypothesis in thin-walled open-profile members. Master's thesis, University of Pittsburgh, School of Engineerig, 2004.

B. Fedelich and A. Ehrlacher. An analysis of stability of equilibrium and of quasi-static evolution on the basis of the dissipation function. *Eur. J. Mech. A/Solids*, 16:833–855, 1997.

W. Gambin. Plasticity of crystals with interacting slip systems. *Enging. Trans.*, 39:303–324, 1991.

W. Gambin and F. Barlat. Modeling of deformation texture development based on rate independent crystal plasticity. *Int. J. Plast.*, 13:75–85, 1997.

G. Gerard and H. Becker. Handbook of structural stability — Part I – buckling of flat plates. NACA Technical Note 3781, National Advisory Commitee for Aeronautics, Washington, 1957.

M. Gotoh. A class of plastic constitutive equations with vertex effect – i. general theory. *Int. J. Solids Structures*, 21:1101–1116, 1985a.

M. Gotoh. A simple plastic constitutive equation with vertex effect. *Eng. fract. mech.*, 21:673–684, 1985b.

M. Gotoh. A class of plastic constitutive equations with vertex effect – ii. discussions on the simplest form. *Int. J. Solids Structures*, 21:1117–1129, 1985c.

M. Goya and K. Ito. An expression of elastic-plastic constitutive law incorporating vertex formation and kinematic hardening. *ASME J. Appl. Mech.*, 58: 617–622, 1991.

M. Goya and K. Ito. Determination of constitutive parameters of plastic materials using a finite-element polycrystalline model. *JSME International Journal Series A*, 40:169–178, 1997.

N.K. Gupta and H.A. Lauert. A study of yield surface upon reversal of loading under biaxial stress. *ZAMM*, 63:497–504, 1983.

E. Hairer and G. Wanner. *Solving ordinary differential equations II– Stiff and differential-algebraic problems*. Springer, 1996.

M.B. Halphen and Q. S. Nguyen. Sur les matériaux standards généralisés. *J. Méca.*, 14:39–63, 1975.

K.S. Havner and A.H. Shalaby. Further investigation of a new hardening law in crystal plasticity. *J. Appl. Mech.*, 45:500–506, 1978.

S.S. Hecker. Yield surfaces in prestrained aluminum and copper. *Met. Trans.*, 2:2077–2086, 1971.

S.S. Hecker. Experimental investigations of corners in yield surface. *Acta Mechanica*, 13:69–86, 1972.

S.S. Hecker. Experimental studies of yield phenomena in biaxially loaded metals. In J.A. Stricklin and K.J. Saczalski, editors, *Constitutive Equations in Viscoplasticity: Computational and Engineering Aspects*, 1–34. ASME, 1976.

N. J. Higham. Computing the polar decomposition—with applications. *SIAM J. Sci. and Stat. Comp.*, 7(4):1160–1174, October 1986.

R. Hill. The elastic behavior of a crystalline aggregate. *Proc. Phys. Soc.*, A65: 349–354, 1952.

R. Hill. The essential structure of constitutive laws for metal composites and polycrystals. *J. Mech. Phys. Solids*, 15:79–95, 1967.

W.F. Hosford. *The mechanics of crystals and textured polycrystals*. Oxford University Press, New York, 1993.

P. Hu, J. Lian, Y.Q. Liu, and Y.X. Li. A quasi flow corner theory of elastic-plastic finite deformation. *Int. J. Solids Structures*, 35:1827–1845, 1998.

P. Hu, Y.Q. Liu, and J.C. Wang. Numerical study of the flange earring of deep-drawing sheets with stronger anisotropy. *International Journal of Mechanical Sciences*, 43:279–296, 2001.

J.W. Hutchinson. Elastic-plastic behaviour of polycrystalline metals and composites. *Proc. Roy. Soc. Lond. A*, 319:247–272, 1970.

J.W. Hutchinson. Bounds and self-consistent estimates for creep of polycrystalline materials. *Proc. Roy. Soc. Lond. A*, 348:101–127, 1976.

J.W. Hutchinson and B. Budiansky. Analytical and numerical study of the effects of initial imperfections on the inelastic buckling of a cruciform column. In B. Budiansky, editor, *Proceedings of IUTAM Symposium on Buckling of Structures*, 98–105. springer, 1976.

J.W. Hutchinson and V. Tvergaard. Shear band formation in plane strain. *Int. J. Solids Structures*, 17:451–470, 1981.

K. Ikegami. Experimental plasticity on the anisotropy of metals. In J.P. Boehler, editor, *Mechanical Behavior of Anisotropic Solids, Proceedings of the Euromech Colloquium 115*, volume 295 of *Colloques internationaux du centre national de la recherche scientifique*, 201–227, The Hague, Boston, London, 1982. Martinus Nijhoff Publishers.

K. Ito, M. Goya, and H. Takahashi. An expression of elastic-plastic constitutive law incorporating stress increment dependence (evolutional equation of stress increment dependency parameters on stress path). In *Proceedings of MECAMAT 92*, 689–694, 1992.

R. Kiryk and H. Petryk. A self-consistent model of rate-dependent plasticity of polycrystals. *Arch. Mech.*, 50:247–263, 1998.

R. Knockaert, Y. Chastel, and E. Massoni. Rate-independent crystalline and polycrystalline plasticity, application to fcc materials. *Int. J. Plast.*, 16:179–198, 2000.

U.F Kocks. The relation between polcrystal deformation and single-crystal deformation. *Metall. Trans.*, 1:1121, 1970.

U.F. Kocks. Simulation of deformation texture development for cubic metals. In Kocks et al. (1998), chapter 9.

U.F. Kocks. Kinematics and kinetics of plasticity. In Kocks et al. (1998), chapter 8.

U.F. Kocks, C.N. Tomé, and H.R. Wenk, editors. *Texture and Anisotropy.* Cambridge University Press, 1998.

W.T. Koiter. Stress-strain relations, uniqueness and variational theorems for elastic-plastic materials with a singular yield surface. *Quarterly of Applied Mathematics*, 11:350–354, 1953.

K. Kowalczyk. Evolution of plastic anisotropy for the polycrystalline materials in large deformation processes. *Engin. Trans.*, 49:537–571, 2001.

K. Kowalczyk and W. Gambin. Model of plastic anisotropy evolution with texture-dependent yield surface. *Int. J. Plast.*, 20:19–54, 2004.

M. Kraska and A. Bertram. Simulation of polycrystals using an FEM-based representative volume element. *Technische Mechanik*, 16:51–62, 1996.

Martin Kraska. *Textursimulation bei großen inelastischen Verformungen mit der Technik des repräsentativen Volumenelements (RVE).* Diss., TU Berlin, 1998.

Arnold Krawietz. *Materialtheorie.* Springer, Berlin, 1986.

M. Kuroda and V. Tvergaard. Use of abrupt strain path change for determining subsequent yield surface: illustrations of basic idea. *Acta Materialia*, 47, 1999.

M. Kuroda and V. Tvergaard. A phenomenological plasticity model with non-normality effects representing observations in crystal plasticity. *J. Mech. Phys. Solids*, 49:1239–1263, 2001a.

M. Kuroda and V. Tvergaard. Shear band development predicted by a non-normality theory of plasticity and comparisons to crystal plasticity predictions. *Int. J. Solids Structures*, 38:8945–8960, 2001b.

T. Kuwabara, M. Kuroda, V. Tvergaard, and K. Nomura. Use of abrupt strain path change for determining subsequent yield surface: experimental study with metal sheets. *Acta Metallurgica*, 48, 2000.

E.H. Lee and P.S. Symonds, editors. *Plasticity – Proceedings of the second symposium on naval structural mechanics.* Pergamon, Oxford, 1960.

D.C. Leigh. *Nonlinear Continuum Mechanics.* McGraw-Hill, New York, 1968.

V.S. Lensky. Analysis of plastic behavior of metals under complex loading. In Lee and Symonds (1960), 259–278.

T.H. Lin. A proposed theory of plasticity based on slips. In *Proceedings Second U.S. Nat. Cong. Applied Mechanics*, 461–468, 1954.

T.H. Lin. On stress-strain relations based on slip. In *Proceedings Third U.S. Nat. Cong. Applied Mechanics*, 581–587, 1958.

T.H. Lin and M. Ito. Theoretical plastic stress-strain relationship of a polycrystal and the comparisons with the von mises and tresca plasticity theories. *Int. J. Eng. Sci.*, 4:543–561, 1966. Paper presented at 5th U.S. Natnl. Cong. Appl. Mech.

V. A. Lubarda. *Elastoplasticity Theory.* CRC Press, Boca Raton, FL., 2002.

V.A. Lubarda and D.J. Benson. On the partitioning of the rate of deformation gradient in phenomenological plasticity. *Int. J. Solids Structures*, 38:6805–6814, 2001.

J. Lubliner. *Plasticity Theory.* Macmillan Publishing Comp., New York, 1990.

J. Mandel. Generalisation de la theorie de plasticite de W. T. Koiter. *Int. J. Solids Structures*, 1:273–295, 1965.

Z. Marciniak and K. Kuczynski. Limit strains in the processes of stretch-forming sheet metal. *Int. J. Mech. Sci.*, 9:609–620, 1967.

J.E. Marsden and T.J.R. Hughes. *Mathematical Foundations of Elasticity.* Dover, New York, 1994.

C. Miehe and J. Schröder. A comparative study of stress update algorithms for rate-independent and rate-dependent crystal plasticity. *Int. J. Numer. Meth. Engng.*, 50:273–298, 2001.

C. Miehe, J. Schröder, and J. Schotte. Computational homogenization analysis in finite plasticity simulation of texture development in polycrystalline materials. *Comput. Methods Appl. Mech. Engrg.*, 171:387–418, 1999.

C. Miehe, J. Schotte, and Lambrecht M. Homogenization of inelastic solid materials at finite strains based on incremental minimization principles. application to the texture analysis of polycrystals. *J. Mech. Phys. Solids*, 50: 2123–2167, 2002.

A. Mielke. Energetic formulatione of multiplicative elasto-plasticity using dissipation distances. *Cont. Mech. Thermodyn.*, 15:351–382, 2003.

F. Mollica and A.R. Srinivasa. A general framework for generating convex yield surfaces for anisotropic metals. *Acta Mechanica*, 154:61–84, 2002.

I. Müller. *Thermodynamics.* Pitman, 1985.

I. Müller and T. Ruggeri. *Rational Extended Thermodynamics.* Springer, 1993.

P. Neff. *Mathematische Analyse multiplikativer Viskoplastizität.* Diss., Technische Universität Darmstadt, 2000. Shaker Verlag, Aachen.

Q. S. Nguyen. *Stability and Nonlinear Solid Mechanics*. John Wiley & Sons, Chichester, 2000.

P. Papadopoulos and J. Lu. A general framework for the numerical solution of problems in finite elasto-plasticity. *Comp. Meth. Appl. Mech. Engrg.*, 159: 1–8, 1998.

D. Peirce, R.J. Asaro, and A. Needleman. An analysis of nonuniform and localized deformation in ductile single crystals. *Acta Metall.*, 30:1087–1119, 1982.

H. Petryk. The energy criteria of instability in time-independent inelastic solids. *Arch. Mech.*, 43:519–545, 1991.

H. Petryk. Macroscopic rate-variables in solids undergoing phase transformation. *J. Mech. Phys. Solids*, 46:873–894, 1998.

H. Petryk. On the micro-macro transition and hardening moduli in plasticity. In O. T. Bruhns and E. Stein, editors, *Proceedings of IUTAM Symposium on Micro- and Macrostructural Aspects of Thermoplasticity*, 219–230, 1999.

H. Petryk. Theory of material instability in incrementally nonlinear plasticity. In H. Petryk, editor, *Material Instability in Elastic and Plastic Solids*. Springer, Wien, New York, 2000a. CISM courses and Lectures, No. 414.

H. Petryk. General conditions for uniqueness in materials with multiple mechanisms of inelastic deformation. *J. Mech. Phys. Solids*, 48:367–396, 2000b.

H. Petryk and K. Thermann. Post-critical plastic deformation of biaxially stretched sheets. *Int. J. Solids Structures*, 32:689–705, 1996.

H. Petryk and K. Thermann. A yield-vertex modification of two-surface models of metal plasticity. *Arch. Mech.*, 49:847–863, 1997.

A. Phillips. Pointed vertices in plasticity. In Lee and Symonds (1960), 202–214.

A. Phillips and R.L. Sierakowski. On the concept of the yield surface. *Acta Mechanica*, 1:29–35, 1965.

J. R. Rice. On the structure of stress-strain-relations for time-dependent plastic deformations in metals. *J. Appl. Mech.*, 37:728–737, 1970.

J.W. Rudnicki and J.R. Rice. Conditions for the localization of deformation in pressure-sensitive dilatant materials. *J. Mech. Phys. Solids*, 23:371–394, 1975.

G. Sachs. Zur Ableitung einer Fließbedingung. *Z. Verein Deut. Ing.*, 72:734, 1928.

J.L. Sanders Jr. Plastic stress-strain relations based on linear loading functions. In *Proceedings of Second U.S. Nat. Cong. Applied Mechanics*, 455–460, 1954.

O. Scherf. *Numerische Simulation inelastischer Körper*. Diss., TU Darmstadt, Düsseldorf, 2000. VDI Fortschrittsberichte, Reihe 20, Nr. 321.

M. Schmidt-Baldassari. Numerical concepts for rate-independent single crystal plasticity. *Comput. Methods Appl. Mech. Engrg.*, 192:1261–1280, 2003.

M. Schurig and A. Bertram. A rate independent approach to crystal plasticity with a power law ansatz. *Comp. Mat. Sci*, 26:154–158, 2003.

M. Schurig and A. Bertram. Incorporation of the vertex effect into a plasticity theory with a modified plastic potential. *in preparation*, 2005.

M. Schurig, A. Bertram, and H. Petryk. Micromechanical analysis of the development of a yield vertex in polycrystal plasticity. *in preparation*, 2005.

M.J. Sewell. A plastic flow rule at a yield vertex. *J. Mech. Phys. Solids*, 22: 469–490, 1974.

E. Shiratori and K. Ikegami. Experimental study of the subsequent yield surface by using cross-shaped specimens. *J. Mech. Phys. Solids*, 16:373–394, 1968.

M. Šilhavý. *The Mechanics and Thermodynamics of Continuous Media*. Springer, 1997.

P. Steinmann. On localization analysis in multisurface hyperelasto-plasticity. *J. Mech. Phys. Solids*, 44:1691–1713, 1996.

S. Stören and J.R. Rice. Localized necking in thin sheets. *J. Mech. Phys. Solids*, 23:421–441, 1975.

T.B. Stoughton and X. Zhu. Review of theoretical models of the strain-based FLD and their relevance to the stress-based FLD. *Int. J. Plast.*, 20:1463–1486, 2004.

G. I. Taylor. Plastic strain in metals. *J. Inst. Met.*, 62:307–324, 1938.

H. Tresca. Mémoire sur l'coulement des corps solides soumis de fortes pressions. *Comptes Rendus Acad. Sci. Paris*, 59:754, 1864.

C. A. Truesdell and W. Noll. *The Non-linear Field Theories of Mechanics*. Springer, Berlin, 1965.

S. Tsutsumi and K. Hashiguchi. General non-proportional loading behavior of soils. *Int. J. Plast.*, 2005.

P. van Houtte. A comprehensive mathematical formulation of an extended Taylor-Bishop-Hill model of featuring relaxed constraints, the Renouard-Wintenberger theory and a strain rate sensitivity model. *Textures and Microstructures*, 8–9:313–350, 1988.

H. Wagner. Verdrehung und Knickung von offenen Profilen. In *Festschrift zum 25. Jahrestag der TH Danzig*. Danzig, 1929.

K. Wilmański. *Thermomechanics of Continua*. Springer, Berlin, Heidelberg, 1998.

www.python.org. Python programming language. www.python.org, 2005.

P. Zattarin, P. Lipinski, and A. Rosochowski. Numerical study of the inflence of microstructure on subsequent yield surfaces of polycrystalline materials. *Int. J. Mech. Sci.*, 46:1377–1398, 2004.

INDEX